



**HAL**  
open science

## Etude théorique d'oxydes nano-structurés multifonctionnels

Jinzhu Zhao

► **To cite this version:**

Jinzhu Zhao. Etude théorique d'oxydes nano-structurés multifonctionnels. Autre. Université Sciences et Technologies - Bordeaux I, 2013. Français. NNT : 2013BOR14866 . tel-00986110

**HAL Id: tel-00986110**

**<https://theses.hal.science/tel-00986110>**

Submitted on 1 May 2014

**HAL** is a multi-disciplinary open access archive for the deposit and dissemination of scientific research documents, whether they are published or not. The documents may come from teaching and research institutions in France or abroad, or from public or private research centers.

L'archive ouverte pluridisciplinaire **HAL**, est destinée au dépôt et à la diffusion de documents scientifiques de niveau recherche, publiés ou non, émanant des établissements d'enseignement et de recherche français ou étrangers, des laboratoires publics ou privés.



# THÈSE

PRÉSENTÉE A

**L'UNIVERSITÉ BORDEAUX 1**

ÉCOLE DOCTORALE DES SCIENCES CHIMIQUES

ET A

**L'UNIVERSITÉ DE LIEGE**

ÉCOLE DOCTORALE DE PHYSIQUE

Par Jinzhu ZHAO

POUR OBTENIR LE GRADE DE DOCTEUR

SPÉCIALITÉ : Physico-Chimie de la Matière Condensée

**First-principles study of ferroelectricity in oxide superlattices**

Directeurs de recherche : MM. A. Villesuzanne et Ph. Ghosez

Soutenue le : 11 octobre 2013

Après avis de :

<b>M. J. ÍÑIGUEZ</b>	Chercheur – ICMAB – Université Autonome de Barcelone	Rapporteur
<b>M. G. GENESTE</b>	Ingénieur-chercheur – CEA-DAM Ile de France	Rapporteur

Devant la commission d'examen formée de :

<b>M. E. BOUSQUET</b>	Professeur – Université de Liège	Examineur
<b>M. J. CORS</b>	Docteur – PHASIS – Université de Genève	Examineur
<b>M. J. ETOURNEAU</b>	Professeur émérite – ICMCB, Bordeaux	Président du Jury
<b>M. G. GENESTE</b>	Ingénieur-chercheur – CEA-DAM Ile de France	Rapporteur
<b>M. Ph. GHOSEZ</b>	Professeur – Université de Liège	Examineur
<b>M. J. ÍÑIGUEZ</b>	Chercheur – ICMAB, Université Autonome de Barcelone	Rapporteur
<b>M. M. MAGLIONE</b>	Directeur de recherche – ICMCB, Bordeaux	Examineur
<b>M. A. VILLESUZANNE</b>	Chargé de recherche – ICMCB, Bordeaux	Examineur

*Université Bordeaux 1*

*Les Sciences et les Technologies au service de l'Homme et de l'environnement*





UNIVERSITÉ DE BORDEAUX I  
Ecole Doctorale des Sciences Chimiques

UNIVERSITÉ DE LIEGE  
Ecole Doctorale de Physique

# First-principles study of ferroelectricity in oxide superlattices

*A thesis submitted in fulfillment of the requirements for the  
degree of PhD in Sciences*

by

**Jinzhu ZHAO**

***Supervisors:***

Prof. Philippe GHOSEZ

Dr. Antoine VILLESUZANNE

***Jury members:***

Prof. Jean ETOURNEAU

Dr. Jorge ÍÑIGUEZ

Dr. Gregory GENESTE

Dr. Jorge CORS

Dr. Mario MAGLIONE

Dr. Eric BOUSQUET

October 2013



## Résumé de la thèse

### I. INTRODUCTION.

Les propriétés structurales et de dynamique de réseau (instabilités de type ferroélectriques) d'oxydes fonctionnels complexes sont ici étudiées par méthodes de premiers principes, approches phénoménologiques, et par construction d'un potentiel modèle.

Plus particulièrement, les systèmes étudiés peuvent être décrits comme des super-réseaux basés sur des titanates de structure perovskite  $ATiO_3$  ( $A=Ba, Sr, Pb$ ) et des oxydes binaires de formulation  $AO$ , à structure type  $NaCl$ . Certains de ces super-réseaux existent naturellement (phases de Ruddlesden-Popper), les autres peuvent être dérivées de ces structures naturelles en insérant des plans  $AO$  supplémentaires à l'interface entre couches de type pérovskite, ou encore être conçus comme des intercroissances de phases à cation  $A$  différent.

En jouant sur ces paramètres compositionnels et structuraux, ainsi que sur les effets de dimensionnalité et de contraintes aux interfaces, il est envisagé de pouvoir moduler les propriétés ferroélectriques de ces systèmes nano-structurés, et de voir émerger de nouveaux phénomènes et/ou des propriétés ferroélectriques exotiques.

### II. OUTILS THEORIQUES

L'essentiel des calculs fait appel à la théorie de la fonctionnelle de la densité, pour établir en particulier les courbes de dispersion de phonons (les phonons d'énergie négative indiquent et décrivent une instabilité structurale), les énergies associées aux distorsions mis en évidence, les constantes de force inter-atomiques.

Par ailleurs, un effort important est dédié à la construction de potentiels modèles, mettant en jeu les paramètres évalués par les calculs DFT. L'idée est d'évaluer ces paramètres sur des systèmes simples, de construire un modèle transférable aux systèmes à structure de complexité arbitraire, et de pouvoir accéder aux effets de la température par des approches statistiques (algorithmes de Monte-Carlo). Les phénomènes dépendant de la température (en particulier, les transitions de phase), peuvent ainsi, dans le cas idéal, être étudiés pour des structures complexes avec une précision équivalente à celle des calculs de premiers principes.

Enfin, une approche phénoménologique de type Landau-Devonshire est appliquée au cas des réseaux  $PbTiO_3/SrTiO_3$  de période minimale, permettant de tester le modèle minimal requis pour reproduire des données expérimentales originales obtenues dans la littérature pour ce système. Des phénomènes non attendus et originaux, offrant d'intéressantes perspectives, ont par ailleurs été mis en évidence par cette approche.

### III. Le super-réseau $PbTiO_3/SrTiO_3$ (1/1)

Le super-réseau  $PbTiO_3/SrTiO_3$  (1/1) est constitué de couches pérovskites simples (épaisseur d'un octaèdre  $TiO_6$ ) et a fait l'objet de travaux expérimentaux précis, montrant de la ferroélectricité de type impropre. En accord avec l'expérience, les calculs DFT montrent bien que l'instabilité ferroélectrique fait ici intervenir trois paramètres d'ordre (un mode polaire et deux modes de

rotations d'octaèdres). Les résultats expérimentaux (notamment, évolution linéaire de la polarisation avec la température, et non-divergence de la constante diélectrique à la transition) sont bien reproduits par un modèle phénoménologique macroscopique de type Landau, et l'introduction de températures critique distinctes pour les trois paramètres d'ordre révèle un comportement inattendu (conservation du comportement linéaire de la polarisation vs. T), ouvrant le champ d'une ferroélectricité impropre de type exotique (Figure 1).

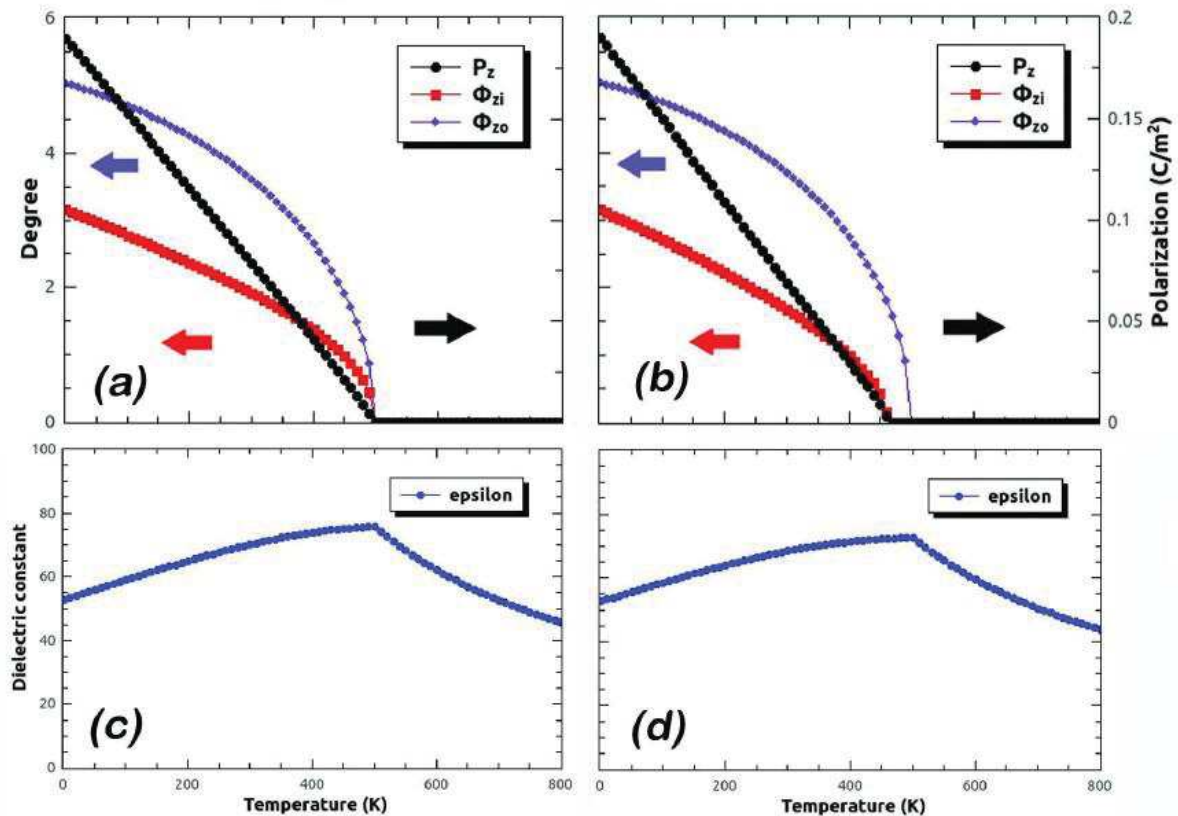


**Figure 1.** Amplitude des modes de distorsion polaires  $P_z$  et de rotation  $\Phi_{zi}$  et  $\Phi_{zo}$  en fonction de la température, et constante diélectrique relative, calculées par une approche de type Landau-Devonshire, et reproduisant les résultats expérimentaux pour le système  $\text{PbTiO}_3/\text{SrTiO}_3$  (1/1).

La construction d'un potentiel modèle microscopique, associé à une simulation de type Monte-Carlo, permet de retrouver le comportement diélectrique attendu, et de révéler la signature d'autres condensations de modes à basse température (Figure 2). Ce modèle doit être affiné, mais permet d'ores et déjà d'envisager son application à l'étude des transitions de phase au sein de systèmes beaucoup plus complexes, et faisant intervenir le couplage de plusieurs paramètres d'ordre. Enfin, les effets du champ électrique appliqué et des contraintes (pression chimique / effets de substrat) ont pu être abordés et montrent que le comportement diélectrique peut être ainsi modulé de façon contrôlée dans ces systèmes.

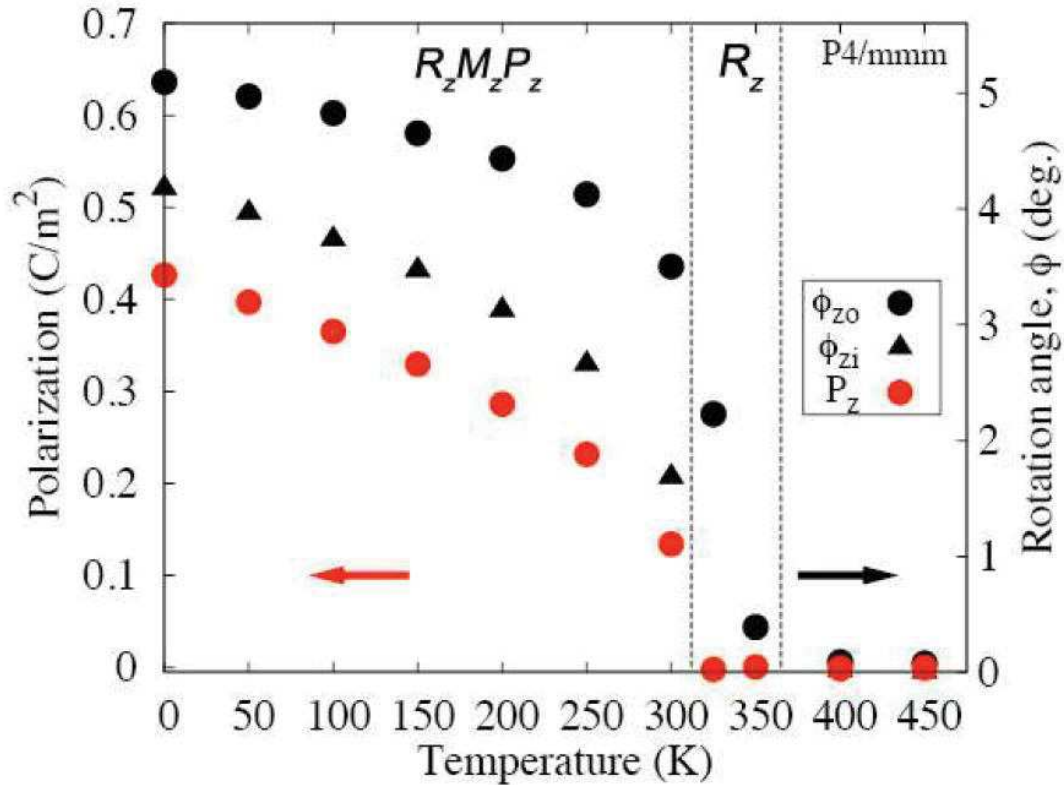


**Figure 2.** Amplitude des modes de distorsion polaires  $P_z$  et de rotation  $\Phi_{zi}$  et  $\Phi_{zo}$  en fonction de la température, calculée par un potentiel modèle couplé à une simulation de type Monte-Carlo, pour le système  $\text{PbTiO}_3/\text{SrTiO}_3$  (1/1).

#### IV. Super-réseaux $\text{ABO}_3/\text{AO}$ artificiels et de type Ruddlesden-Popper.

Le propos est ici de déterminer la délimitation appropriée entre « interface » et couche centrale dans les structures de type Ruddlesden-Popper ou apparentées, afin de pouvoir traiter séparément ces deux sous-parties, et d'obtenir *in fine* une description des propriétés du système complet avec une précision équivalente aux premiers principes.

Les calculs de dispersion et densité d'états de phonons, de charges effectives de Born, de potentiel de Hartree, des constantes de forces inter-atomiques, du tenseur diélectrique ont été effectués par DFT. Il est montré que, vis-à-vis des propriétés structurales et diélectriques, l'effet de l'interface est limité à la première couche d'octaèdres du bloc pérovskite. Au-delà, quelque soit le système étudié ici ( $A = \text{Ba}, \text{Sr}, \text{Pb}$ ), la dynamique de réseau et la structure adoptent le comportement de la pérovskite cubique. Seule l'instabilité ferroélectrique dans la direction perpendiculaire à l'interface nécessite une longueur de corrélation suffisante, quoique réduite, pour apparaître. Cette convergence très rapide des grandeurs étudiées vers les valeurs caractéristiques de la pérovskite, en fonction de la distance à l'interface, permet d'envisager une partition efficace, robuste et transférable des super-réseaux en couches centrales et interfaces. La connaissance « premiers principes » des propriétés de la pérovskite et d'une interface réduite doit alors permettre une description précise des propriétés de super-réseaux complexes.

## V. Super-réseaux PbTiO<sub>3</sub>/SrTiO<sub>3</sub> (m/n).

Les densités d'états de phonons et les constantes de forces inter-atomiques ont été calculées par DFT pour les super-réseaux PbTiO<sub>3</sub>/SrTiO<sub>3</sub> (3/1) et (1/3), puis mises en regard des mêmes grandeurs obtenues pour les pérovskites et pour le système PbTiO<sub>3</sub>/SrTiO<sub>3</sub> (1/1). Il est démontré que ce dernier système décrit très correctement le comportement de l'interface dans les systèmes (3/1) et (1/3), et que la tri-couche centrale possède le même comportement que la pérovskite correspondante (Figure 3). Ces résultats confirment qu'à l'aide d'une partition (interface vs. cœur) et d'un potentiel modèle (dont les paramètres sont calculés par DFT, sur systèmes simples) adaptés, il est possible de décrire le comportement diélectrique de super-réseaux complexes avec une précision égale aux approches de premiers principes, et d'aborder de la même manière les phénomènes aux températures finies.

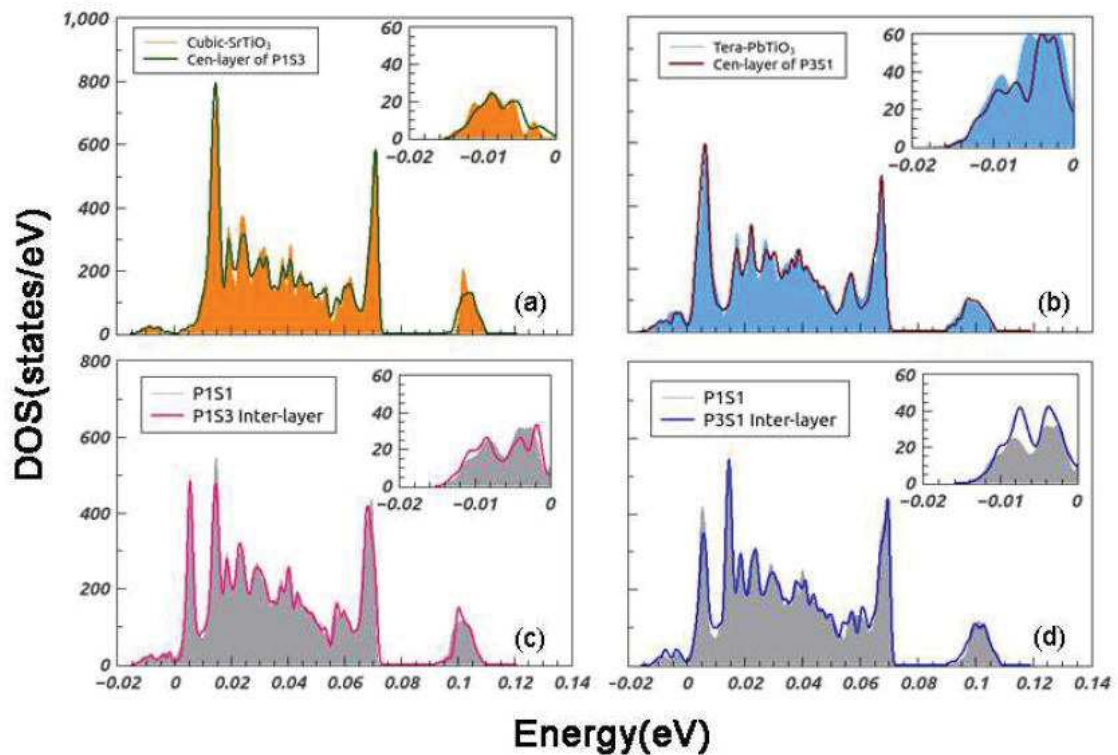


**Figure 3.** Comparaison des densités d'états de phonons calculées pour SrTiO<sub>3</sub>, PbTiO<sub>3</sub> et pour le système PbTiO<sub>3</sub>/SrTiO<sub>3</sub> (1/1), avec les densités d'états partielles obtenues pour le cœur et l'interface des systèmes PbTiO<sub>3</sub>/SrTiO<sub>3</sub> (3/1) et (1/3).

## VI. Conclusion

Ce travail conduit à une méthodologie pour l'étude théorique des propriétés structurales et ferroélectriques de systèmes complexes de type super-réseaux. Cette méthodologie s'appuie tout d'abord sur une partition adaptée des systèmes en régions interfaciales et de cœur. Il est démontré que cette partition est simple, grâce à la convergence rapide des grandeurs calculées lorsqu'on s'éloigne de l'interface. Dans un second temps, il est montré qu'un potentiel modèle peut être construit sur la base de paramètres issus de calculs de premiers principes. Ce potentiel, qui reste à affiner, permet alors l'étude fine de super-réseaux complexes, et de leur comportement en

température via un traitement statistique. Enfin, une approche phénoménologique a permis de reproduire des données expérimentales relatives à une transition de phase ferroélectrique de type impropre, c'est-à-dire faisant intervenir un paramètre d'ordre principal différent de la polarisation. Cette approche montre que des transitions de phase ferroélectriques exotiques, de type impropre, peuvent être mises en évidence en fonction des couplages entre plusieurs paramètres d'ordre, et de leurs températures critiques.

Ce travail ouvre la voie à l'étude de systèmes complexes de type super-réseau, avec une précision équivalente à celle des méthodes de premiers principes (restreintes habituellement à des systèmes relativement simples), et en incluant l'effet de la température. De plus, la méthodologie proposée peut être affinée (potentiel modèle aussi robuste et transférable que possible), et la pertinence des phénomènes exotiques mis en évidence pourra être évaluée par des études théoriques ou expérimentales. Il a été aussi montré des dépendances intéressantes et exploitables des propriétés diélectriques en fonction du champ électrique appliqué et des contraintes.



# *Acknowledgements*

Three years ago, it was my first time to go abroad. Then I had colorful experiences during my PhD studies where I started my research on first-principles. Since then I improved my research ability with the help of many people and had opportunities to share the knowledge at workshops and conferences. Finally I achieved my PhD thesis that I had dreamed of since I was young. It will be an unforgettable experience in my life, definitely. It is a pleasure to thank the many people who made this thesis possible.

First, thanks to the IDS-FunMat program. I could not have had such a wonderful and distinct PhD experience without this impressive project. Please allow me to express my honor to Prof. Jean Etourneau, Prof. Laurent Servant, and to all the organizer of IDS-FunMat. They are working hard for our future young scientists. Thanks to those wonderful spring schools where I met lots of new friends from all over the world. It is my great honor to be a PhD candidate in IDS-FunMat.

It is difficult to overstate my gratitude to my PhD. supervisors, Prof. Philippe Ghosez and Dr. Antoine Villesuzanne who with their enthusiasm, their inspiration, and their great efforts explained things clearly and simply to me. Throughout my thesis, they provided me encouragement and lots of good ideas. Dr. Antoine Villesuzanne was the first French man who talked to me. During the initial period, he helped me to quickly establish my life and research in Europe, including the registrations, the search for an apartment, the application for the resident card, etc.. I would have been quite lost without his help. Thanks to Prof. Philippe Ghosez who gave me an opportunity to join his research group and to present my work in several academic conferences, so that I could quickly go into this research field and learn lots of knowledge from excellent scientists.

I would like to thanks Prof. Matthieu Verstraete for his help on the computational resources, the cluster machines and the tricks in using ABINIT code. Thanks to Dr. Jorge Iniguez for the discussions with you in Liege and in Santander which have been very helpful to my thesis.

Thanks a lot to Dr. Jorge Cors, for supporting my internship in PHASIS. Although it was short, it was an impressive experience in the beautiful city of Geneva.

---

Thanks to Dr. Bin Xu who shared a lot of his research experiences with me. Thanks to Dr. Zeila Zanolli for the help on starting the calculations on *PTO/STO* superlattices as well as Dr. Nicholas Bristowe, people I feel very happy to collaborate with.

Thanks to all my colleagues in Liege and Bordeaux for the friendship and great working atmosphere: Daniel Bilc, Julien Varignon, Hania Djani, Henu Sharma, Begum Kocak, Denis Fontaine, Safari Amisi, Srijan Kumar Saha, Naihua Miao, Alina Prikockyte, Momar Diakhate, Marco di Gennaro, Theodoros Papadopoulos, Osman Baris Malcioglu, Wilfredo Ibarra Hernandez, Qiang Liu, Na Liu, Sbastien Fourcade, Philippe Bellanger, Abdelaadim Danine, Chennabasappa Madhu, Clment Nicollet, Vaibhav Vibhu, Pierre Batocchi, Hongfeng Wang, Na Liu, Qianwen Wu.

I want to thank my physics teacher in middle school, Mr. Zhe Zhou, who gade me an interest in physics and encouraged me to choose physics in university.

I appreciate the support of my wife Minqian Fan during the past three years, also the support for my academic career in the past five years. Thanks to her love for our family.

Here, I must mention my gratitude to my parents here since there is few opportunity to do it during past years. They have been working so hard and sacrificed a lot to take care of me and our family when I was young. That was a long difficult time for them. They keep teaching me to be a good man who is helpful for others. Thanks them for supporting me chose physics as my major subject ten years ago, thanks their support to my academic career although they are not interested in it. My parents do not know anything about what I am doing, the only reason they support me is these are my choices. They must be happy for my achievement of PhD in science, I know it.

在这里我必须感谢我的父母，因为之前我并没有很多这样的机会。在我小时候，他们为了照顾我和家庭努力地工作并且牺牲了很多。那是一段对他们来说很不容易的日子。他们一直以来教育我要做一个能帮助他人的好人。感谢他们十年前对我选择物理学专业的支持，感谢他们一直以来对我学术事业的支持，尽管对物理他们并没有兴趣。我父母完全不懂我所研究的东西，他们支持我的原因仅仅是因为这是我的选择。他们一定会为我获得了博士学位而感到高兴，我知道的。

Finally, I would like to thank myself for the decision I made ten years ago and never give it up.





# Contents

Acknowledgements	i
List of Figures	ix
List of Tables	xv
Introduction	1
<b>1 General background</b>	<b>3</b>
1.1 Introduction	3
1.2 Microscopic origin of ferroelectricity	3
1.3 The $ABO_3$ family of compounds	5
1.3.1 Simple perovskite $ABO_3$ compounds	6
1.3.2 Layered perovskites	9
1.4 Different types of ferroelectricity	13
1.4.1 Proper ferroelectricity	13
1.4.2 Improper ferroelectric	14
1.4.3 Hybrid improper ferroelectricity	16
1.5 Technical approaches	17
1.5.1 First-principles calculations	17
1.5.2 Effective Hamiltonian methods	17
1.5.3 Phenomenological Landau-Devonshire Theory	18
1.6 Motivation	19
<b>2 Theoretical approach</b>	<b>21</b>
2.1 Introduction	21
2.2 Many-body Hamiltonian	21
2.3 Density Functional Theory	23
2.3.1 Kohn-Sham equations	23
2.3.2 Density Functional Perturbation Theory	26
2.4 Practical implementation	27
2.4.1 Exchange-correlation energy	27
2.4.1.1 Local Density Approximation	27
2.4.1.2 Generalized Gradient Approximation	28
2.4.2 Plane-wave basis set	29

2.4.3	Brillouin zone grid . . . . .	29
2.4.4	Pseudopotentials . . . . .	30
2.5	Effective model potential . . . . .	31
2.5.1	$E_p(\{\mathbf{u}_i\})$ . . . . .	31
2.5.2	$E_s(\eta)$ and $E_{sp}(\{\mathbf{u}_i\}, \eta)$ . . . . .	32
2.5.3	Approximation and simulation details . . . . .	34
<b>3</b>	<b><i>PbTiO<sub>3</sub>/SrTiO<sub>3</sub>(1/1)</i> superlattices</b>	<b>35</b>
3.1	Introduction . . . . .	35
3.2	Technical Details of DFT Calculations . . . . .	37
3.3	High-symmetry reference structure . . . . .	38
3.3.1	Relaxed reference structure . . . . .	38
3.3.2	Phonon dispersion curves . . . . .	39
3.3.3	Strain effects . . . . .	41
3.4	Relevant degrees of freedom in ground state . . . . .	43
3.4.1	Energy landscape . . . . .	43
3.4.2	Landau type model . . . . .	44
3.4.3	Temperature dependent Landau model . . . . .	48
3.5	Model potential . . . . .	50
3.5.1	Effective potential training set . . . . .	52
3.5.2	Temperature dependent behavior . . . . .	52
3.6	Conclusion and perspectives . . . . .	57
<b>4</b>	<b>Natural and artificial <i>ABO<sub>3</sub>/AO</i> superlattices</b>	<b>59</b>
4.1	Introduction . . . . .	59
4.2	System of Interest . . . . .	61
4.3	Technical Details of DFT Calculations . . . . .	62
4.4	Relaxed Reference Structure . . . . .	62
4.5	Phonon Dispersion Curves . . . . .	65
4.5.1	<i>Barium Compounds</i> . . . . .	66
4.5.2	<i>Strontium Compounds</i> . . . . .	68
4.5.3	<i>Lead compounds</i> . . . . .	70
4.6	Phonon Density of States . . . . .	75
4.7	Interatomic Force Constants . . . . .	79
4.8	Hartree Potential . . . . .	83
4.9	Born effective charges and dielectric constants . . . . .	84
4.9.1	Born effective charges . . . . .	85
4.9.2	Optical dielectric tensor . . . . .	87
4.10	Conclusion and perspectives . . . . .	90
<b>5</b>	<b><i>PbTiO<sub>3</sub>/SrTiO<sub>3</sub>(m/n)</i> superlattices</b>	<b>93</b>
5.1	Introduction . . . . .	93
5.2	Structures of interest and technical details . . . . .	94
5.3	Structure Relaxation . . . . .	95
5.4	Phonon density of states . . . . .	96

---

5.5	Interatomic force constants . . . . .	98
5.6	Conclusion . . . . .	100
	<b>Conclusions and perspectives</b>	<b>101</b>
	<b>Bibliography</b>	<b>105</b>



# List of Figures

1.1	The ideal structure of $ABO_3$ perovskite compounds . . . . .	5
1.2	Simple $ABO_3$ perovskite compounds cited from Ref.[1]. . . . .	6
1.3	Three types of atomic distortions in perovskite. (a) Polar motion along $z$ axis; (b) in-phase octahedra rotation along $z$ axis; (c) out-of-phase octahedra rotation along $z$ axis. . . . .	7
1.4	Structure evolutions in terms of Goldschmidt tolerance factor $t$ . . . . .	8
1.5	The structure of <i>Ruddlesden-Popper</i> (at the right side) and artificially designed perovskite/rock-salt compounds(at the left side), the number of perovskite layer in each unit cell is from $n=1$ to $3$ . . . . .	11
1.6	Hysteresis loop in ferroelectric materials. $E$ refers to the external electric field and $P$ refers to the polarization. $P_{up}$ and $P_{down}$ correspond to two equivalent spontaneous polarized states with opposite polarization directions. $E_c$ is the depolarization field. . . . .	14
1.7	Energy curve in terms of $P$ , for proper ferroelectric state (blue color) and non-ferroelectric state (red color). . . . .	15
1.8	Energy curver in terms of $P$ for non-ferrelectrics (red line) and improper ferroelectrics (green line, solid and dashed). . . . .	16
3.1	Structure of the <i>PTO/STO(1/1)</i> superlattice. (a) 10 atoms unit cell used in structure optimization and <i>DFPT</i> calculations. (b) 40 atoms super-cell used in the calculation of condensing the $M_{xy}$ mode. (c) 20 atoms super-cell used for condensing most of the unstable phonon modes at the Brillouin zone boundary. . . . .	37
3.2	Unstable phonon modes that correspond to the atomic motion polarized or rotated along $z$ axis in the <i>PTO/STO(1/1)</i> system. (a) The polar mode along $z$ axis( $FE_z$ ) in which $O$ atoms move against cations. (b) The in-phase rotation $\phi_{zi}$ where the two octahedras along $z$ axis rotate in the same direction. (c) The out-of-phase rotation $\phi_{zo}$ where the two octahedras along $z$ axis rotate in the opposite directions. . . . .	38
3.3	Phonon dispersion curves of the <i>(PTO/STO)(1/1)</i> superlattice. The phonon frequencies are presented in the unit of $cm^{-1}$ . The imaginary values are reported as negative ones. . . . .	40

3.4	Phonon frequency (in $cm^{-1}$ ) of selected modes, under different strains, including $P_z$ (black), $P_x$ (red) modes at $\Gamma$ point and $\phi_{zi}$ (green), $\phi_{zo}$ (blue) modes at $R$ point. The imaginary values are reported as negative ones. (a) Strain applied along $z$ direction while the in-plane lattice constant is fixed at the bulk $SrTiO_3$ value. (The strain is defined as $\eta_z = (c_s - c_0)/c_0$ where $c_0$ is the relaxed $z$ component lattice constant of $PTO/STO(1/1)$ and $c_s$ is the $z$ component lattice constant of $PTO/STO(1/1)$ after strain is applied). (b) In-plane strain applied under relaxed $c$ (solid line) and fixed $c$ (dashed line). (The strain is defined as $\eta_{xy} = (a_s - a_0)/a_0$ where $a_0$ is the $x$ component lattice constant which is fixed to the bulk cubic $SrTiO_3$ value and $a_s$ is the $x$ component lattice constant of $PTO/STO(1/1)$ after epitaxial strain is applied). . . . .	42
3.5	The space groups for ground state of $PTO/STO(1/1)$ superlattices under different in-plane strain. The strain is given with respect to the lattice constant of cubic $SrTiO_3$ under zero strain. . . . .	45
3.6	The $1D$ total energy (in $meV/f.u.$ ) curve $E(P_z, \phi_{zi}, \phi_{zo})$ with respect to only one degree of atomic motion: (a) $E(P_z, 0, 0)$ ; (b) $E(0, \phi_{zi}, 0)$ ; (c) $E(0, 0, \phi_{zo})$ ; In the case for which two of these degrees are fixed at the ground state value: (d) $E(P_z, 3.15, 5.04)$ ; (e) $E(0.19, \phi_{zi}, 5.04)$ ; (f) $E(0.19, 3.15, \phi_{zo})$ . . . . .	46
3.7	The $2D$ total energy (in $meV/f.u.$ ) plot $E(P_z, \phi_{zi}, \phi_{zo})$ with respect to two degrees of atomic motion:(a) $E(0, \phi_{zi}, \phi_{zo})$ ; (b) $E(P_z, 0, \phi_{zo})$ ; (c) $E(P_z, \phi_{zi}, 0)$ ;(d) $E(0.19, \phi_{zi}, \phi_{zo})$ ; (e) $E(P_z, 3.15, \phi_{zo})$ ; (f) $E(P_z, \phi_{zi}, 5.04)$ . . .	47
3.8	The amplitude of each distortion mode, in degree for rotation mode (left side) and in $C/m^2$ for polar mode (right side): (a) the amplitude of $\phi_{zi}$ (blue) and $\phi_{zo}$ (purple) modes; (b) the amplitude of $P_z$ (red) and $\phi_{zo}$ (purple) modes; (c) the amplitude of $\phi_{zi}$ (blue) and $P_z$ (red) modes;(d),(e),(f) energy when the three modes coexist (black) and when only one mode exist (brown). . . . .	48
3.9	Different values for $T_1$ , $T_2$ and $T_3$ in equation 3.2: (a) The amplitude of each atomic distortion mode for polarization mode (right axis) and for rotation mode (left axis) under different temperatures when we set $T_1=52K$ , $T_2=500K$ and $T_3=500K$ ; (b) The amplitude of each atomic distortion mode for polarization mode (right axis) and for rotation mode (left axis) under different temperatures when we set $T_1=50K$ , $T_2=490K$ and $T_3=500K$ ; (c) Dielectric constant under different temperatures when we set $T_1=52K$ , $T_2=500K$ and $T_3=500K$ ; (d) Dielectric constant under different temperatures when we set $T_1=50K$ , $T_2=490K$ and $T_3=500K$ . . . . .	50
3.10	Total energy (in $meV$ ) of each intermediate phase, relative to the reference $P4/mmm$ phase, with respect to the scaled mode amplitude which are obtained from model potential. The crosses points indicate the total energy of each intermediate phase obtained from first-principle calculations. . . .	53
3.11	The amplitude of each atomic distortion mode in ( $C/m^2$ ) for polarization mode(red colour) and in degree for rotation mode(black colour) which are reported under different temperature (in $K$ ). . . . .	54

3.12	The amplitude of in-plane(red) and out-of-plane(blue) atomic distortion mode under external electric field(in GV/m) along $z$ direction:(a) the amplitude of in-plane polarization $P_x$ and out-of-plane polarization $P_z$ (in C/m <sup>2</sup> ); (b) the amplitude of in-plane rotation $\phi_{xo}$ and out-of-plane rotation $\phi_{zi}$ and $\phi_{zo}$ (in degree). . . . .	55
3.13	The temperature dependent amplitude of each atomic distortion mode in (C/m <sup>2</sup> ) for polarization mode (red colour) and in degrees for rotation mode(black colour) which are reported under -6.9 GPa pressure along $z$ direction. . . . .	56
4.1	Motivation: We try to estimate the dynamics of large period superlattices from the knowledge of bulk and short period superlattices. The thick superlattices is divided into two parts, the central layer (purple part) and the interface layer (yellow part). We try to demonstrate that we can use the related quantity of the bulk to approximate the central layer of the thick superlattices, and use the related quantity from the short period superlattices to approximate the interface of the thick ones. . . . .	60
4.2	In the case of $AF$ (left side) and $RP$ (right side) superlattices, we label each layer, from <i>layer 0</i> to <i>layer 4</i> ( <i>layer 0</i> only exists in $AF$ series), and define the central perovskite layer (orange part), interface perovskite layer (blue part) and interface rock-salt layer (yellow part). . . . .	61
4.3	The in-plane lattice constant (a) and out-of-plane lattice (c) are shown here. We label each bond (from bond 1 to bond 3) and define the average plane for each layer. The thickness of central perovskite layer ( $c_c$ ) and the one of interface perovskite layer ( $c_i$ ) are defined as well. . . . .	64
4.4	Phonon dispersion curves of bulk cubic $BaTiO_3$ ( $n=\infty$ ) and $Ba$ based superlattices for $AF$ and $RP$ types, $n$ from 1 to 3. The phonon frequencies are presented in units of $cm^{-1}$ . The imaginary values are reported as negative ones. The zero frequency isosurface of bulk cubic $BaTiO_3$ is plotted at the right bottom corner. . . . .	67
4.5	Phonon dispersion curves of bulk cubic $SrTiO_3$ ( $n=\infty$ ) and $Sr$ based superlattices for $AF$ and $RP$ types, $n$ from 1 to 3. The phonon frequency are in units of $cm^{-1}$ . The imaginary values are reported as negative ones. The zero frequency isosurface of bulk cubic $SrTiO_3$ is plotted at the right bottom corner. . . . .	69
4.6	Phonon dispersion curves of bulk cubic $PbTiO_3$ ( $n=\infty$ ) and $Pb$ based superlattices for $AF$ and $RP$ types, $n$ from 1 to 3. The phonon frequency are in the units of $cm^{-1}$ . The imaginary values are reported as negative ones. The zero frequency isosurface of bulk cubic $PbTiO_3$ is plotted at the right bottom corner. . . . .	72
4.7	Amplitude of unstable polar phonon motion in the arbitrary units. Here, mode 1 refers the lowest unstable phonon mode and mode 2 refers the second lowest one. The data are selected from $Pb$ and $Ba$ based superlattices for $n=2$ . . . . .	74

4.8	Phonon density of states ( <i>DOS</i> ) of <i>Ba</i> based superlattices, in the case of $n=3$ for <i>AF</i> and <i>RP</i> types. The region of imaginary frequencies is zoomed in insets. The gray color part refers the phonon <i>DOS</i> of the bulk cubic <i>BaTiO<sub>3</sub></i> , the red line indicates the phonon <i>DOS</i> contribution of the interface perovskite layer in superlattices while the blue line indicates the phonon <i>DOS</i> contribution of the central perovskite layer in superlattices . . . . .	75
4.9	Phonon density of states ( <i>DOS</i> ) of <i>BaO</i> layer, in the case of $n=3$ for <i>AF</i> and <i>RP</i> types superlattices. The gray color part refers the phonon <i>DOS</i> of interface perovskite layer in superlattices, the red line indicates the phonon <i>DOS</i> contribution of the <i>BaO</i> layer in central perovskite layer in superlattices while the blue line indicates the phonon <i>DOS</i> contribution of the bulk rock-salt <i>BaO</i> . . . . .	76
4.10	Phonon density of states ( <i>DOS</i> ) of <i>Sr</i> based superlattices, in the case of $n=3$ for <i>AF</i> and <i>RP</i> types. The region of imaginary frequencies is zoomed in insets. The green color part refers the phonon <i>DOS</i> of the bulk cubic <i>SrTiO<sub>3</sub></i> , the red line indicates the phonon <i>DOS</i> contribution of the interface perovskite layer in superlattices while the blue line indicates the phonon <i>DOS</i> contribution of the central perovskite layer in superlattices. . . . .	77
4.11	Phonon density of states ( <i>DOS</i> ) of <i>Pb</i> based superlattices, in the case of $n=3$ for <i>AF</i> and <i>RP</i> types. The region of imaginary frequencies is zoomed in insets. The green color part refers the phonon <i>DOS</i> of the bulk cubic <i>PbTiO<sub>3</sub></i> , the red line indicates the phonon <i>DOS</i> contribution of the interface perovskite layer in superlattices while the blue line indicates the phonon <i>DOS</i> contribution of the central perovskite layer in superlattices . . . . .	78
4.12	Interatomic Force Constant ( <i>IFC</i> ) induced on <i>Ti</i> atom in bulk cubic <i>BaTiO<sub>3</sub></i> and <i>Ba</i> based superlattices, <i>AF</i> and <i>RP</i> types. The <i>IFC</i> values depend on different atoms and atomic distances with reference <i>Ti</i> atom. Atoms differ by colors, green for <i>Ti</i> , blue for <i>Ba</i> and black for <i>O</i> . . . . .	82
4.13	Difference between the interatomic force constant ( <i>IFC</i> ) induced on <i>Ti</i> atom in bulk cubic <i>BaTiO<sub>3</sub></i> and the ones induced on <i>Ti</i> atom in superlattices. The values depend on different atoms and atomic distances with reference <i>Ti</i> atom. Atom differ by colors, green for <i>Ti</i> , blue for <i>Ba</i> and black for <i>O</i> . . . . .	82
4.14	Hartree Potential in 3-layers <i>BTO</i> . a) Dipole created by <i>Ti</i> atom in interface layer, moved along $z$ ; b) Dipole created by <i>Ti</i> atom in central layer, moved along $z$ ; c) Hartree potential of 3-layers <i>BTO</i> ; d) Dipole created by <i>Ti</i> atom in interface layer, moved along $x$ ; e) Dipole created by <i>Ti</i> atom in central layer, moved along $x$ ; f) Structure of 3-layers <i>BTO</i> supercell . . . . .	84
5.1	<i>PTO/STO(m/n)</i> superlattices with different periods. (a) <i>PTO/STO(1/1)</i> ; (b) <i>PTO/STO(1/3)</i> ; <i>PTO/STO(3/1)</i> . Layers are labeled from layer 1 to layer 5 and the <i>Ti-O</i> bonds are labeled from bond 1 to bond 4. $C_c$ refers to the thickness of central layer, $C_i$ refers to the thickness of interface layer and $C$ is lattice constant along $z$ . . . . .	94

5.2	Phonon density of states( <i>DOS</i> ) of interface and central layer in <i>P1S3</i> and <i>P3S1</i> cases and the <i>DOS</i> for bulk. (a) bulk cubic <i>SrTiO<sub>3</sub></i> (orange) and central layer in <i>P1S3</i> (green line); (b) bulk tetragonal <i>PbTiO<sub>3</sub></i> (light blue ) and central layer in <i>P3S1</i> (brown line); (c) <i>P1S1</i> case (gray) and the interface layer in <i>P1S3</i> (pink line); (d) <i>P1S1</i> case (gray) and the interface layer in <i>P3S1</i> (dark blue line). . . . .	97
5.3	Interatomic force constant ( <i>IFC</i> ) for each <i>Ti</i> atom in <i>PTO/STO(m/n)</i> ( <i>P1S3</i> and <i>P3S1</i> ) superlattices, bulk cubic <i>SrTiO<sub>3</sub></i> and bulk tetragonal <i>PbTiO<sub>3</sub></i> and the difference of <i>IFC</i> values. (a) Distribution of <i>IFC</i> for <i>Ti</i> atom in bulk cubic <i>SrTiO<sub>3</sub></i> ; (b) Distribution of <i>IFC</i> for <i>Ti</i> atom in central layer of <i>P1S3</i> ; (c) Difference of <i>IFC</i> between the <i>Ti</i> values in (b) and the ones in (a); (d) Distribution of <i>IFC</i> for <i>Ti</i> atom in bulk tetragonal <i>PbTiO<sub>3</sub></i> ; (e) Distribution of <i>IFC</i> for <i>Ti</i> atom in central layer of <i>P3S1</i> ; (f) Difference of <i>IFC</i> between the <i>Ti</i> values in (e) and the one in (d). . . . .	98
5.4	Interatomic force constants ( <i>IFC</i> ) for each <i>Ti</i> atom in <i>P1S1</i> ( <i>P1S3</i> , <i>P3S1</i> and <i>P1S1</i> ) superlattices, and the difference of <i>IFC</i> between them. (a) Distribution of <i>IFC</i> for <i>Ti</i> atom <i>P1S1</i> ; (b) Distribution of <i>IFC</i> for <i>Ti</i> atom in interface layer of <i>P1S3</i> ; (c) Difference of <i>IFC</i> between the <i>Ti</i> values in (b) and the one in (a); (d) Distribution of <i>IFC</i> for <i>Ti</i> atom in <i>P3S1</i> ; (e) Difference of <i>IFC</i> between the <i>Ti</i> values in (d) and the ones in (a). . . . .	99



# List of Tables

2.1	Physical quantities obtained from the first and the second order derivatives of the total energy with respect to atomic positions $\mathbf{R}$ , homogeneous strains $\eta$ and electric field $\xi$ . . . . .	27
3.1	Relaxed lattice constants (in Å) of <i>PTO/STO(1/1)</i> superlattices, bulk <i>PbTiO<sub>3</sub></i> and bulk <i>SrTiO<sub>3</sub></i> from calculations and experiment . . . . .	39
3.2	Energy convergence of <i>PTO/STO(1/1)</i> superlattice with different k-grid (in <i>meV/f.u.</i> ). The energy is reported as the value relative to the $8 \times 8 \times 8$ <i>k-grid</i> case. . . . .	39
3.3	Frequency (in $cm^{-1}$ ) of each unstable phonon mode, at the center and boundaries of Brillouin zone, for <i>PTO/STO(1/1)</i> superlattice under zero strain. The imaginary values are reported as negative ones. . . . .	41
3.4	Amplitude of $P_z$ $\phi_{zi}$ and $\phi_{zo}$ atomic motions for each selected phase (corresponding to the polar or rotation motion along $z$ axis) and energy gain (in <i>meV/f.u.</i> ) with respect to the $P_4/mmm$ phase of <i>PTO/STO(1/1)</i> superlattice. . . . .	44
3.5	Parameters of the model described in the text in the standard unit. . . . .	46
3.6	Energy (in <i>meV/f.u.</i> ) of <i>PTO/STO(1/1)</i> superlattice, for $P_4/mmm$ phase, and intermediate phases in the case of relaxed and fixed $z$ component lattice constants under zero in-plane strain. the values are obtained by <i>DFT</i> calculations (using the <i>LDA</i> approximation) and from the effective model potential $E_{eff}$ . The error between them is in the last column. . . . .	51
4.1	In-plane lattice constant (a), out-of-plane lattice constant (c), thickness of interface perovskite layer ( $c_i$ ) and the thickness of central perovskite layer ( $c_c$ ) under zero epitaxial strain of <i>Ba,Sr</i> and <i>Pb</i> based superlattices for <i>AF</i> and <i>RP</i> types (in Å). . . . .	65
4.2	Rumpling in interface perovskite layers, which is defined as the displacement along $z$ between cations and oxygen atoms ( $R_{aver}=(z_{cat}-z_O)/2$ ), of <i>Ba, Sr</i> and <i>Pb</i> based superlattices for <i>AF</i> and <i>RP</i> types (in Å). . . . .	65
4.3	<i>Ti-O</i> bond lengths of <i>Ba,Sr</i> and <i>Pb</i> based superlattices for <i>AF</i> and <i>RP</i> types (in Å). Each bond is defined in figure 4.3. . . . .	66
4.4	Phonon frequency of the lowest unstable mode (in $cm^{-1}$ ) of <i>Ba,Sr</i> and <i>Pb</i> based superlattices for <i>AF</i> and <i>RP</i> types. . . . .	70
4.5	Phonon frequency of the $FE_z$ and $AFD_{zo}$ mode in <i>PTO</i> ( $cm^{-1}$ ) . . . . .	73

4.6	The $z$ component on-site force constant for $Ti$ and A site atoms and the component along $Ti-O$ chain of on-site force constant for $O$ atoms (in $Ha./Bohr^2$ ) of $Ba, Sr$ and $Pb$ based superlattices in $AF$ and $RP$ types. $TT$ refers the total part of the force constants and $SR$ refers the short range part. $O_{xy}$ and $O_z$ refers to the equatorial and apical oxygen atoms in the $TiO_6$ octahedra. . . . .	81
4.7	$Z^*$ in bulk cubic perovskite and rock-salt oxides (in $ q_{e-} $ ), $\perp$ refers the direction perpendicular to the $x-y$ plane, $\parallel$ refers the direction parallel to the $x-y$ plane. . . . .	85
4.8	$Z^*$ of atoms (in $ q_{e-} $ ) in $Ba, Sr$ and $Pb$ based superlattices of $AF$ and $RP$ types. $\perp$ refers the direction perpendicular to the $x-y$ plane, $\parallel$ refers the direction parallel to the $x-y$ plane. Notations are defined in the main text. . . . .	86
4.9	$Z^*$ of $O$ atoms (in $ q_{e-} $ ) in $Ba, Sr$ and $Pb$ based superlattices of $AF$ and $RP$ types. $\parallel_{Ti-O}$ refers the direction along $Ti-O$ bond, $\perp_1$ and $\perp_2$ refer to the other two directions perpendicular to $\parallel_{Ti-O}$ . . . . .	87
4.10	Dielectric constant in superlattices, bulk cubic perovskite and bulk rock-salt oxides. $z$ refers to the component along $z$ and $x-y$ refers to the component along $x-y$ plane. . . . .	89
4.11	Effective dielectric constant ( $\epsilon'_z$ ), dielectric constant ( $\epsilon_z$ ) and the relative difference between them ( $(\epsilon'_z - \epsilon_z)/\epsilon_z$ ) in $AF$ type of $Ba, Sr$ and $Pb$ based superlattices. . . . .	89
4.12	Effective dielectric constant ( $\epsilon'_z$ ), dielectric constant ( $\epsilon_z$ ) and the relative difference between them ( $(\epsilon'_z - \epsilon_z)/\epsilon_z$ ) in $RP$ type of $Ba, Sr$ and $Pb$ based superlattices. . . . .	90
5.1	The lattice constant $C$ (along $z$ ) for $PTO/STO(m/n)$ ( $P1S3, P3S1$ and $P1S1$ ), bulk cubic $SrTiO_3$ and bulk tetragonal $PbTiO_3$ . Thickness of central layer $C_c$ , and interface layer $C_i$ (in $\text{\AA}$ ). . . . .	95
5.2	Value of rumpling for each layer in $PTO/STO(m/n)$ superlattices ( $P1S3, P3S1$ and $P1S1$ ) (in $\text{\AA}$ ). Each layer is labeled in Figure 5.1. . . . .	96
5.3	$Ti-O$ bond lengths along $z$ in $PTO/STO(m/n)$ superlattices ( $P1S3, P3S1$ and $P1S1$ ) and bulk (in $\text{\AA}$ ), Each bond is labeled in Figure 5.1. . . . .	96

# Introduction

Ferroelectricity has attracted intensive research interest since it was discovered in 1920. With the time passing, various ferroelectric materials were identified. There exists a huge experimental data and different theories were proposed to describe and explain this phenomenon. Nowadays, ferroelectric materials are widely used in technological applications, from space shuttles to Iphone 5... Perovskite type compounds of chemical formula  $ABO_3$ , is an important group of materials that exhibit ferroelectric properties for  $B=Ti, Nb, Ta, \dots$ . Perovskite materials also exhibit plenty of other behaviors, like superconducting properties, ferromagnetism, multiferroism etc., that attracted much interest during the recent years.

The aim of the present thesis is to investigate, from first-principles, the ferroelectric properties and related phase transition behaviors in perovskite type compounds. We will not focus only on the bulk perovskite systems, but also on related layered superlattices where the interface may play an important role and induce new phenomena. Our study is organized as follows.

In a first part, we will overview the general framework of the present thesis. In Chapter 1, we will briefly introduce the background knowledge on ferroelectricity in perovskite compounds, from bulk systems to different types of layered systems. Different types of ferroelectricity will be introduced, including proper ferroelectricity, improper ferroelectricity and hybrid improper ferroelectricity. In Chapter 2, the theoretical scheme that was used for all the calculations in this thesis will be described, including the density functional theory (DFT) and a new type of first-principles based model atomic potentials.

In Chapter 3, we will focus on the investigation of the ferroelectric phase transition behaviors of  $PbTiO_3/SrTiO_3$  superlattices. Based on the data of DFT calculations, a Landau type model will be developed and a new model atomic potentials will be fitted providing access to finite temperature properties.

---

In Chapter 4, based on the DFT calculations for different types of  $ABO_3/AO$  superlattices, we will study the possibility of transferring our model potential from short period superlattices to larger systems. Our investigation will mainly focus on the dynamical properties of these systems. Finally, we will apply a similar approach to thicker  $PTO/STO(m/n)$  systems in Chapter 5.

# Chapter 1

## General background

### 1.1 Introduction

The main object of this thesis is to investigate from first-principles the ferroelectric properties of superlattices derived from well known titanium based  $ABO_3$  compounds and to explore the possibility of building effective potentials providing access to the finite temperature properties of short and long period superlattices. The aim of this chapter is to briefly introduce the background of the present thesis. First, we will introduce some aspects of the microscopic origin of the ferroelectric instability. Then we will briefly introduce the  $ABO_3$  series of compounds from bulk systems to superlattices, We will highlight the competition between different structural instabilities yielding different phase transitions sequences. In the third part, we will introduce some theoretical approaches commonly used in this field. At last, we will explain our motivation and the organization of the present thesis.

### 1.2 Microscopic origin of ferroelectricity

A theoretical explanation of the microscopic origin of ferroelectricity was first proposed by Cochran [2] in 1960: the soft phonon mode concept was first introduced and became the central quantity to describe the lattice instability and phase transition. In the framework of the soft mode picture, the ferroelectric phase transition is driven by a polar transverse optical mode which progressively softens and finally condenses into the structure below the phase transition temperature. As a consequence, a finite

polarization occurs, that can be characterized by an hysteretic loop under an applied electric field.

The lattice dynamical equation of a crystal can be written as follows, under the harmonic approximation:

$$\sum_{\kappa'\beta} \tilde{D}_{\kappa\alpha,\kappa'\beta}(\vec{q}) \gamma_{m\vec{q}}(\kappa'\beta) = \omega_{m\vec{q}}^2 \gamma_{m\vec{q}}(\kappa\alpha) \quad (1.1)$$

where  $\kappa$  and  $\kappa'$  indicate different atoms,  $\alpha$  and  $\beta$  label the displacement direction,  $\omega_{m\vec{q}}$  is the phonon frequency of mode  $m$  with the wave vector of  $\vec{q}$ ,  $\gamma_{m\vec{q}}$  is the phonon eigenvector which corresponds to the phonon displacement  $\eta_{m\vec{q}} = \sqrt{M} \gamma_{m\vec{q}}$ . The dynamical matrix  $\tilde{D}_{\kappa\alpha,\kappa'\beta}$  is defined as:

$$\tilde{D}_{\kappa\alpha,\kappa'\beta}(\vec{q}) = \frac{1}{\sqrt{M_\kappa M_{\kappa'}}} \tilde{C}_{\kappa\alpha,\kappa'\beta}(\vec{q}) \quad (1.2)$$

Here,  $\tilde{C}_{\kappa\alpha,\kappa'\beta}(\vec{q})$  is the Fourier transform of the interatomic force constants (*IFC*) in real space [3].

$$C_{\kappa\alpha,\kappa'\beta}(l, l') = \frac{\partial^2 E}{\partial \tau_{\kappa\alpha}(l) \partial \tau_{\kappa'\beta}(l')} \quad (1.3)$$

where  $l$  and  $l'$  label the unit cells,  $\tau$  is the displacement of the atom  $\kappa$  in unit cell  $l$  along the directions labeled by  $\alpha$  and  $\beta$ .

In a stable phase, the atomic positions will correspond to a minimum of energy. The curvature of energy vs. any displacement and consequently the value of  $\omega^2$  of all phonon modes are positive. In this case any atomic motion will increase the total energy of the lattice. When a phase is unstable, the curvature for some peculiar atomic motions and the related value of  $\omega^2$  are negative. Here, the frequency  $\omega$  will consequently be imaginary. The computation of phonons for a high symmetry phase allows identifying the lattice instabilities and reveals an important technique in the research for phase transitions in ferroelectrics.

In  $BaTiO_3$ , first-principles calculations reproduce an unstable polar mode in the cubic phase. This mode has an overlap of 99% with the atomic distortion taking place at the phase transition from the cubic to the tetragonal phase, illustrating the relevance of the soft mode theory of Cochran in this class of compounds.

Cochran further explained the origin of the instability of the ferroelectric soft mode from a competition between short-range forces stabilizing the cubic structure and long-range electrostatic interactions destabilizing the structure. This basic idea was checked and validated at the first-principles level in perovskite compounds. In that context, it appeared that the giant Born effective charges related to dynamical transfer of charges between  $O$   $2p$  and  $B$  atom  $d$  levels in perovskite compounds was a key ingredient to produce a dipolar interaction sufficiently large to destabilize the crystal.

### 1.3 The $ABO_3$ family of compounds

The widely investigated  $ABO_3$  cubic perovskite compounds have crystal structures related to the mineral *perovskite*  $CaTiO_3$  which was discovered by Gustav Rose in 1839 and named as *perovskite* in honor of the eminent Russian mineralogist, Count Lev Alexevich von Perovski [4]. Figure 1.1 shows the basic structure of ideal  $ABO_3$  compounds, which is cubic with space group  $Pm\bar{3}m(221)$ . This cubic phase observed in most compounds at high temperature is paraelectric. When the temperature decreases, these compounds may undergo different types of polar or non-polar structural phase transitions. In this part, we will briefly introduce the background of  $ABO_3$  compounds, from bulk to superlattices.

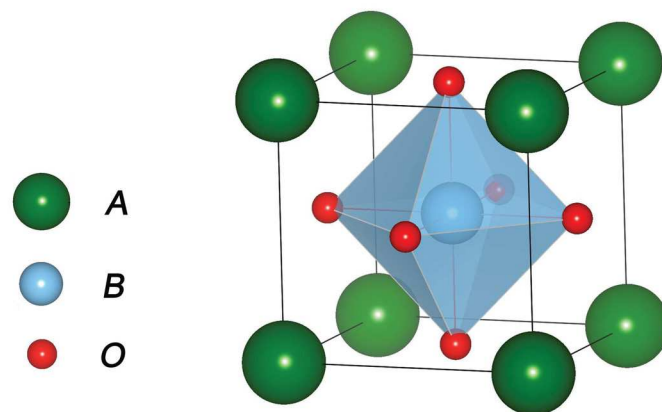


FIGURE 1.1: The ideal structure of  $ABO_3$  perovskite compounds

### 1.3.1 Simple perovskite $ABO_3$ compounds

The broad range behavior of  $ABO_3$  compounds refers to different types of  $A$  and  $B$  site cations. As it is reviewed in Refs. [1, 5, 6], the  $ABO_3$  family compounds present various physical properties, from insulator to conductor and superconductor, from ferroelectric ( $FE$ ) to ferromagnetic and multiferroic, from antiferro-distorted ( $AFD$ ) to orbital ordered etc. In this present thesis, we will mainly focus on the ferroelectric property of perovskite material.

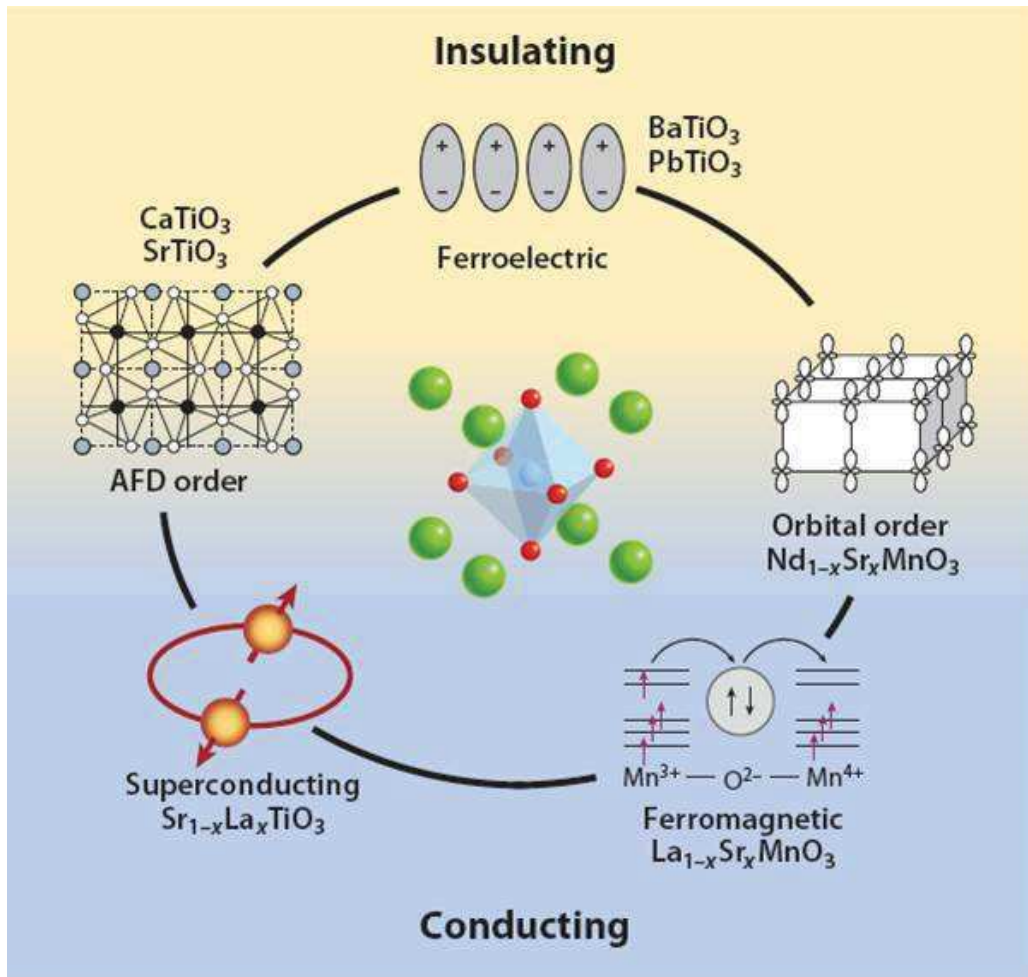


FIGURE 1.2: Simple  $ABO_3$  perovskite compounds cited from Ref.[1].

There are two basic types of atomic motions in perovskite materials that correspond to these phase transitions (shown in Figure1.3). The first one is the atomic polar motion, where cations move against oxygens (the ferroelectric phase transition); the second one is the tilts of oxygen octahedra, which correspond to the non-polar antiferro-distorted phase transition. We will introduce, in more details, these two types of motions in Chapter 3.

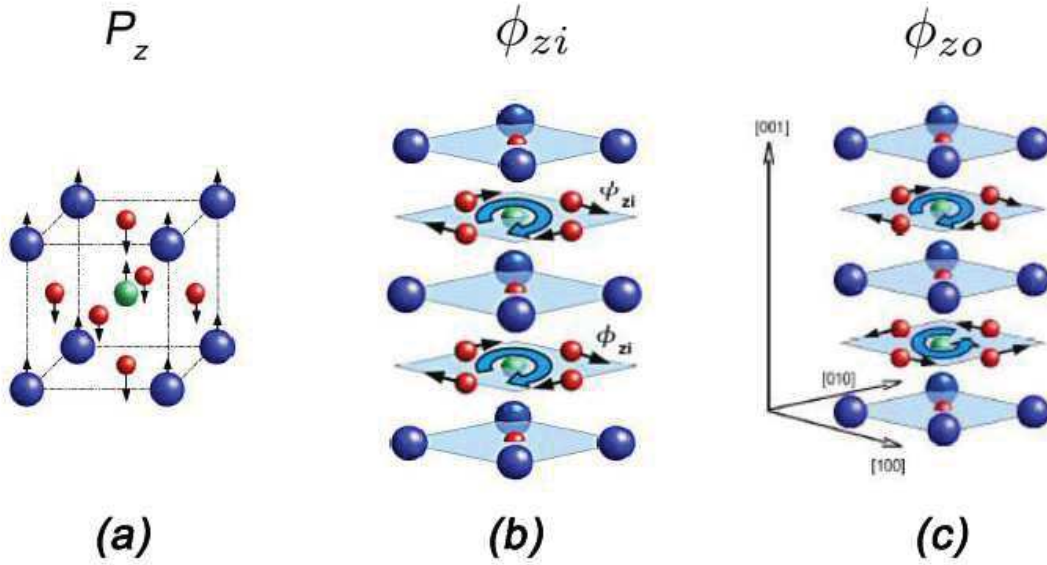


FIGURE 1.3: Three types of atomic distortions in perovskite. (a) Polar motion along  $z$  axis; (b) in-phase octahedra rotation along  $z$  axis; (c) out-of-phase octahedra rotation along  $z$  axis.

The tendency of perovskite compounds to be either ferroelectric or antiferrodistorted is related to the so-called Goldschmidt tolerance factor:

$$t = \frac{R_A + R_O}{\sqrt{2}(R_B + R_O)} \quad (1.4)$$

where  $R_A$ ,  $R_B$  and  $R_O$  are the ionic radii of  $A$ ,  $B$  and  $O$  atoms. Generally, as it is shown in Figure 1.4:  $t=1$  leads to the ideal cubic perovskite structure; distorted perovskite exist in the range  $0.85 < t < 1.1$ , beyond those limits the system will be in other structures. In the range of  $0.85 < t < 1.1$ : when  $t > 1$ , the  $B$  site atom is relatively small so that the system has a tendency to develop a polar distortion; when  $t < 1$ , the  $A$  site atom is relatively small and the tilting of the oxygen octahedra will be favored.

$BaTiO_3$  is a well known perovskite material, the ferroelectric property of which was found accidentally in 1945 [7]. Three phase transitions are observed: i) at  $T \simeq 130^\circ\text{C}$ , the system switches from cubic ( $Pm\bar{3}m(221)$ ) to tetragonal ( $P4mm(99)$ ) phase in which the spontaneous polarization appears along  $z$  axis; ii) an orthorhombic phase ( $Pmm2(25)$ ) is observed below  $T \simeq 0^\circ\text{C}$  where the spontaneous polarization is along the  $[011]$  direction; iii) when the temperature decreases below  $T \simeq -80^\circ\text{C}$ , the rhombohedral phase appears and the polarization will be switched to the  $[111]$  direction.

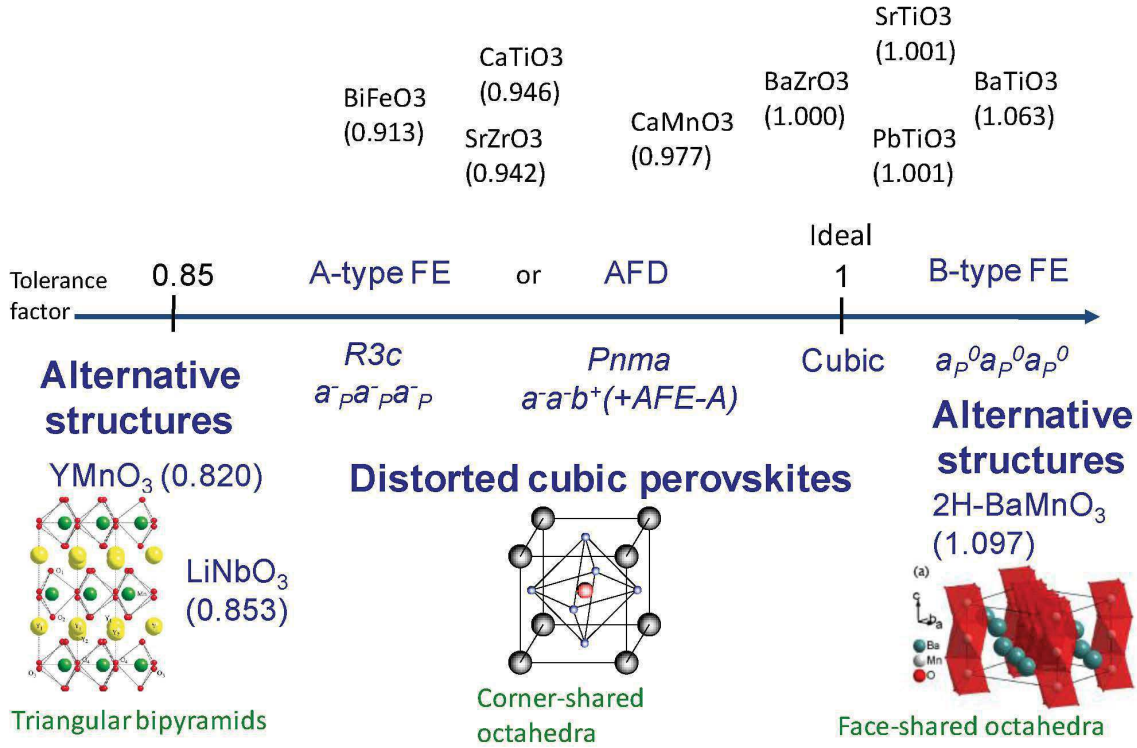


FIGURE 1.4: Structure evolutions in terms of Goldschmidt tolerance factor  $t$ .

Another perovskite compound,  $KNbO_3$ , shows the same phase transitions sequence starting at 710 K [7].  $PbTiO_3$  has a ferroelectric ground state as well, but it is of tetragonal symmetry.

$SrTiO_3$  is another remarkable perovskite material, the ground state of which is characterized by the tilts of oxygen octahedra, i.e. a non-polar antiferro-distorted ( $AFD$ ) state. At the temperature  $T \simeq 100$  K,  $SrTiO_3$  is switched from cubic to a  $AFD$  non-polar tetragonal phase in which the octahedra rotates around the tetragonal axis. Nevertheless,  $SrTiO_3$  can transform to a ferroelectric phase under strain at room temperature [8]. The suppressed ferroelectric phase transition under zero strain is due to quantum fluctuations [9]. This non-polar behavior also appears in other  $ABO_3$  compounds e.g.  $CaTiO_3$  [10, 11],  $KTaO_3$  [12, 13]...which are called incipient ferroelectrics (or quantum ferroelectrics).

These two types of ferroic orders can coexist in some perovskite material e.g.  $BiFeO_3$  [14, 15] and  $CaMnO_3$  [16]. It is worth to mention that, in  $CaMnO_3$ , the ferroelectricity and the magnetism are not necessarily exclusive but can be driven by the same cation. Moreover, other type of atomic distortions can exist in  $ABO_3$  perovskite compounds such as the anti-ferroelectric phase of  $PbZrO_3$  [17, 18].

### 1.3.2 Layered perovskites

Beyond the bulk phases, layered perovskites, in which oxides with different compositions or structures are stacked together, can also exhibit rich interesting phenomena. Some of the properties in complex superlattices are bulk-like while some of them are completely new and specific. Typically, interfaces play a key role in driving new physics in superlattices by modifying the electrostatic boundary condition, breaking symmetry, inducing epitaxial strain etc. [1, 19–21].

For instance, at any interface between two materials which have different chemical potentials, charge transfer will be allowed. Charge transfer in  $CaMnO_3/CaRuO_3$  systems results in a ferromagnetic interface from which finite charge transfer between these layers can be deduced [22]. It is interesting to see that without real charge transfer, geometric control of virtual charge exchange can completely alter the magnetic properties [19, 23, 24]. Furthermore, the interface between materials with different valence states at the  $B$  site in the superlattice composed of  $SrTi^{4+}O_3$  and  $LaTi^{3+}O_3$  makes the system exhibit metallic behavior [25]. In  $LaAlO_3/SrTiO_3$  ( $LAO/STO$ ) systems, a “2-dimensional-electron-gas” (2DEG) appears at the interface on the  $STO$  side when the  $LAO$  film thickness exceeds 3 unit cells [26]. These experimental results have attracted a lots of interest and research activity [27] and many exciting properties related to this 2DEG have been observed [26, 28, 29].

Due to the strong polarization-strain coupling in perovskite compounds, the superlattice system is highly sensitive to the epitaxial strain generated at the interface when the two basic materials have different lattice parameters. It has been preliminarily demonstrated that epitaxial strain can be used to induce ferroelectricity [8], multiferroicity [16], and to create strongly coupled multiferroics [30]. Strain engineering has become a popular method for controlling the lattice instabilities, atomic distortions and tuning the ground state between different phases [31–34].

Here, we would like to briefly introduce the selected types of layered perovskites which are relevant in the present thesis.

#### ***Ruddlesden-Popper* compounds**

*Ruddlesden-Popper* ( $RP$ ) compounds form a series of naturally layered perovskites (intrinsic superlattices) with the general formula  $(ABO_3)_n/(AO)$  as first proposed by

S.N. Ruddlesden and P. Popper in 1958 [35]. As it is shown in Figure 1.5, the typical structure of *Ruddlesden-Popper*  $((ABO_3)_n/(AO))$  compounds is based on perovskite layers connected by a single unit cell *rock-salt* layer. At each interface, the  $ABO_3$  layer is shifted along [110] direction by  $(1/2, 1/2)$  lattice constant. Bulk  $ABO_3$  compounds can be considered as the *RP* compound with infinite value of  $n$ . The first member ( $n=1$ ) corresponds to the  $K_2NiF_4$ -type structure.

It is interesting to see that *Ruddlesden-Popper* compounds can exhibit properties distinct from these of related  $ABO_3$  materials. The rock-salt interface breaks the continuity of the  $B-O$  bond chains along  $z$  and suppresses ferroelectric instabilities in these series of superlattices, along the stacking direction. In  $(CaTiO_3)_n/(CaO)$  and  $(SrTiO_3)_n/(SrO)$  series of compounds, no tendency to ferroelectric behavior is observed for short periodic members (mentioned in Ref. [36]). To reactivate the ferro electric order, one option is to increase the thickness of perovskite layers; another method is to modify the structure of the interface as demonstrated in the  $(SrTiO_3)_n/(SrO)$  series from first-principles [37]. The series of  $(SrRuO_3)_n/(SrO)$  compounds is another interesting member of *Ruddlesden-Popper* type superlattices; the  $n=1$  member is an unconventional superconductor [38], the  $n=2$  member exhibits metamagnetism and quantum criticality [39–41], and for higher value of  $n$ , ferromagnets with rather complicated magnetic and transport properties are found [42–44]. Similar interesting phenomena were observed in the  $(CaRuO_3)_n/(CaO)$  series compounds as well [45–49].

Besides those example, some other interesting observation in *Ruddlesden-Popper* compounds are worth mentioning here: the first member of the  $(SrTiO_3)_n/(SrO)$  series compounds was reported having a large dielectric constant [50]; the first member of  $(PbTiO_3)_n/(PbO)$  series was predicted having in-plane ferroelectric properties [36]; hybrid improper ferroelectricity is predicted in  $(CaMnO_3)_n/(CaO)$  from first principles [51].

### $(ABO_3)_n/(AO)_m$ superlattices

In close connection with the *Ruddlesden-Popper* compounds, the artificially designed  $(ABO_3)_n/(AO)_m$  ( $m>1$ ) compounds alternate perovskite and rock-salt materials. The basic structure is shown in Figure 1.5. The *Ruddlesden-popper* compounds can be considered as the  $m=1$  members of this series.

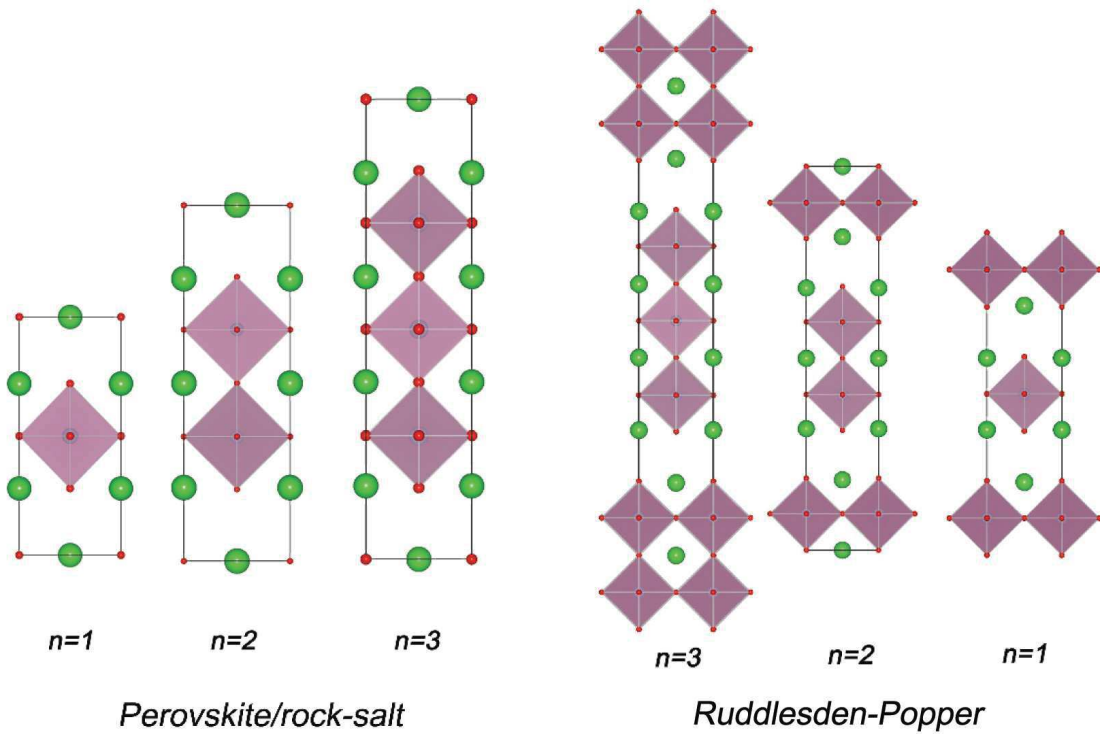


FIGURE 1.5: The structure of *Ruddlesden-Popper* (at the right side) and artificially designed perovskite/rock-salt compounds (at the left side), the number of perovskite layer in each unit cell is from  $n=1$  to 3.

It has been experimentally demonstrated that perovskite compounds can be grown on silicon substrates [52]. The case  $m=6$  and  $n=5$  for  $(BaTiO_3)_n/(BaO)_m$  and  $(SrTiO_3)_n/(SrO)_m$  has been investigated from first-principles [53]. The authors concluded that, at the interface, epitaxial strain exists and the atomic rumpling is localized in this region. There was no ferroelectric behavior predicted in this system. Furthermore, the ferroelectric and antiferroelectric instabilities in  $(BaTiO_3)_n/(BaO)_m$  was studied later from first-principles [54]; it was shown that different ferroic orders compete in such superlattices. In this work,  $(BaTiO_3)_n/(BaO)_m$  was assumed to be grown on a  $SrTiO_3$  substrate thus fixing the in-plane lattice constant as the one of bulk  $SrTiO_3$ , so that in-plane strain was induced. It was concluded that although  $BaTiO_3$  is ferroelectric at bulk level, such type of superlattices can present an antiferroelectric ground state at short  $BaTiO_3$  thicknesses due to the depolarizing field, inherent to the electrical boundary conditions. The epitaxial strain plays also as a key role by tuning the competition between ferroelectric and antiferroelectric orders.

**$ABO_3/A'B'O_3$  superlattices**

$ABO_3/A'B'O_3$  artificial superlattices is another series of remarkable and widely investigated system, based on the same perovskite structure but different compositions. Often ferroelectric and paraelectric compounds are combined. Different options provide an exciting opportunity for the design of artificial materials with tunable properties.

$BaTiO_3/SrTiO_3$  is an interesting example which has been widely discussed in the literature [55–61]. It was proposed from first-principles that, when the in-plane lattice constant is fixed to the bulk  $SrTiO_3$  value, the compressive strain enhances the out-of-plane polarization in  $BaTiO_3$  layers [62, 63]. A uniform polarization then develops in the whole superlattice,  $BaTiO_3$  forcing a polarization in  $SrTiO_3$ , since any polarization mismatch at interface would cause large depolarization fields with a large energy cost. This homogeneous polarization phenomenon is expected in short period superlattices [64] while various domain patterns can appear in larger systems. It is also observed that the in-plane component of polarization can appear in  $SrTiO_3$  layers under specific strain conditions [56, 65–67]. Similar investigations and arguments were applied to  $KNbO_3/KTaO_3$  superlattices [68, 69]. It is worth to mention that in  $(KNbO_3)_n/(KTaO_3)_n$ , when  $n < 6$ ,  $KNbO_3$  layers are strongly coupled with each other while they behave essentially independently when  $n$  is larger than 12, which is confirmed both theoretically and experimentally [70, 71].

The  $PbTiO_3/SrTiO_3$  system is another remarkable ferroelectric/paraelectric superlattice which can be grown experimentally using molecular beam epitaxy (MBE) [72] and off-axis radio frequency (RF) magnetron sputtering [73]. Different types of instabilities compete in perovskite compounds. Usually, at the bulk level, only one type of distortion appears in the ground state as in  $PbTiO_3$ , which has a purely ferroelectric ground state, and in  $SrTiO_3$ , which has an anti-ferrodistorted ground state [74], although both ferroelectric and anti-ferroelectric instabilities coexist in the high symmetry phase of the two bulk materials [9, 75].

Large period  $PTO/STO$  superlattices exhibit a ferroelectric behavior, with a coupling between  $PTO$  layers and a domain structure dependent of the  $STO$  layer thickness [76]. In the limit of small  $STO$  thicknesses, a uniform polarization can develop through the whole superlattice. The amplitude of this polarization decreases with the  $PTO$  content and is expected to vanish below a critical  $PTO$  thickness. Surprisingly, an unexpected recovery of ferroelectricity was observed in ultra-short

period *PTO/STO* superlattices[20]. Bousquet et al. attributed this behavior to the emergence of a new type of ferroelectricity arising from an unusual trilinear coupling between the ferroelectric mode and two distinct antiferrodistortive motions. Consequently, the coupling of lattice modes in oxide superlattices has generated a lot of attention. The concept of “hybrid improper ferroelectricity” further discussed in the next Section was introduced [51] and rationalized [77]. Guiding rules have been proposed to identify alternative hybrid improper ferroelectrics [78]. The emergence of ferroelectricity in rotation-driven ferroelectrics was also widely discussed [79]. Still many questions remain regarding the finite temperature behavior of such systems like the structural phase transition sequence and the ferroelectric switching mechanism.

## 1.4 Different types of ferroelectricity

Ferroelectricity was discovered in 1920 by Valasek [80] who observed in Rochelle salts a spontaneous polarization which is switchable under an external electric field. This ferroelectric materials are a group of insulators characterized by a reversible spontaneous polarization in which the coupling between the electric field and polarization gives rise to an electric hysteresis loop as shown in Figure 1.6. With the time passing, various ferroelectric materials were used in technological applications. In the present thesis, we will mainly focus on the ferroelectric properties of perovskite compounds, in which ferroelectricity was first observed in *BaTiO<sub>3</sub>* in 1945 [7]. Ferroelectric materials usually undergo a structural phase transition from a non-polar centrosymmetric paraelectric phase to a polar noncentrosymmetric ferroelectric phase when decreasing the temperature. However, the phase transition mechanism is different for conventional proper ferroelectricity, improper ferroelectricity and hybrid improper ferroelectricity, as it will be briefly introduced in this section.

### 1.4.1 Proper ferroelectricity

In conventional proper ferroelectrics like *BaTiO<sub>3</sub>* and *PbTiO<sub>3</sub>*, the polarization is induced directly by the condensation of unstable polar mode which acts as the primary order parameter. In such systems, the evolution of the energy with the polarization around the paraelectric structure ( $P=0$ ) is characterized by a typical double-well shape (the blue curve in Figure 1.7). We can expand the internal energy around the paraelectric structure in terms of the order parameter  $P$  as:

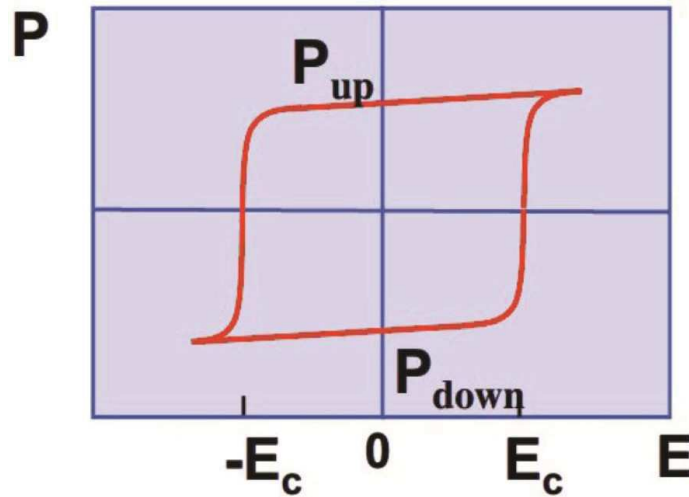


FIGURE 1.6: Hysteresis loop in ferroelectric materials.  $E$  refers to the external electric field and  $P$  refers to the polarization.  $P_{up}$  and  $P_{down}$  correspond to two equivalent spontaneous polarized states with opposite polarization directions.  $E_c$  is the depolarization field.

$$E = \frac{1}{2}A_0P^2 + \frac{1}{4}B_0P^4 \quad (1.5)$$

In proper ferroelectrics,  $A_0 < 0$ . This negative energy curvature is associated to the presence in the paraelectric phase of an unstable polar mode with an imaginary frequency ( $A_0 \propto \omega^2$ ) which appears at the first-principles level as the fingerprint of the proper ferroelectric behaviors.

## 1.4.2 Improper ferroelectric

Improper ferroelectricity is another distinct behavior which was first proposed in 1974 [81]. In this kind of materials, contrary to conventional proper ferroelectrics, the ferroelectric phase transition is not driven by an unstable polar phonon mode but by another non-polar mode, let's say  $\phi_1$ . The polarization  $P$  is no more the primary driving force for the ferroelectric phase transition but is the slave of another order parameter which couples with it through an energy term linear in  $P$ . As example, let us mention the spin-driven improper ferroelectric  $TbMnO_3$  [82–84] and the structural driven improper ferroelectric  $YMnO_3$  [85]. In  $TbMnO_3$ , there is a bi-linear coupling between the polarization and the magnetic primary order parameters so that the system is also referred to as a pseudo-proper ferroelectric [86, 87]. As discussed in [85], in  $YMnO_3$ , there is no unstable polar mode at the zone center. The phase transition

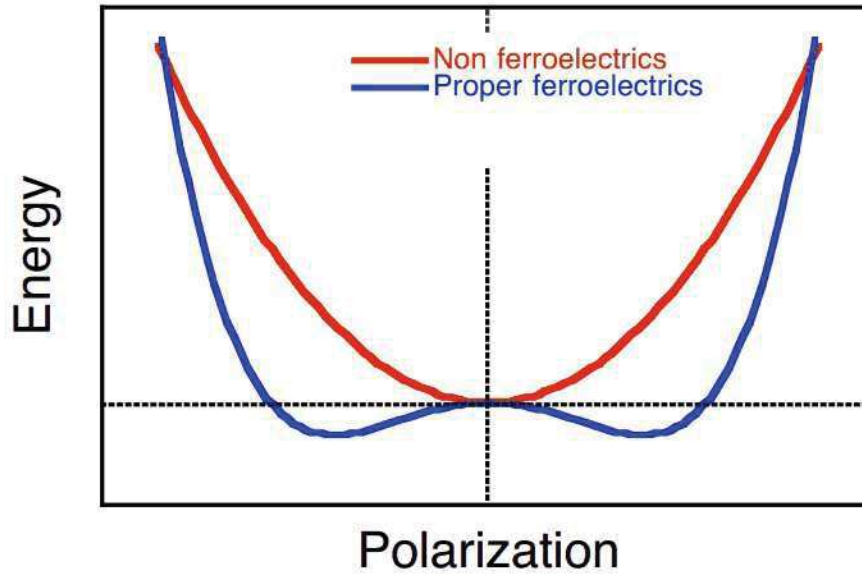


FIGURE 1.7: Energy curve in terms of  $P$ , for proper ferroelectric state (blue color) and non-ferroelectric state (red color).

is driven by an unstable non-polar ‘trimerization’ mode ( $K_3=\phi_1$ ), the condensation of which produce the appearance of  $P$  through a coupling term.

The expansion of the energy in terms of  $\phi_1$  and  $P$  in systems like  $YMnO_3$  takes the form:

$$E = \frac{1}{2}A_0P^2 + \frac{1}{4}B_0P^4 + \frac{1}{2}A_1\phi_1^2 + \frac{1}{4}B_1\phi_1^4 + C_{01}\phi_1^3P \quad (1.6)$$

$A_0$  is positive and  $A_1$  is negative since  $P$  is a stable mode while  $\phi_1$  is an unstable mode. The condensation of  $\phi_1$  will act as a geometric field that will shift the polarization well to lower energy through the coupling term  $C_{01}\phi_1^3P$  as illustrated in Figure 1.8. Contrary to proper ferroelectricity, the polarization well remains a single well with direct consequences on the ferroelectric properties. First, the switching of  $P$  requires the concomitant switching of  $\phi_1$  (see Figure 1.8) providing a unusual strong link between the two degrees of freedom. Second, in the absence of softening of a polar mode, there is no divergence of the dielectric constant and related dielectric properties at the phase transition. Finally, the system is less sensitive to depolarizing field issues and can preserve a finite spontaneous polarization, even in open-circuit electrical boundary conditions [77].

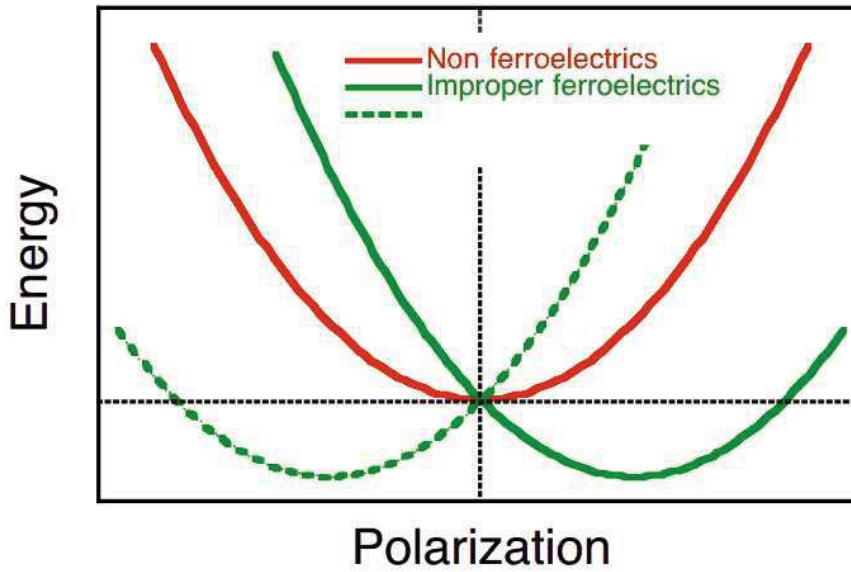


FIGURE 1.8: Energy curve in terms of  $P$  for non-ferroelectrics (red line) and improper ferroelectrics (green line, solid and dashed).

### 1.4.3 Hybrid improper ferroelectricity

Things are still slightly more complex for ‘hybrid improper ferroelectricity’ which was first proposed for  $PTO/STO(1/1)$  system in Ref [51]. The energy curve in terms of  $P$  is a shifted single-well as in improper ferroelectricity. However, as it is shown in the energy expansion 1.7, there are now two independent non-polar order parameters,  $\phi_1$  and  $\phi_2$ , linearly coupled with polar mode  $P$  through the trilinear coupling term  $\lambda\phi_1\phi_2P$ . Here,  $\phi_1$  and  $\phi_2$  work together as an hybrid mode to induce the polarization. To switch the polarization in this kind of systems requires switching either  $\phi_1$  or  $\phi_2$ . Besides, the condensation of two distortion modes will automatically condense the third one.

$$E = \frac{1}{2}A_0P^2 + \frac{1}{4}B_0P^4 + \frac{1}{2}A_1\phi_1^2 + \frac{1}{4}B_1\phi_1^4 + \frac{1}{2}A_2\phi_2^2 + \frac{1}{4}B_2\phi_2^4 + C_{01}\phi_1^2P^2 + C_{02}\phi_2^2P^2 + C_{12}\phi_1^2\phi_2^2 + \lambda\phi_1\phi_2P \quad (1.7)$$

The investigation of such hybrid improper ferroelectricity recently appeared as a field of increasing interest. Such ferroelectrics may display different phase transition behaviors from conventional improper ferroelectrics. Also the coupling with other properties like the magnetism offer a pathway to electric switching of the magnetization [51, 88].

## 1.5 Technical approaches

In the present thesis, our investigations will rely on the density functional theory, effective Hamiltonian methods and phenomenological Landau-Devonshire theory. The purpose of this section is to briefly introduce our technical approach; more details will be found in following chapters.

### 1.5.1 First-principles calculations

Density Functional Theory (DFT) is widely used for the calculation of electronic structure and properties of complex oxides [89]. In the case of  $ABO_3$  ferroelectric compounds, a large amount results from *DFT* calculations have been reported in recent years. Here, we just select some of them as examples not only in bulk systems like  $BaTiO_3$ ,  $PbTiO_3$ [90],  $KNbO_3$  [91], but also for superlattices such as  $PTO/STO$  [20],  $BTO/STO$  [62, 63].

As it is mentioned in Ref [89], the first-principles calculations can be very accurate at predicting structural parameters, which is an important complement to experimental structure determination. The phonon calculations based on first-principles proved an efficient way to explain the infrared and Raman spectroscopy data. Furthermore, phonon calculations in high-symmetry phases can be used to identify the lattice instabilities related to the atomic distortions in the low symmetry phase. We need to notice that, within DFT calculations, some approximation may cause errors. For instance, the local-density-approximation (LDA) calculations systematically underestimate the lattices volume to which the ferroelectric properties are sensitive. In this case we need to be very carefully in treating the DFT results for ferroelectricity. All first-principle calculations performed in this present thesis were done using the open source code package ABINIT [92]. There are many other available packages within DFT, Hartree-Fock or hybrid: VASP [93–96], SIESTA [97], CRYSTAL [98], WIEN2k [99], and PWscf[100]. The basics of DFT will be introduced in Chapter 2.

### 1.5.2 Effective Hamiltonian methods

In ferroelectric  $ABO_3$  compounds, the temperature evaluations of the structure and functional properties is a key issue. Unfortunately, DFT calculations are typically

restricted at zero Kelvin. First-principles molecular dynamics simulations are a priori possible but restricted in practice to very small systems and time scales. In this context, an effective Hamiltonian approach to structural phase transitions was proposed by Rabe and Joannopoulos [101, 102] in which the thermal average of the quantities of interest were calculated by a standard Metropolis Monte Carlo method, and the parameters of the Hamiltonian were determined from first-principles calculations. This effective Hamiltonian method was first applied to *GeTe* [101, 102] and then generalized to the perovskite *BaTiO<sub>3</sub>* [103, 104], opening the door to the investigation of temperature dependence of phase transitions in perovskite materials. However, the ‘Effective Hamiltonians’ are restricted to a small set of relevant ionic degrees of freedom, which is not sufficient for *PTO/STO(1/1)* where many phonon instabilities coexist in the reference high-symmetry phase. As a natural expansion, a new ‘model potential’ was suggested by Wojde et. al. [105] that properly includes all ionic degrees of freedom. This new method will be briefly introduced in Chapter 2 and applied to *PTO/STO(1/1)* superlattices in Chapter 3.

### 1.5.3 Phenomenological Landau-Devonshire Theory

At the macroscopic level, the most popular method to describe the temperature phase transition behavior is the phenomenological Landau-Devonshire theory [106]. Here, we will simply introduce the basic theory of this instead of listing a vast literature.

Based on Landau theory, the phase transition behavior is described in terms of order parameters which correspond to the symmetry breaking process. Below the Curie phase transition temperature  $T_C$ , the order parameter has a finite value which vanishes when temperature reaches  $T_C$ . In this framework, the free energy of the material is written as a Taylor expansion in terms of selected order parameters, as the polarization  $P$  in the case of ferroelectric phase transitions:

$$F(T, P) = AP^2 + BP^4 + CP^6 \quad (1.8)$$

This expansion is typically truncated at the sixth order,  $A$ ,  $B$ ,  $C$  being independent parameters.  $C$  is always positive to guarantee that the  $P$  which minimize  $F$  is finite.

According to the Landau theory, the sign of  $B$  determines the order of the phase transition. Cases where  $B > 0$  corresponds to second order transition.  $A$  should be

positive when  $T > T_C$  since the minimum should be found at  $P=0$  and be negative when  $T < T_C$ . The simplest choice is:

$$A = a(T - T_C) \quad (1.9)$$

with  $a > 0$ . We notice that  $A \propto \omega^2$  where  $\omega$  is the frequency of the polar mode condensing at the phase transition. So that this temperature dependence of  $A$  is a perfect agreement with the soft mode theory of Cochran that postulates  $\omega^2 = \omega_0^2(T - T_C)$  and so well suited to describe ferroelectricity. With such parameters, when  $T > T_C$ , the energy curve has a single well with the minimum value at  $P=0$ . For  $T < T_C$ , the energy curve will be a double well in which the minimum points are found at  $P = \pm P_0$  where  $P_0 = \sqrt{\frac{a(T_C - T)}{2B}}$ . Similar analysis can be used for first order phase transitions by fixing  $B$  to a negative value [7, 107]. In this case the phase transition takes place at  $T_0 > T_C$  and the polarization switches discontinuously from zero to a finite value at the transition point.

## 1.6 Motivation

As it is introduced above, the first-principles methods based on DFT efficiently work but is restricted to zero Kelvin systems. Effective Hamiltonian methods, based on parameters issued from DFT, can describe the temperature dependence of phase transitions but mainly for bulk ferroelectric materials (*BaTiO<sub>3</sub>* [103, 104], *SrTiO<sub>3</sub>*, *PbTiO<sub>3</sub>* [108]). Specifically, for the short period *PTO/STO(1/1)* superlattice, it is observed that different modes of atomic distortions are coupled. However, it is difficult to identify from DFT calculations which one is the primary order that drive the phase transition. In this case, elaborating a model for superlattices beyond the bulk level becomes meaningful.

The first motivation for the present thesis is to investigate the possibility of building an effective model for perovskite superlattices. Based on the effective Hamiltonian approach, we aim at building an effective model for short periodic *PTO/STO(1/1)* superlattice, that can describe the temperature dependence for each mode of atomic distortion. DFT calculations will be performed as the first step and will provide the parameters in effective Hamiltonian, which will be developed to include all the relevant phonon modes. The detail of this approach will be introduced in Chapter 3.

Furthermore, to go beyond the short periodic system, we need to extend our model to thick superlattices, this is our second motivation. Directly calculating the phonon behavior of large periodic systems from first-principles become rapidly untraceable. In this case we wish to develop another model method based on accurate calculations on simple materials, e.g bulk, short periodic superlattices. This will be presented in Chapter 4.

# Chapter 2

## Theoretical approach

### 2.1 Introduction

Many properties of materials can nowadays be determined from first-principles, providing key new insights into critical problems in physics, chemistry and material sciences. In this chapter, we will give a brief overview of first-principles methods we used in our research. We will describe the general framework, equations and the main approximation we used without mathematical details.

Density Functional Theory (DFT), which is based on quantum mechanics, has become one of the most widely used first-principles approach. In this chapter, we will first introduce the *Schrödinger* equation for many-body systems and the widely used Born-Oppenheimer approximation. Then, we will describe the framework and the basic equations of DFT and briefly introduce Density Functional Perturbation Theory (DFPT). In the next section, the main approximations used in DFT calculations will be presented including different exchange-correlation approximations, the plane wave expansions, the k-grid for Brillouin zones and the so-called pseudopotentials. At last, a finite temperature theory so-called ‘effective model potential’ will be introduced.

### 2.2 Many-body Hamiltonian

In quantum mechanics, the physics of a stationary system is described by the time-independent *Schrödinger* equation:

$$H\psi = E\psi \quad (2.1)$$

where  $\psi$  is the wave function of the many-body system,  $\mathbf{H}$  is the Hamiltonian operator and  $E$  is the corresponding energy. The Hamiltonian for a many-body system with the interaction of electrons and nuclei can be written as:

$$H(\vec{R}, \vec{r}) = T_N(\vec{R}) + T_e(\vec{r}) + V_{NN}(\vec{R}) + V_{ee}(\vec{r}) + V_{eN}(\vec{R}, \vec{r}) \quad (2.2)$$

where  $\vec{R}$  refers to all the nuclear coordinates  $\vec{R}_I$  and  $\vec{r}$  refers to all the electronic coordinates  $\vec{r}_i$ .  $T_N$  and  $T_e$  are the kinetic energy operator of nuclei and electrons,  $V_{NN}$ ,  $V_{ee}$  and  $V_{eN}$  are the electrostatic potential energy operator between nuclei, electrons and electrons and nuclei:

$$T_N = -\frac{\hbar^2}{2} \sum_I \frac{1}{M_I} \frac{\partial^2}{\partial \vec{R}_I^2} \quad (2.3)$$

$$T_e = -\frac{\hbar^2}{2m} \sum_i \frac{\partial^2}{\partial \vec{r}_i^2} \quad (2.4)$$

$$V_{NN} = \frac{e^2}{2} \sum_{I \neq J} \frac{Z_I Z_J}{|\vec{R}_I - \vec{R}_J|} \quad (2.5)$$

$$V_{ee} = \frac{e^2}{2} \sum_{i \neq j} \frac{1}{|\vec{r}_i - \vec{r}_j|} \quad (2.6)$$

$$V_{eN} = e^2 \sum_{iJ} \frac{Z_J}{|\vec{r}_i - \vec{R}_J|} \quad (2.7)$$

$Z_I$  is the charge of nuclei  $I$  with mass  $M_I$ ,  $m$  is the mass of electron and  $-e$  is the elementary charge.

The Born-Oppenheimer approximation arises from the fact that the mass of nuclei is much larger than electron's, so that the kinetic energy of the nuclei can be neglected and the wave function of the electron system can be treated separately, considering nuclei positions  $\vec{R}_I$  as parameters :

$$H(\vec{R}, \vec{r}) = T_e(\vec{r}) + V_{NN}(\vec{R}) + V_{ee}(\vec{r}) + V_{eN}(\vec{R}, \vec{r}) \quad (2.8)$$

This basic simplification reduces the many-body problem to the study of interacting electrons in some potential background of the nuclei. However, the problem remains complex due to the electron-electron interactions. Besides, there are about  $10^{23}$  electrons in the material so that it remains, in practice, impossible to solve the *Schrödinger* equations and further simplifications are required, in order to retrieve a set of single particle wave functions, and, for example, to take advantage of the translation symmetry in crystals.

## 2.3 Density Functional Theory

DFT was first proposed in 1960's by Hohenberg and Kohn [109] and Kohn and Sham [110]. The first paper showed that the physical properties of the ground state for a many-body electron system can be considered as a unique functional of the electronic density  $n(\vec{r})$ . It provides the possibility to avoid seeking directly for the complex many-body wave function, considering different point of view in which the electronic density is a simpler scalar function of position. But in this paper, the authors did not introduce any explicit form for this functional.

In the second paper, Kohn and Sham provided an *ansatz* formulation of the density functional theory in which the interacting electronic system is replaced by a non-interacting particle system with exactly the same ground-state electronic density, by introducing a external potential. In this framework, the electronic density( $n(\vec{r})$ ) can be obtained by single particle wave functions and the potential can be efficiently approximated as discussed below.

### 2.3.1 Kohn-Sham equations

In the single particle type Kohn-Sham framework, the total energy is given by:

$$E_{KS} = -\frac{1}{2} \sum_i \langle \psi_i | \nabla^2 | \psi_i \rangle + \frac{1}{2} \int \frac{n(\vec{r})n(\vec{r}')}{|\vec{r} - \vec{r}'|} d\vec{r}d\vec{r}' + E_{xc} [n(\vec{r})] + \int V_{ext}(\vec{r})n(\vec{r})d\vec{r} + E_{NN} \quad (2.9)$$

where the first term corresponds to the electronic kinetic energy of the non-interacting particles, the second one is the classical Coulomb energy (Hartree energy) related to the electronic density  $n(\vec{r})$ . The third term relates the exchange and correlation energy between electrons. The fourth one corresponds to the interaction between electrons and the external electron-ion potential  $V_{ext}$ . The last one is the potential energy between nuclei. All these terms are defined explicitly except the exchange and correlation energy  $E_{xc}[n(\vec{r})]$ . The electronic density is given by:

$$n(\vec{r}) = \sum_i^{occ} \psi_i^*(\vec{r})\psi_i(\vec{r}) \quad (2.10)$$

For a given set of atomic positions, the ground-state can be obtained by minimizing Eq. 2.9 under the following orthonormalization constraints:

$$\langle \psi_i | \psi_j \rangle = \delta_{ij} \quad (2.11)$$

By using the Lagrange multiplier method, the minimization of Eq. 2.9 with the constraints can be achieved by minimizing the following equation:

$$F[\psi_i] = E[\psi_i] - \sum_{i,j}^{occ} \Lambda_{ij} (\langle \psi_i | \psi_j \rangle - \delta_{ij}) \quad (2.12)$$

In which  $\Lambda_{ij}$  are the Lagrange multipliers. The corresponding Euler-Lagrange equation is:

$$H |\psi_i\rangle = \sum_j \Lambda_{ij} |\psi_j\rangle \quad (2.13)$$

where the Hamiltonian is

$$H = -\frac{1}{2}\nabla^2 + v_{ext} + v_H + v_{xc} \quad (2.14)$$

The Hartree and exchange-correlation potentials are respectively defined as the functional derivative of the Hartree and exchange-correlation energy with respect to the density:

$$v_H = \frac{\delta E_H[n]}{\delta n(\vec{r})} \quad (2.15)$$

and

$$v_{xc} = \frac{\delta E_{xc}[n]}{\delta n(\vec{r})} \quad (2.16)$$

The solution of Eq. 2.13 is not unique since we can always apply a unitary transformation  $U$  to the wave functions of the occupied states:

$$|\psi_i\rangle \rightarrow \sum_j^{occ} U_{ij} |\psi_j\rangle \quad (2.17)$$

by keeping the same energy nor the density which is so-called *gauge transformation*. Since the Hamiltonian is a hermitian operator, we can always work within the so-called *diagonal gauge* where the Lagrange multiplier matrix is diagonal

$$\Lambda_{ij} = \langle \psi_j | H | \psi_i \rangle = \varepsilon \delta_{ij} \quad (2.18)$$

In practice, alternatively to solving Eq. 2.9, the ground state of the system can also be determined by solving self-consistently the following set of Kohn-Sham equations by a self-consistent procedure (as it is done in ABINIT).

$$\left\{ \begin{array}{l} [-\frac{1}{2}\nabla^2 + v_s] |\psi_i\rangle = \varepsilon_i |\psi_i\rangle \\ v_s(\vec{r}) = v_{ext}(\vec{r}) + \int \frac{n(\vec{r}_1)}{|\vec{r}_1 - \vec{r}|} d\vec{r}_1 + \frac{\delta E_{xc}[n]}{\delta n(\vec{r})} \\ n(\vec{r}) = \sum_i^{occ} \psi_i^*(\vec{r}) \psi_i(\vec{r}) \end{array} \right. \quad (2.19)$$

The starting point of this procedure is a given set of atomic positions and a guess for the electronic density  $n(\vec{r})$ . After solving Eq. 2.19, the obtained new density  $n'(\vec{r})$  is used to compute  $v_s(\vec{r})$  and  $E_{xc}$ . This procedure is repeated until self-consistency is achieved.

### 2.3.2 Density Functional Perturbation Theory

Numerous physical properties (mechanical, dielectric, dynamical,...) depend on the derivative of the total energy with respect to perturbations i.e. strain, external electric field, atomic displacements... This can be calculated by freezing the system into finite values of the perturbation, and extracting derivatives from a finite difference technique (so-called frozen-phonon approach). It is also possible to access these by merging the DFT and perturbation theory in a systematic way. Density Functional Perturbation Theory (DFPT) was first reported by Baroni, Giannozzi and Testa [111–114]. A different way to calculate the energy-derivatives was proposed by X. Gonze, Allan and Teter [115–119], based on a variational principle rather than solving the Sternheimer equation. It gives access also to non-linear responses thanks to the  $(2n+1)$  theorem [115].

Let us consider a small external perturbation labeled by the parameter  $\lambda$ , which can refer to the atomic displacements  $\mathbf{R}$ , homogeneous strain  $\eta$  or homogeneous electric field  $\xi$ . Then the energy  $E[\lambda]$  can be expanded around the ground-state ( $\lambda=0$ ) according to:

$$E[\lambda] = E(0) + \sum_i \left. \frac{\partial E}{\partial \lambda_i} \right|_0 \lambda_i + \frac{1}{2} \sum_{i,j} \left. \frac{\partial^2 E}{\partial \lambda_i \partial \lambda_j} \right|_0 \lambda_i \lambda_j + \dots \quad (2.20)$$

If we truncate this expansion to the second order, the related physical quantities are reported in Table 2.1. The first order derivatives with respect to atomic displacement are related to the atomic forces ( $\mathbf{F}$ ), the first order derivatives with respect to strain can provide the stress tensor ( $\sigma$ ) and the spontaneous polarization ( $\mathbf{P}$ ) can be obtained from the first order derivatives with respect to electric field. The interatomic force constants ( $C$ ), the optical dielectric tensor ( $\epsilon^\infty$ ), the elastic constant ( $c^0$ ), the Born effective charges tensor ( $Z^*$ ), the piezoelectric tensor ( $e^0$ ) and the internal strain coupling parameters ( $\gamma$ ) can be accessed from the second order derivatives of the total energy. In this framework, additional physical quantities can be obtained as well, i.e. the phonon dispersion curves, the piezoelectric and elastic tensors, the LO-TO splitting, *etc.*

TABLE 2.1: Physical quantities obtained from the first and the second order derivatives of the total energy with respect to atomic positions  $\mathbf{R}$ , homogeneous strains  $\eta$  and electric field  $\xi$ .

$\lambda$	$\eta$ and electric field $\xi$ .	
	1 <sup>st</sup> order	2 <sup>nd</sup> order
		$\mathbf{R}$ $\eta$ $\xi$
$\mathbf{R}$	$\mathbf{F}$	$C$ $\gamma$ $Z^*$
$\eta$	$\sigma$	$\gamma$ $c^0$ $e^0$
$\xi$	$\mathbf{P}$	$Z^*$ $e^0$ $\epsilon^\infty$

## 2.4 Practical implementation

In principle, DFT provides us the possibility to access different physical quantities from first-principles in an accurate way. However, we have to introduce several approximations to our practical calculation in order to achieve the balance between the accuracy and the computation cost [120]. In this section, we will introduce the basic approximations in practical DFT calculations including the exchange-correlation functional, the plane wave expansion and related truncation, the grid of the Brillouin zone and the pseudopotentials.

### 2.4.1 Exchange-correlation energy

In the Kohn-Sham approach, the interacting many-body system is replaced by a non-interacting type description in which fictitious independent particles move in an effective potential produced by the ions and all the other particles. In practice, only the form of exchange-correlation energy  $E_{xc}[n]$  is unknown and must be approximated. It is worth to point out that the exchange-correlation energy is expected to be a universal functional of the whole electronic density. However, some methods of approximation consider local development of the density and provide accurate results.

#### 2.4.1.1 Local Density Approximation

The first proposed and simplest approximation is the Local Density Approximation (LDA) [110] in which it is assumed that the exchange-correlation energy of each particle at point  $\vec{r}$ ,  $\epsilon_{xc}(\vec{r})$ , only depends on the density at this point. In this case, exchange-correlation energy is equivalent to the one for an homogeneous electron gas with the same density:

$$E_{xc}^{LDA} [n] = \int \varepsilon_{xc}^{\text{hom}} [n(\vec{r})] n(\vec{r}) d\vec{r} \quad (2.21)$$

The exchange part can be obtained analytically according to:

$$\varepsilon_x^{\text{hom}} [n] = -\frac{3}{4\pi} (3\pi^2 n)^{1/3} \quad (2.22)$$

The correlation part  $\varepsilon_c^{\text{hom}}$  was accessed by Monte-Carlo simulation of the homogeneous electron gas. There are various formulations (Wigner, X-alpha, Gunnarson-Lundqvist, Perdew-Zunger, Perdew-Wang, Teter...) that are referred to as local density approximations. They have the same exchange part but slightly different correlation parts.

Such a simple approximation works well in many cases with surprising accuracy [121], which make it become the most widely used on in solid state simulations. Typical error of LDA respect with experimental values is about 1% on atomic positions and lattice constants and about 5% on phonon frequencies. Well known exceptions are on the electronic band gap which is systematically largely underestimated. The 1% error on the lattice constants can have dramatic consequences in perovskite oxides, in which the ferroelectric instability is very sensitive to strain.

### 2.4.1.2 Generalized Gradient Approximation

An alternative and connected approach is labelled as Generalized Gradient Approximation (GGA) [122–125]. Here the exchange-correlation functional depends not only on the local density at  $\vec{r}$ , but also on its gradient or higher order derivatives. It is expanded as follows:

$$E_{xc}^{GGA} [n] = \int n(\vec{r}) \varepsilon_{xc}^{GGA} [n(\vec{r}); |\nabla n(\vec{r})|; \nabla^2 n(\vec{r})] d\vec{r} \quad (2.23)$$

This GGA approach can improve the computed value of the cohesive energy and consequently can better predict the bond-length and lattices constant. However, this kind of approximation does not work well for dielectric constants since this quasi-local approximation does not include any long-range interaction [126–128].

Besides, there are several alternative available approximations such as the weighted density approximation (WDA) [129], and so-called hybrid functionals were also developed to improve greatly the accuracy but at significantly larger computational cost.

### 2.4.2 Plane-wave basis set

In an infinite periodic solid, by imposing well known Born-Von Karman periodic boundary conditions, the wave function can be written in the Bloch form as the product of a plane wave by a cell function:

$$\psi_{n,\vec{k}}(\vec{r}) = \frac{1}{\sqrt{\Omega}} u_n(\vec{k}, \vec{r}) e^{i\vec{k}\cdot\vec{r}} \quad (2.24)$$

where  $\Omega$  is the cell volume,  $\vec{k}$  is the wave-vector in the reciprocal space and  $n$  is the band index. In practical calculations, Bloch functions are expanded in a Fourier expansion:

$$\psi_{n,\vec{k}}(\vec{r}) = \frac{1}{\sqrt{\Omega}} \sum_{\vec{G}} C_{n,k}(\vec{G}) e^{i(\vec{k}+\vec{G})\cdot\vec{r}} \quad (2.25)$$

This Fourier transformation of the Bloch functions involves infinite number of plane-wave terms. In practice, a cut-off energy  $E_{cut}$  has to be chosen to truncate this expansion as:

$$\frac{\hbar^2}{2m} |\vec{k} + \vec{G}|^2 \leq E_{cut} \quad (2.26)$$

This kind of truncation will introduce an error that can be controlled by increasing the value of  $E_{cut}$ , a convergence procedure is needed in practical calculations.

### 2.4.3 Brillouin zone grid

The electronic density is obtained from an integration procedure of the square modulus of previously mentioned Bloch type wave functions over the Brillouin zone in reciprocal space, which is be done over a group of selected  $\vec{k}$  points. In this case, a

finite number selection of  $\vec{k}$  point is needed so that the integration procedure can be replaced by a sum over limited number of  $\vec{k}$  points. In this thesis, we will use the techniques developed by Monkhorst and Pack [130]. The related physical quantities obtained from DFT are strongly depends on the set of  $\vec{k}$  points especially for metals. For a perovskite oxide such as  $SrTiO_3$  we used a  $6 \times 6 \times 6$  k-grid. For some conductors, larger density of k-grid is required to precisely define the Fermi surface.

This kind of error induced by the k-grid of Brillouin zone is a numerical error, the amplitude of which can be decreased by improving the density of  $\vec{k}$  points in Brillouin zone.

#### 2.4.4 Pseudopotentials

The plane wave basis set has some difficulties in describing the core electrons and the valence electrons in the core region, since a large number of plane wave are required, which increases the cost of the practical calculation. To solve this problem, the pseudopotential technique [131] was developed by introducing the following approximations: i) the electronic properties in solid state mainly depend on the valence electrons while the core electrons can be isolated and treated equivalently with the ones in an independent atom. ii) The strong oscillations of the valence electron state inside the core region can be replaced by a smooth function while keeping the same behavior out-side the core region.

The first approximation is so-called frozen-core approximation: the core electrons are not involved in the chemical bonding directly which will be slightly modified by the changed atomic environment. In this situation, it is reasonable to expect that the core electrons can be treated as the ones in a isolated atom.

In the second approximation, the ionic potential screened by the core electrons is replaced by a fictitious potential such that the valence wave functions remain unchanged beyond a given cut-off radius, with a smoothly varying function inside the core region. In practice, a reference calculation will be performed on a isolated atom, and then an analytical pseudopotential is fitted to reproduce the previous calculation.

The pseudopotential approximation significantly decreases the number of plane waves involved in the Bloch wave expansion and the number of electrons to be considered in the Kohn-Sham equations, therefore the practical calculation can be much less time consuming at practically low cost for accuracy. It is needed to mentioned that

various types of pseudopotential approximations are available [132]. In our work, we used Teter pseudopotentials [133] in all LDA calculations and optimized (RRKJ) pseudopotentials in our GGA-WC calculations [125].

## 2.5 Effective model potential

As mentioned in Chapter 1, “Effective Hamiltonians” were developed to investigate the finite temperature behavior of materials [101–104], but only a small set of phonon modes are selected as the basis, which can not well describe the system such as *PTO/STO(1/1)*. In order to solve such problems, a new effective model potential was developed recently [105] which will be summarized in this part.

The “model potential” has the same general form as “Effective Hamiltonians”: the model energy is spread into different terms, written as a low-order Taylor expansion in terms of atomic and strains degrees of freedom:

$$E_{eff}(\{\mathbf{u}_i\}, \eta) = E_p(\{\mathbf{u}_i\}) + E_s(\eta) + E_{sp}(\{\mathbf{u}_i\}, \eta) \quad (2.27)$$

Here we use the subscript ‘eff’ to distinguish between the energy from our potential and the energy obtained from our first-principles calculations;  $\mathbf{u}_i$  refers to the atomic position of atom  $i$  and  $\eta$  refers to the strain applied on the lattice. At the right side of (2.27), the first term is the energy change due to atomic displacements (here  $p$  refers to the phonon), the second term is the energy change from the strain only and the third term refers to the contribution from strain-phonon coupling. Each term will be discussed below:

### 2.5.1 $E_p(\{\mathbf{u}_i\})$

Usually, the  $E_p(\{\mathbf{u}_i\})$  term can be splitted into two parts, the harmonic part ( $E_{har}(\{\mathbf{u}_i\})$ ) and the anharmonic part ( $E_{anh}(\{\mathbf{u}_i\})$ ). Here the phonon term is written as a Taylor series around the reference structure (RS) as:

$$E_p(\{\mathbf{u}_i\}) = \frac{1}{2} \sum_{i\alpha j\beta} K_{i\alpha j\beta}^{(2)} u_{i\alpha} u_{j\beta} + \frac{1}{6} \sum_{i\alpha j\beta k\gamma} K_{i\alpha j\beta k\gamma}^{(3)} u_{i\alpha} u_{j\beta} u_{k\gamma} + O(\mathbf{u}^4) \quad (2.28)$$

The tensor  $K^{(n)}$  is formed as:

$$K_{i\alpha j\beta}^{(n)} = \left. \frac{\partial^n E_{eff}}{\partial u_{i\alpha} \partial u_{j\beta} \dots} \right|_{RS} \quad (2.29)$$

The  $RS$  structure is a stationary point of energy surface so that  $K^{(1)}=0$ . Besides it is needed to point out that this phonon term can be equivalently expanded as a function of displacement differences as:

$$E_p(\{\mathbf{u}_i\}) = \frac{1}{2} \sum_{\substack{ijkh \\ \alpha\beta}} \tilde{K}_{ijkh\alpha\beta}^{(2)} (u_{i\alpha} - u_{j\alpha})(u_{k\beta} - u_{h\beta}) + \frac{1}{6} \sum_{\substack{ijkhrt \\ \alpha\beta\gamma}} \tilde{K}_{ijkhrt\alpha\beta\gamma}^{(3)} (u_{i\alpha} - u_{j\alpha})(u_{k\beta} - u_{h\beta})(u_{r\gamma} - u_{t\gamma}) + O(\mathbf{u}^4) \quad (2.30)$$

It is obvious that  $E_p$  does not change for a rigid displacement of the material which make  $E_p$  to achieve the *Acoustic sum rule*(ASR) automatically. The harmonic part ( $K^{(2)}$ ), the force-constant matrix, can be obtained directly from our *DFT* calculations, which includes all phonon branches. Anharmonic terms ( $K^{(n)}$ ,  $n>2$ ), are determined by a fitting procedure aimed at obtaining a model that reproduces a training set of first-principle results.

### 2.5.2 $E_s(\eta)$ and $E_{sp}(\{\mathbf{u}_i\}, \eta)$

For the elastic energy  $E_s(\eta)$ , we use a Taylor expansion as:

$$E_s(\eta) = \frac{N}{2} \sum_{ab} C_{ab}^{(2)} \eta_a \eta_b + \frac{N}{6} \sum_{abc} C_{abc}^{(3)} \eta_a \eta_b \eta_c + O(\eta^4) \quad (2.31)$$

where

$$C_{ab\dots}^{(m)} = \frac{1}{N} \left. \frac{\partial^m E_{eff}}{\partial \eta_a \partial \eta_b \dots} \right|_{RS} \quad (2.32)$$

and  $N$  is the number of cells in the crystal. The harmonic term  $C^{(2)}$  in this series corresponds to the elastic constants which can be obtained directly from our first-principles calculations. The anharmonic terms ( $C^{(m)}$ ,  $m > 2$ ) are suppressed since they are not required for semi-quantitative results.

For the strain-phonon interaction term, we can write:

$$\begin{aligned} E_{sp}(\{\mathbf{u}_i\}, \eta) = & \frac{1}{2} \sum_a \sum_{i\alpha} \Lambda_{ai\alpha}^{(1,1)} \eta_a u_{i\alpha} + \frac{1}{6} \sum_a \sum_{i\alpha j\beta} \Lambda_{ai\alpha j\beta}^{(1,2)} \eta_a u_{i\alpha} u_{j\beta} \\ & + \frac{1}{6} \sum_{ab} \sum_{i\alpha} \Lambda_{abi\alpha}^{(2,1)} \eta_a \eta_b u_{i\alpha} + O(\eta^4) \end{aligned} \quad (2.33)$$

The  $\Lambda^{(1,1)}$  term describes the forces that act on the atoms as a consequence of homogeneous strain. As in the case of  $E_p$ , an alternative expression of  $E_{sp}$  can be used as:

$$\begin{aligned} E_{sp}(\{\mathbf{u}_i\}, \eta) = & \frac{1}{2} \sum_a \sum_{ij\alpha} \tilde{\Lambda}_{aij\alpha}^{(1,1)} \eta_a (u_{i\alpha} - u_{j\alpha}) + \frac{1}{6} \sum_a \sum_{ijhk\alpha\beta} \tilde{\Lambda}_{ijhk\alpha\beta}^{(1,2)} \eta_a (u_{i\alpha} - u_{j\alpha})(u_{k\beta} - u_{h\beta}) + \\ & \frac{1}{6} \sum_{ab} \sum_{ij\alpha} \tilde{\Lambda}_{abij\alpha}^{(2,1)} \eta_a \eta_b (u_{i\alpha} - u_{j\alpha}) + O(\eta^4) \end{aligned} \quad (2.34)$$

where  $\tilde{\Lambda}^{(m,n)}$  parameters achieve the ASR automatically. The leading harmonic term  $\tilde{\Lambda}^{(1,1)}$  is directly calculated from first-principles. For the anharmonic term we will use the following method: one runs DFPT calculations for the RS structure subject to a small strain  $\delta\eta$ , so that the force-constant matrix can be written in our model as:

$$K_{i\alpha j\beta}^{(2)} \Big|_{\delta\eta} = K_{i\alpha j\beta}^{(2)} + \sum_a \Lambda_{i\alpha j\beta}^{(1,2)} \delta\eta_a \quad (2.35)$$

which will allow us to obtain the targeted couplings.

### 2.5.3 Approximation and simulation details

As mentioned above, the harmonic term can be obtained from first-principles. The parameters of higher-order coupling, ie.  $\tilde{K}^{(n)}$  ( $n>2$ ) and  $\tilde{\Lambda}^{(m,n)}$  ( $m+n>2$ ), are obtained from a fitting procedure to reproduce a training set of first-principles results. In the *PTO/STO(1/1)* case, the training set was composed of low-energy phases that are more stable than RS. The fitting procedure has been discussed in Ref. [105].

It is worth noticing also that, When working with insulators, it is convenient to split the energy term into short-range and long-range parts as:

$$K^{(n)} = K^{(n)sr} + K^{(n)lr} \quad (2.36)$$

$$\Lambda^{(m,n)} = \Lambda^{(m,n)sr} + \Lambda^{(m,n)lr} \quad (2.37)$$

Where the long-range part corresponds to the Coulomb interaction which has a well known analytic form in terms of the Born effective charges ( $Z^*$ ) and the optical dielectric constants ( $\epsilon^\infty$ ) in the limit of long distances. For  $K^{(2)}$ , the long-range part is directly provided from first-principles codes as ABINIT. In order to obtain models for fast simulation, we do not include the long-range part for anharmonic terms, by simply assuming that  $\tilde{K}^{(n)lr} = \tilde{\Lambda}^{(m,n)lr} = 0$  and fitting the harmonic terms  $\tilde{K}^{(n)sr}$  and  $\tilde{\Lambda}^{(m,n)sr}$  to reproduce the training set from first-principles results.

# Chapter 3

## *PbTiO<sub>3</sub>/SrTiO<sub>3</sub>(1/1)* superlattices

### 3.1 Introduction

The coupling between different lattice modes in  $ABO_3$  series superlattices opens a feasible path toward the engineering of new multifunctional materials [134–136].  $(PbTiO_3)_m/(SrTiO_3)_n$  ( $PTO/STO(m/n)$ ) superlattices is one of the most studied system in recent literature, and is considered as a good example where the balance between different phonon instabilities can yield unusual phenomena that were theoretically predicted and experimentally observed [73, 137].

In short-period  $PTO/STO(1/1)$  superlattices, an unexpected recovery of ferroelectricity appears, as reported in Ref.[20], which is not a purely ferroelectric state, but rather a coupling between the polarization( $FE_z$ ) and two antiferrodistorted ( $AFD$ ) modes, corresponding to in-phase ( $\phi_{zi}$ ) and out-of phase ( $\phi_{zo}$ ) rotations of the oxygen octahedra along the polarization direction (shown in figure 3.2). This involves a trilinear coupling term between  $FE_z$ ,  $\phi_{zi}$  and  $\phi_{zo}$  which is the “fingerprint” of a so-called “hybrid improper ferroelectricity” behavior.

“Improper ferroelectricity” is a well known although rare phenomenon. In so-called “proper ferroelectrics”, the polarization is the primary order parameter of the phase transition while in “improper ferroelectrics” the polarization is the slave of another non-polar primary order parameter, responsible for the phase transition and inducing the polarization through an energy term linear in  $P$  [81]. Example of that type are the spin-driven improper ferroelectricity in  $TbMnO_3$  [82] and the structurally driven improper ferroelectricity in  $YMnO_3$  [85]. Things are still more complex in

$PTO/STO(1/1)$  superlattices, where the polarization couples with two distinct rotational modes. The combined two rotational modes, which have different symmetries, are treated like an hybrid mode coupling to a linear power of polarization. As it is discussed in Refs.[51] and [77] by analogy with usual improper ferroelectrics, people suggested to call such a system as *hybrid* improper ferroelectric.

Since then, the coupling of lattice modes in perovskite layered structures has generated an increasing interest, appearing also in magnetic superlattices as a promising pathway to achieve electric control of the magnetization[138]. The concept of “hybrid improper ferroelectricity” has been rationalized [77], guiding rules to identify alternative hybrid improper ferroelectrics have been proposed [139], and the emergence of ferroelectricity in rotation-driven ferroelectrics was discussed [79]. Still many fundamental questions remain regarding the behavior of hybrid improper ferroelectrics. For instance, the mechanism of their structural phase transition is not clearly established : does the primary and secondary distortions really condense at the same temperature or do we have instead consecutive phase transitions ? Also, the switching of the polarization mandatorily requires the concomitant switching of one of the rotational modes and the switching path is difficult to anticipate. Up to now, calculations were restricted to first-principles calculations at zero Kelvin. To go further and investigate these issues, a finite temperature theory is needed.

In the 90’s, an “Effective Hamiltonian” method was developed to access the finite temperature properties of perovskite oxides [101–104], in which the energy of high-symmetry reference structure is written as a low order Taylor expansion in terms of the most relevant phonon modes and strains. The coefficients are directly determined from *ab initio* calculations and the finite temperature properties are accessed from Monte Carlo simulations. This Effective Hamiltonian has achieved good results for many oxide materials. However, in our  $PTO/STO$  system, it is difficult to identify a small subset of phonon modes defining the relevant degrees of freedom. Thus we need to go further and build a new model potentials including all the atomic degrees of freedom as recently proposed in Ref.[105].

In this chapter, we will describe the basic dynamics of high-symmetry  $PTO/STO$  systems by using first-principles calculations and we will introduce a simple model by using Laudau type energy expansion. Then we will apply the new model potential to our system to investigate the finite temperature behavior and discuss the results.

## 3.2 Technical Details of DFT Calculations

All first-principles calculations were done with the ABINIT package within Density Functional Theory (DFT) and the local-density approximation (*LDA*) for the exchange-correlation energy. Teter's pseudopotentials were employed, with the following electrons treated as valence states: the  $5d$ ,  $6s$  and the  $6p$  states of  $Pb$ , the  $4s$ ,  $4p$  and  $5s$  states of  $Sr$ , the  $3s$ ,  $3p$ ,  $3d$  and  $4s$  states of  $Ti$  and the  $2s$  and  $2p$  states of  $O$ . Electronic wave functions were expanded in a plane-wave basis and an energy cutoff of 45 hartrees was used.

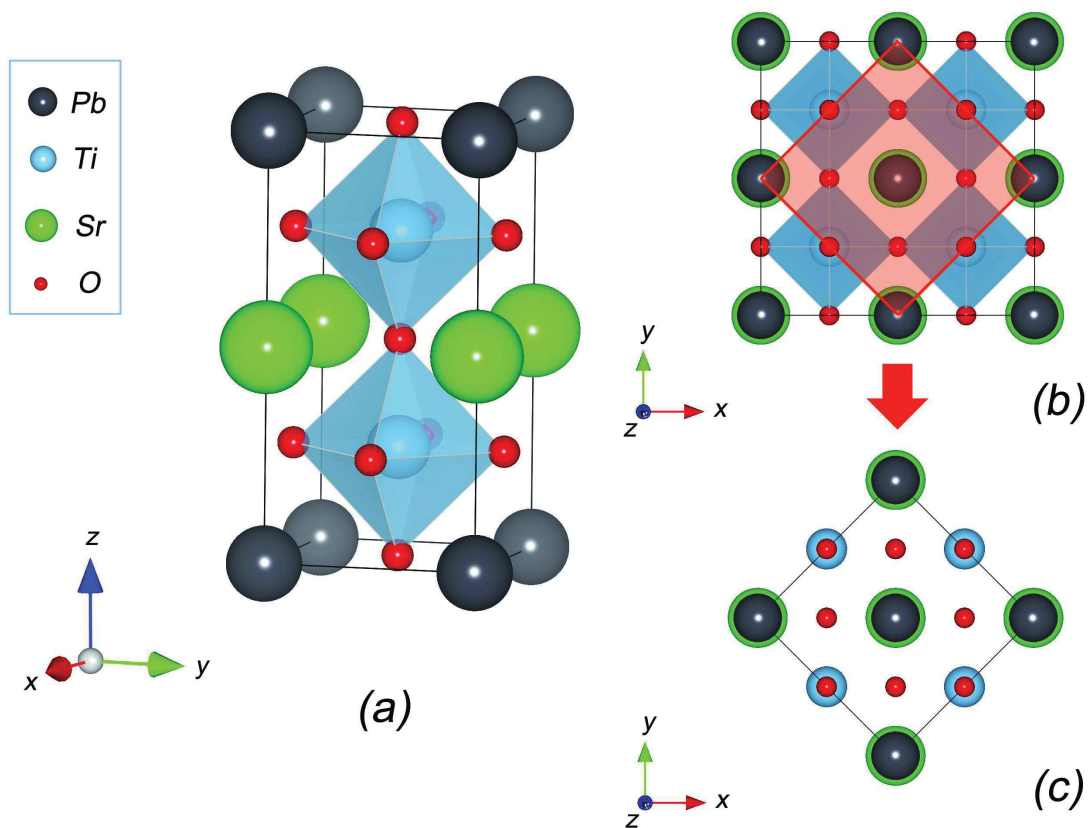


FIGURE 3.1: Structure of the  $PTO/STO(1/1)$  superlattice. (a) 10 atoms unit cell used in structure optimization and *DFPT* calculations. (b) 40 atoms super-cell used in the calculation of condensing the  $M_{xy}$  mode. (c) 20 atoms super-cell used for condensing most of the unstable phonon modes at the Brillouin zone boundary.

As it is shown in Figure 3.1, a 10-atoms cell was used for the calculation of high-symmetry reference structure. In order to condense unstable rotation modes, a 20-atoms super cell was employed. We used tetragonal Monkhorst-Pack meshes of  $8 \times 8 \times 4$  to compute integrals in the Brillouin-zone of the 10-atoms cell and  $6 \times 6 \times 4$   $k$ -point

grid was used for the 20-atoms super cell. For the strained system,  $6 \times 6 \times 4$   $k$ -point mesh was used for 10-atoms cell as well. In structural relaxations, atomic positions were optimized until the residual force on atoms were below  $3 \times 10^{-4} \text{Hartree/Bohr}$ .

### 3.3 High-symmetry reference structure

#### 3.3.1 Relaxed reference structure

In this part, the high-symmetry tetragonal  $PTO/STO(1/1)$  system, which is of space group  $P4/mmm$  (No.123), will be investigated. In-plane refers to the  $x$ - $y$  directions and out-of-plane refers to the perpendicular  $z$  direction. We assume that the  $PTO/STO(1/1)$  superlattice is grown on a  $SrTiO_3[001]$  substrate, so that the in-plane lattice constant is fixed to the theoretical bulk cubic  $SrTiO_3$  value (3.845 Å).

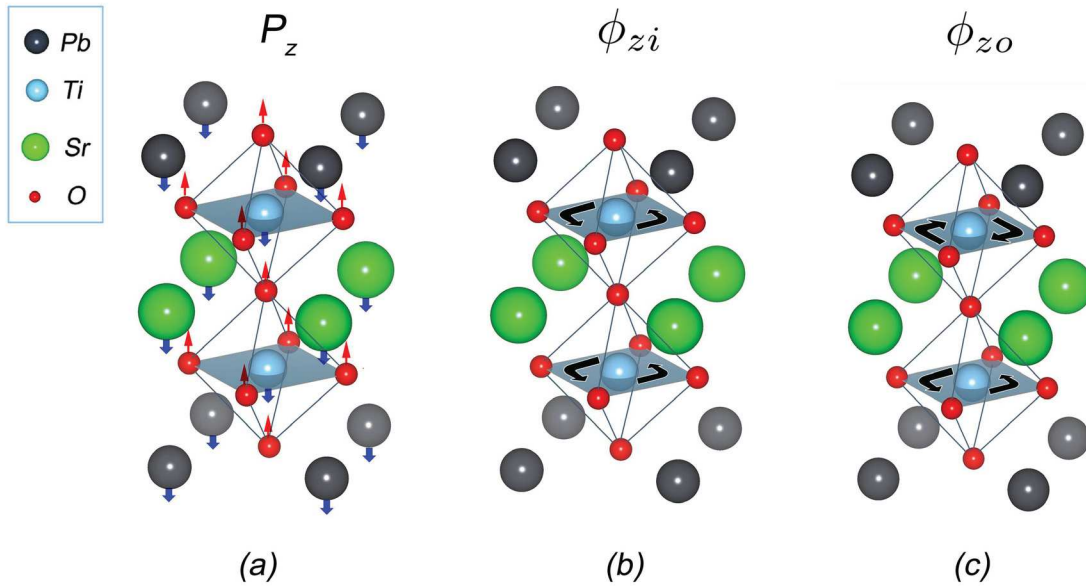


FIGURE 3.2: Unstable phonon modes that correspond to the atomic motion polarized or rotated along  $z$  axis in the  $PTO/STO(1/1)$  system. (a) The polar mode along  $z$  axis ( $FE_z$ ) in which  $O$  atoms move against cations. (b) The in-phase rotation  $\phi_{zi}$  where the two octahedras along  $z$  axis rotate in the same direction. (c) The out-of-phase rotation  $\phi_{zo}$  where the two octahedras along  $z$  axis rotate in the opposite directions.

After full relaxation, the atomic positions and the out-of-plane lattice constants were obtained and reported and compared with the experimental values in Table 3.1. From

there we can see that, comparing with the experimental values, the *LDA* approximation under-estimates the lattice constant by 1~2% error. In addition, the out-of-plane thickness of the perovskite layer is close to the lattice constant of bulk cubic  $PbTiO_3$  (0.1% error), which means that the perovskite unit cell has been pulled a little along  $z$  direction and there is compressive epitaxial in-plane strain on the  $PbTiO_3$  cell.

TABLE 3.1: Relaxed lattice constants (in Å) of  $PTO/STO(1/1)$  superlattices, bulk  $PbTiO_3$  and bulk  $SrTiO_3$  from calculations and experiment

$PTO/STO$		$PbTiO_3$		$SrTiO_3$	
a	c/2	cubic	Exp. <sup>a</sup>	cubic	Exp. <sup>a</sup>
3.845	3.876	3.880	3.969	3.845	3.905

<sup>a</sup>Reference[140]

In addition, we calculated the total energy of the high-symmetry phase unit cell by applying different k-grids. The results are reported in Table 3.2. We take the  $8 \times 8 \times 8$  k-grid case as the reference and report the energy difference between it and other k-grid cases. The energy of each case was renormalized equivalently to the 10 atoms unit cell. From Table 3.2, we can see that the energy differences are lower than  $1 meV/f.u.$ , within our error tolerance, except for the  $4 \times 4 \times 4$  k-grid case.

TABLE 3.2: Energy convergence of  $PTO/STO(1/1)$  superlattice with different k-grid (in  $meV/f.u.$ ). The energy is reported as the value relative to the  $8 \times 8 \times 8$  k-grid case.

$k$ -grid	Atoms per cell	$\Delta E(meV/f.u.)$
$8 \times 8 \times 8$	10	0.00
$8 \times 8 \times 4$	10	-0.10
$6 \times 6 \times 4$	10	-0.82
$6 \times 6 \times 4$	20	-0.11
$4 \times 4 \times 4$	20	-1.89

### 3.3.2 Phonon dispersion curves

The phonon dispersion curves of  $PTO/STO(1/1)$  superlattice were obtained by applying the *DFPT* formalism as implemented in *ABINIT*. The phonon dispersion curves are shown in Figure 3.3 and exhibit many phonon instabilities in Brillouin zone. These unstable phonon modes might drive the phase transition, so our investigation will mainly trace these modes. We report the frequency of each unstable mode in Table 3.3. The high symmetry points of the Brillouin zone are labelled as follows:

$\Gamma(0, 0, 0)$ ,  $X(1/2, 0, 0)$ ,  $M(1/2, 1/2, 0)$ ,  $R(1/2, 1/2, 1/2)$ ,  $Z(0, 0, 1/2)$  and  $W(0, 1/2, 1/2)$  in units of the reciprocal lattice unit vectors.

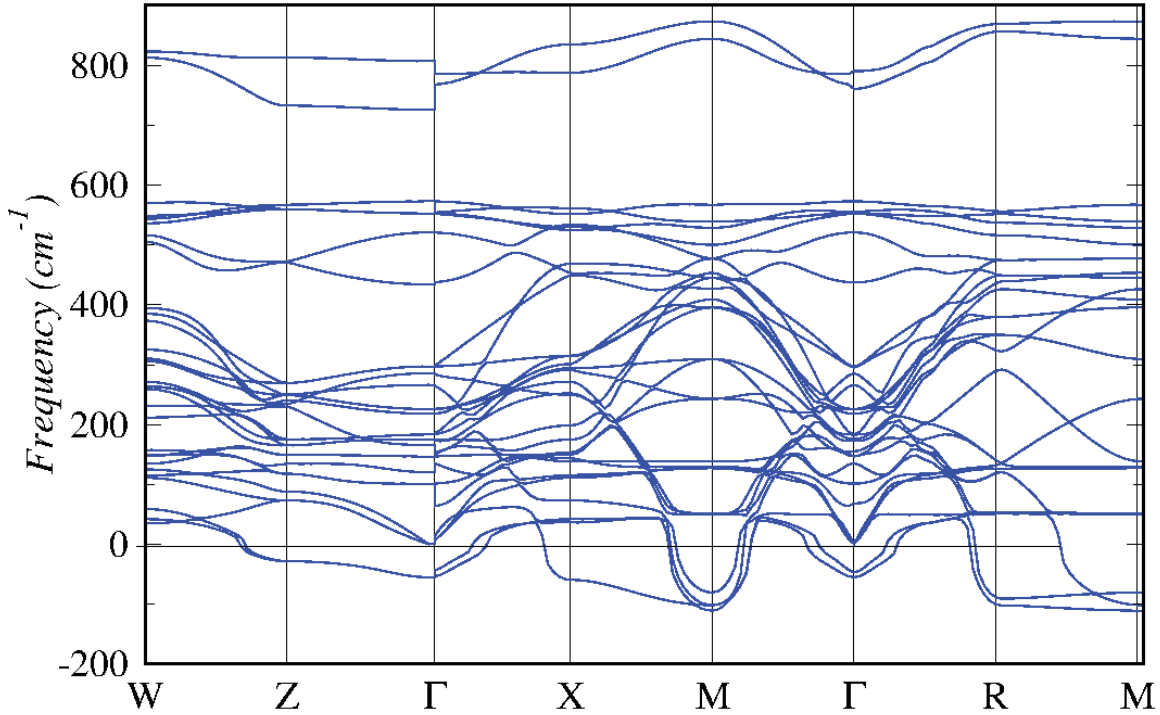


FIGURE 3.3: Phonon dispersion curves of the  $(PTO/STO)(1/1)$  superlattice. The phonon frequencies are presented in the unit of  $cm^{-1}$ . The imaginary values are reported as negative ones.

The lowest phonon frequency is found at  $M$  point at which four unstable phonon modes are found overall which propagate in the  $x$ - $y$  plane. By examining the eigenvector of the lowest one, an antiferrodistortive mode corresponding to octahedra out-of-phase rotations along  $z$  axis ( $\phi_{zo}$ , shown in figure 3.2(c)) is revealed which means along the rotation axis, two consecutive octahedra rotating in opposite directions. The second and the third lowest modes have the same frequency and correspond to an oxygen atoms rotation along  $x$  or  $y$  direction and combines additional displacements of  $Pb$ ,  $Sr$  and  $Ti$  atoms. These two modes stiffen up rapidly when going away from the  $M$  point. The fourth lowest mode reveals an antiferro-distortion mode which corresponds to octahedra in-phase rotation along the  $z$  axis ( $\phi_{zi}$ , shown in figure 3.2(b)), which means along the rotation axis, two consecutive octahedra rotating in the same direction. The  $\phi_{zo}$  and  $\phi_{zi}$  modes remain unstable at  $R$  point and along  $M$ - $R$  branch with little dispersion: the  $\phi_{zo}$  mode stiffens up a little and the  $\phi_{zi}$  mode becomes softer.

There are three unstable phonon modes at  $\Gamma$  point. The first and the second have same frequency and correspond to in-plane atomic polar motion along  $x$  or  $y$  ( $P_x$  or  $P_y$ ) where the cations and the oxygen atoms move along opposite directions. The third one reveals a ferroelectric polar mode along  $z$  direction ( $P_z$ , shown in figure 3.2(a)). The  $P_x$  and  $P_y$  modes remain unstable at  $Z$  point and along  $\Gamma$ - $Z$  branch with a significant dispersion. Besides, an unstable  $\phi_{yi}$  mode is found at  $X$  point as well.

TABLE 3.3: Frequency (in  $cm^{-1}$ ) of each unstable phonon mode, at the center and boundaries of Brillouin zone, for  $PTO/STO(1/1)$  superlattice under zero strain.

The imaginary values are reported as negative ones.

	$Z$	$\Gamma$	$X$	$M$	$R$
$1^{st}$	-28.18	-55.00	-59.34	-110.67	-102.26
$2^{nd}$	—	-55.00	—	-101.68	-90.74
$3^{rd}$	—	-44.88	—	-101.68	—
$4^{th}$	—	—	—	-80.64	—

### 3.3.3 Strain effects

Strain engineering is known to be used to tune different ferro orders in perovskite systems. In our  $PTO/STO(1/1)$  superlattice, we induced strain in two ways, in-plane and out-of-plane. Here a 10 atoms unit cell and a  $6 \times 6 \times 4$  k-grid were used. The evolution of some selected phonon mode frequencies, including  $P_z$ ,  $P_x$  modes at  $\Gamma$  point and  $\phi_{zi}$ ,  $\phi_{zo}$  modes at  $R$  point, under different epitaxial strain are shown in figure 3.4.

We clearly see that the  $P_z$  mode is strongly strain-dependent while the other three selected modes are less sensitive to the strain. For tensile out-of-plane strain ( $\eta_z > 0$ ), the  $P_z$  mode is unstable and rapidly softening. Its frequency increases under compressive out-of-plane strain ( $\eta_z < 0$ ) and become stable at a critical epitaxial strain  $\eta_z = -0.4\%$ . The other three modes remain unstable under compressive and tensile out-of-plane strain. The  $P_x$  mode decreases smoothly under tensile out-of-plane strain and increase first at compressive out-of-plane strain but starts to decrease again at  $\eta_z = -1\%$ .  $\phi_{zi}$  and  $\phi_{zo}$  are softening smoothly under tensile out-of-plane strain and stiffen up slowly under compressive epitaxial strain while the  $\phi_{zo}$  mode always remains the lower frequency mode.

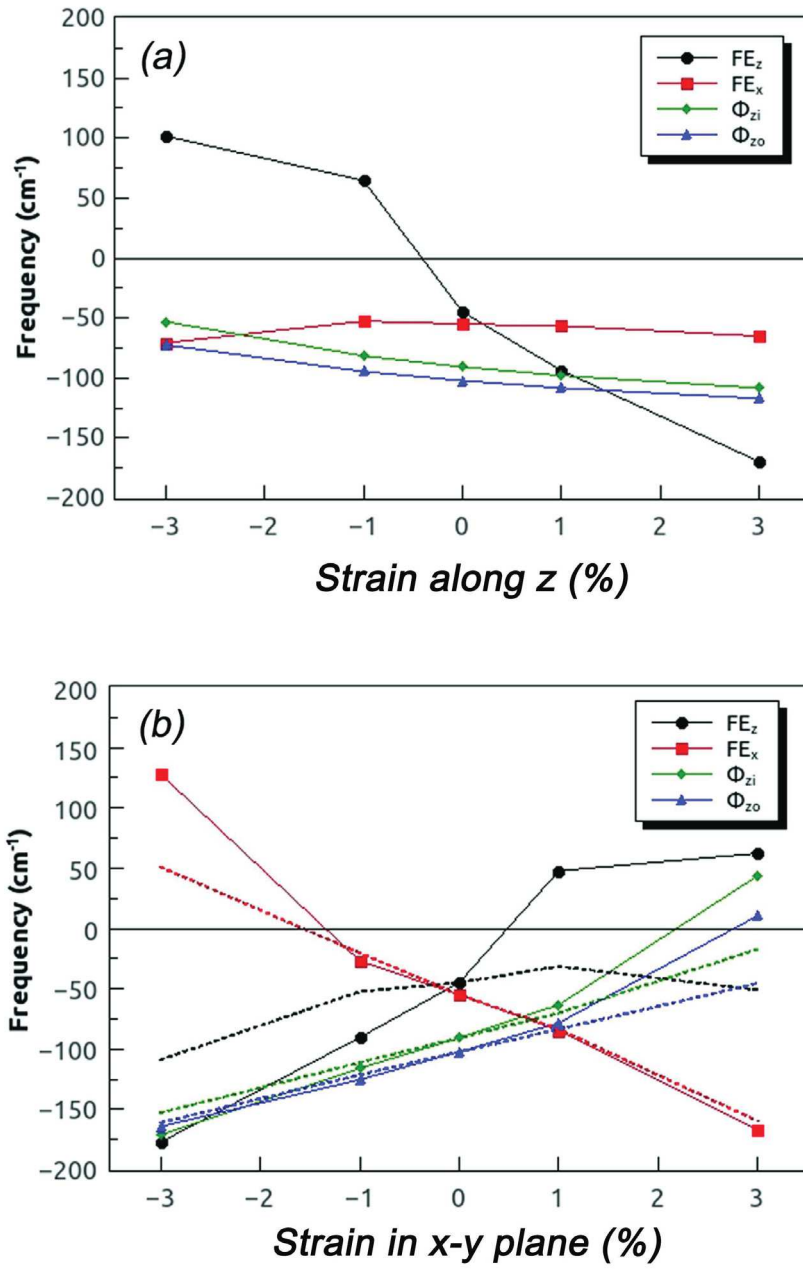


FIGURE 3.4: Phonon frequency (in  $cm^{-1}$ ) of selected modes, under different strains, including  $P_z$ (black),  $P_x$ (red) modes at  $\Gamma$  point and  $\phi_{zi}$ (green),  $\phi_{zo}$ (blue) modes at  $R$  point. The imaginary values are reported as negative ones. (a) Strain applied along  $z$  direction while the in-plane lattice constant is fixed at the bulk  $SrTiO_3$  value. (The strain is defined as  $\eta_z = (c_s - c_0)/c_0$  where  $c_0$  is the relaxed  $z$  component lattice constant of  $PTO/STO(1/1)$  and  $c_s$  is the  $z$  component lattice constant of  $PTO/STO(1/1)$  after strain is applied). (b) In-plane strain applied under relaxed  $c$  (solid line) and fixed  $c$  (dashed line). (The strain is defined as  $\eta_{xy} = (a_s - a_0)/a_0$  where  $a_0$  is the  $x$  component lattice constant which is fixed to the bulk cubic  $SrTiO_3$  value and  $a_s$  is the  $x$  component lattice constant of  $PTO/STO(1/1)$  after epitaxial strain is applied).

For the relaxed  $c$  parameters, we can see that all the selected modes are more sensitive to the in-plane epitaxial strain when compared to the case of out-of-plane strain. For tensile epitaxial strain ( $\eta_{xy} > 0$ ), the  $P_x$  mode frequency decreases rapidly whereas the  $P_z$  mode frequency increases significantly until it becomes stable at a critical strain value  $\eta_{xy} = 0.5\%$ . For compressive epitaxial strain, a similar behavior is observed but here the  $P_z$  mode frequency decreases and the  $P_x$  mode frequency becomes stable at  $\eta_{xy} = -1.3\%$ . The frequencies of  $\phi_{zi}$  and  $\phi_{zo}$  mode are unstable and decrease for compressive epitaxial strain while they increase for tensile epitaxial strain until they become stable at  $\eta_{xy} = 2.1\%$  for  $\phi_{zi}$  and  $\eta_{xy} = 2.8\%$  for  $\phi_{zo}$ . For the fixed  $c$  value, the behaviors of all the selected modes are similar to the ones for relaxed  $c$  parameter. The only exception is the  $P_z$  mode which decreases smoothly under compressive epitaxial strain and increases first at tensile epitaxial strain but start to decrease again at  $\eta_{xy} = 1\%$ . This is similar to the  $P_x$  modes behavior under out-of-plane strain.

From figure 3.4 we can see the ferroelectric (in-plane and out-of-plane) and antiferro-distortion phonon instability coexist under small epitaxial strain ( $|\eta| < 1\%$ ) especially when the lattice constant perpendicular to the direction of epitaxial strain is fixed.

## 3.4 Relevant degrees of freedom in ground state

### 3.4.1 Energy landscape

It is observed from the phonon dispersion curves that there are many phonon instabilities in the  $P4/mmm$  phase of *PTO/STO(1/1)* system. To determine the ground state, we performed full relaxation initialized by condensing each unstable phonon mode independently and condensing some of selected modes together under zero in-plane strain. Then we obtained each intermediate phase and report their energy relative to the  $P4/mmm$  high symmetry reference phase in Table 3.6. From there we can see that when we condense each unstable mode individually, the  $R_z$  phase ( $P4/nbm$ ), in which only  $\phi_{zo}$  mode exists, provides the lowest energy.

It is also shown in Table 3.6 that when we combine some unstable modes and condense them, lower energy phases appear. For instance, we can see that the  $R_z M_z P_z$  ( $P4bm$ ) phase which was defined as the ground state in Ref.[20], has a lower energy than the

TABLE 3.4: Amplitude of  $P_z$   $\phi_{zi}$  and  $\phi_{zo}$  atomic motions for each selected phase (corresponding to the polar or rotation motion along  $z$  axis) and energy gain (in  $meV/f.u.$ ) with respect to the  $P4/mmm$  phase of  $PTO/STO(1/1)$  superlattice.

	$P_z$	$\phi_{zi}$	$\phi_{zo}$	Energy ( $meV$ )	
	( $C/m^2$ )	(degree)	(degree)	10 atoms cell	20 atoms cell <sup>b</sup>
$P_z(P4/mmm)$	0.13	0	0	-0.53	-3
$M_z(P4/mbm)$	0	4.86	0	-9.64	-28
$R_z(P4/nbm)$	0	0	6.43	-32.53	-73
$R_zM_zP_z(P4bm)$	0.19	3.15	5.04	-34.4	-81

<sup>b</sup>Reference.[20]

$R_z$  phase whereas the  $\phi_{zo}$ ,  $\phi_{zi}$  and  $P_z$  atomic distortions are coexisting. In-plane strain effects have been tested in previous work [141] which showed that the ground state of the  $PTO/STO(1/1)$  system will be the  $R_zM_zP_z$  phase under compressive in-plane strain and be  $R_{xy}M_zP_{xy}$  ( $Pmc2_1$ ) phase under tensile strain, where the system prefers the in-plane component distortions as shown in figure 3.5. It is also indicated in Ref.[141] that for small strain, the in-plane and out-of-plane distortions could coexist which means that the  $R_{xyz}M_zP_{xyz}$  ( $Pc$ ) phase is the ground state under small strain. These conclusions are in agreement with our results that under zero in-plane strain, the  $R_{xyz}M_zP_{xyz}$  phase has the lowest energy and  $R_{xy}M_zP_{xy}$  lies at higher energy than  $R_zM_zP_z$ . Our results in figure 3.4 also support that the in-plane polar motion ( $P_x$ ) is more unstable than the out-of-plane one ( $P_z$ ) under tensile strain. The  $P_z$  mode even can be stable when we relax the lattice constant along  $z$ .

From Table 3.6 we notice that the energy difference between  $R_{xyz}M_zP_{xyz}$  phase and  $R_zM_zP_z$  is in fact extremely small ( $\Delta E < 1 emV$ ) and below the limit of accuracy of our calculations. Consistently, the contribution of in-plane distortions is negligible so that the main physics is dominated by  $R_zM_zP_z$  consistently with Ref. [20]. We will try to build a simple model by just considering the  $R_z$   $M_z$  and  $P_z$  degrees of freedom in the next section.

### 3.4.2 Landau type model

We report the energy relative to the  $P4/mmm$  of the  $P_z$ ,  $M_z$ ,  $P_z$  and  $P_zM_zR_z$  phase in Table 3.4 under fixed  $z$  component lattice constant. These values are consistent with those reported in Ref. [20]. The energy gain of each phase are smaller than the values in Ref. [20]. These differences can be traced back in the different accuracy

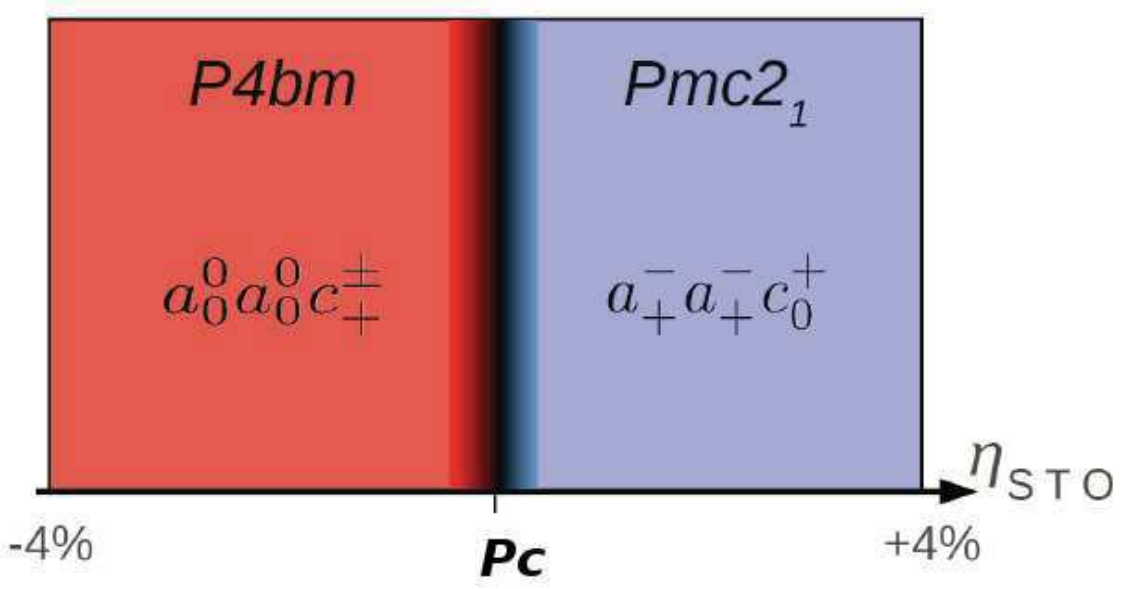


FIGURE 3.5: The space groups for ground state of  $PTO/STO(1/1)$  superlattices under different in-plane strain. The strain is given with respect to the lattice constant of cubic  $SrTiO_3$  under zero strain.

for structure relaxation and in the subsequent different lattice constants at which the calculations have been performed. These four phases indicate local minima points (or maybe saddle) in the global energy landscape. We take  $P_z$ ,  $\phi_{zi}$  and  $\phi_{zo}$  order parameters as the basis to build the energy space and describe the energy surface by using the Landau type energy expansion as follows:

$$\begin{aligned}
 E(P_z, \phi_{zi}, \phi_{zo}) = & \alpha_1 P_z^2 + \beta_1 P_z^4 + \alpha_2 \phi_{zi}^2 + \beta_2 \phi_{zi}^4 + \alpha_3 \phi_{zo}^2 + \beta_3 \phi_{zo}^4 \\
 & + \gamma_{12} P_z^2 \phi_{zi}^2 + \gamma_{13} P_z^2 \phi_{zo}^2 + \gamma_{23} \phi_{zi}^2 \phi_{zo}^2 \\
 & + \lambda P_z \phi_{zi} \phi_{zo}
 \end{aligned} \tag{3.1}$$

The first line in (3.1) corresponds to the double-well potential of each individual mode. The second line provides the biquadratic coupling between each two modes. The third line is the trilinear coupling which was previously identified as key to a novel type of improper ferroelectricity in  $PTO/STO(1/1)$  systems. We report the polarization (along  $z$ ) and the angle of octahedra rotation in Table 3.4 as well, on the basis of which we obtain each parameter ( reported in Table 3.5) in energy expansion (3.1):

Here we label following points.  $G_1$  refers to (0.13, 0, 0),  $G_2$  refers to (0, 4.84, 0),  $G_3$  refers to (0, 0, 6.43) and  $G_0$  refers to (0.19, 3.15, 5.04).  $\alpha_1$ ,  $\alpha_2$  and  $\alpha_3$  have negative

TABLE 3.5: Parameters of the model described in the text in the standard unit.

$\alpha_1$	$\alpha_2$	$\alpha_3$	$\beta_1$	$\beta_2$	$\beta_3$	$\gamma_{12}$	$\gamma_{13}$	$\gamma_{23}$	$\lambda$
-62.722	-0.816	-1.574	1855.680	0.017	0.019	7.252	14.520	0.082	-12.256

values confirming the double-well shape when individual modes are condensed (as shown in figure 3.6 (a),(b),(c)), the minimum in energy are found at  $G_1$ ,  $G_2$  and  $G_3$  point. Values of  $\gamma_{12}$ ,  $\gamma_{13}$  and  $\gamma_{23}$  indicates that the coupling between two of these modes are different, and the one between  $\phi_{zi}$  and  $\phi_{zo}$  is relatively smaller. The amplitude of  $\lambda$  is similar to  $\gamma_{13}$  which implies that the contribution of the trilinear coupling between  $P_z$ ,  $\phi_{zi}$  and  $\phi_{zo}$  is important in the energy surface behavior.

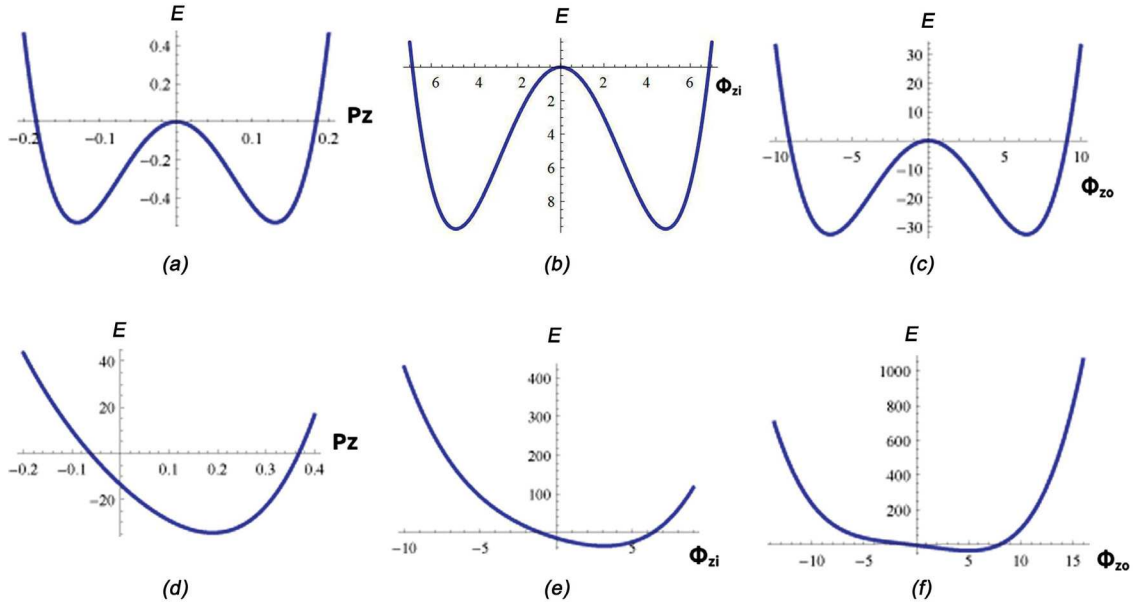


FIGURE 3.6: The 1D total energy (in  $meV/f.u.$ ) curve  $E(P_z, \phi_{zi}, \phi_{zo})$  with respect to only one degree of atomic motion: (a)  $E(P_z, 0, 0)$ ; (b)  $E(0, \phi_{zi}, 0)$ ; (c)  $E(0, 0, \phi_{zo})$ ; In the case for which two of these degrees are fixed at the ground state value: (d)  $E(P_z, 3.15, 5.04)$ ; (e)  $E(0.19, \phi_{zi}, 5.04)$ ; (f)  $E(0.19, 3.15, \phi_{zo})$ .

The global minimum energy is observed at  $G_0$  point. When we fix the values of two modes and change the other one, a single-well energy curve is obtained as shown in Figure 3.6 (d), (e), (f). Taking (d) as an example, the lowest energy of the single-well energy curve is found at a non-zero polarization point which is the key character of improper ferroelectrics. Similar behaviors are found, which correspond to other rotation modes.

When we suppress  $P_z$  (set  $P_z=0$ ), we will obtain the 2D contour plot of the energy landscape shown in figure 3.7(a), from where we can see that  $\phi_{zi}$  and  $\phi_{zo}$  modes are

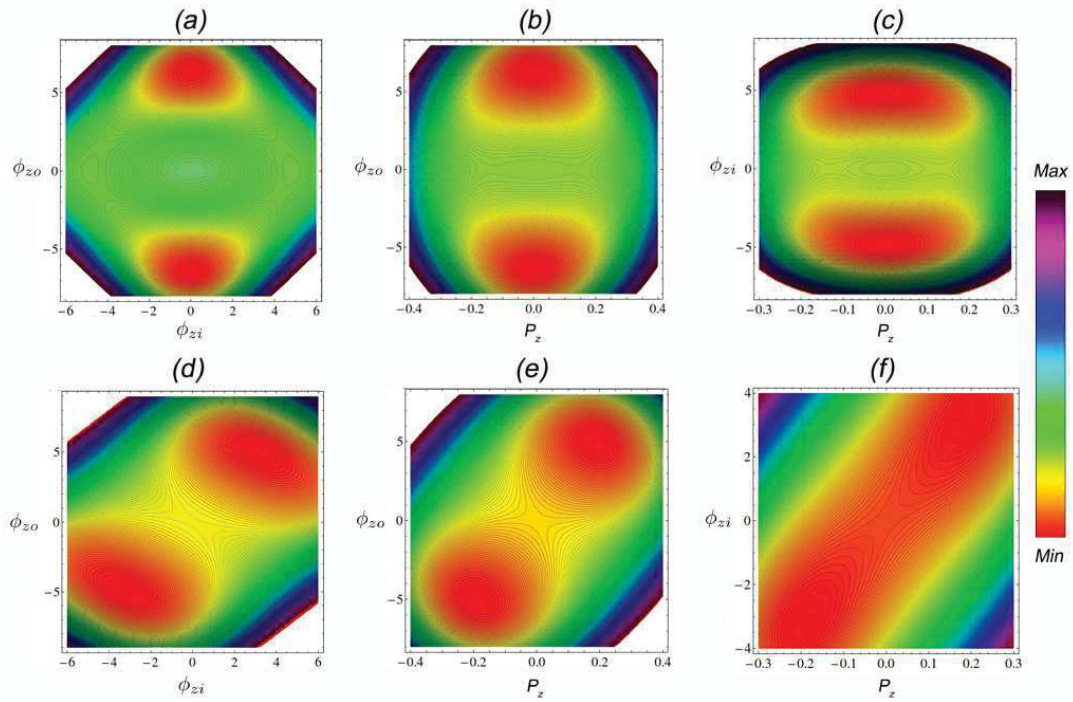


FIGURE 3.7: The 2D total energy (in  $meV/f.u.$ ) plot  $E(P_z, \phi_{zi}, \phi_{zo})$  with respect to two degrees of atomic motion:(a)  $E(0, \phi_{zi}, \phi_{zo})$ ; (b)  $E(P_z, 0, \phi_{zo})$ ; (c)  $E(P_z, \phi_{zi}, 0)$ ;(d)  $E(0.19, \phi_{zi}, \phi_{zo})$ ; (e)  $E(P_z, 3.15, \phi_{zo})$ ; (f)  $E(P_z, \phi_{zi}, 5.04)$ .

unstable, and the condensation of one of them will quickly suppress the instability with respect to the other. The lowest energy corresponds to the pure  $\phi_{zo}$  mode. Similar features are shown in figure 3.7(b) and (c) which correspond to the cases of  $\phi_{zi}=0$  and  $\phi_{zo}=0$ .

If we fix the value of  $P_z$  to its value at the global minima point ( $P_z=0.19$ ) and plot the 2D energy landscape (as shown in figure 3.7(d)), two equivalent local minima are found at  $(0.19, 3.15, 5.04)$  and  $(0.19, -3.15, -5.04)$ . In this case,  $\phi_{zi}$  and  $\phi_{zo}$  do not suppress each other when one of them is condensed, the other one will condense automatically. Similar results occur when we fix  $\phi_{zi}$  as 3.15 or  $\phi_{zo}$  as 5.04, as shown in figure 3.7(e) and (f)

In figure 3.8, we change the amplitude of one mode and report the other behavior of two modes and the energy as well. We also report the energy curve in terms of one distortion mode by suppressing the other two modes. It is observed in figure 3.8(a) that, when  $P_z=0$ ,  $\phi_{zi}$  is suppressed, only  $\phi_{zo}$  exists, which confirms the results of figure 3.7 and is consistent with what was reported in Ref.[20]. As  $P_z$  increases,  $\phi_{zo}$  will decrease,  $\phi_{zi}$  will increase to a maximum value and decrease.  $\phi_{zo}$  and  $\phi_{zi}$  will vanish all together. Similar observations are done when exchanging these three

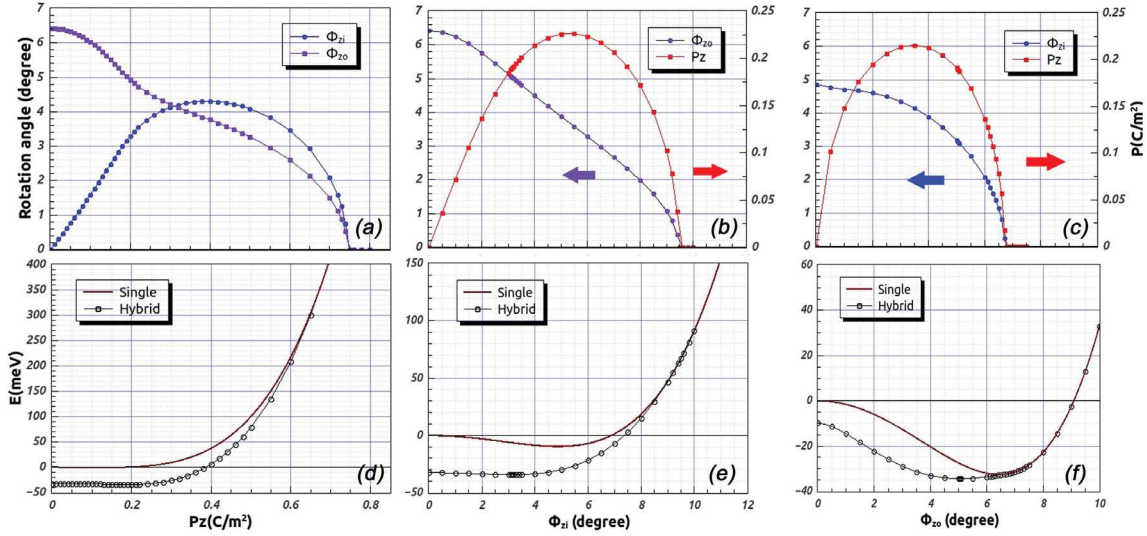


FIGURE 3.8: The amplitude of each distortion mode, in degree for rotation mode (left side) and in  $C/m^2$  for polar mode (right side): (a) the amplitude of  $\phi_{zi}$  (blue) and  $\phi_{zo}$  (purple) modes; (b) the amplitude of  $P_z$  (red) and  $\phi_{zo}$  (purple) modes; (c) the amplitude of  $\phi_{zi}$  (blue) and  $P_z$  (red) modes; (d), (e), (f) energy when the three modes coexist (black) and when only one mode exist (brown).

modes. According to our results, only one distortion mode can survive at high energy and the other two will start to condense at some point when energy decreases. This coupling will decrease energy which is confirmed in figure 3.8, in which the energy is lower when these three modes coexist.

### 3.4.3 Temperature dependent Landau model

The model discussed above is valid at zero Kelvin. In order to describe the phase transition behavior, we introduce the temperature factor to the quadratic terms as usual in Landau theory:

$$\begin{aligned}
 E(P_z, \phi_{zi}, \phi_{zo}) = & \alpha'_1(T - T_1)P_z^2 + \beta_1P_z^4 + \alpha'_2(T - T_2)\phi_{zi}^2 + \beta_2\phi_{zi}^4 + \alpha'_3(T - T_3)\phi_{zo}^2 + \beta_3\phi_{zo}^4 \\
 & + \gamma_{12}P_z^2\phi_{zi}^2 + \gamma_{13}P_z^2\phi_{zo}^2 + \gamma_{23}\phi_{zi}^2\phi_{zo}^2 \\
 & + \lambda P_z\phi_{zi}\phi_{zo}
 \end{aligned} \tag{3.2}$$

where  $T_j$  ( $j=1,2,3$ ) are the phase transition temperatures at which each single order distortion will condense in the system ( $P_z$  at  $T_1$ ,  $\phi_{zi}$  at  $T_2$  and  $\phi_{zo}$  at  $T_3$ ). In order

to provide the right behavior at  $T=0$ ,  $\alpha'_j$  ( $j=1,2,3$ ) are defined as:  $\alpha_j = -\alpha'_j T_j$ , where  $\alpha_j$  are the parameters in Equation 3.1.

The temperature evolution of  $P_z$ ,  $\phi_{zi}$  and  $\phi_{zo}$  can change drastically depending of the choice of the  $T_j$ s. However, it is observed that this model can well reproduce the experimental results in [20] from some specific choices. When we set  $T_1=52K$ ,  $T_2=500K$  and  $T_3=500K$ , as shown in Figure 3.9, the three order parameters condense together at  $500K$ . The polarization exhibits linear behavior with  $T$  and evolves toward value  $0.19C/m^2$  comparable to experiment at  $T=0$  and there is no divergence of the dielectric constant at the phase transition temperature. The system is in  $P4/mmm$  phase above  $T_3$  and in  $P4bm$  phase below  $T_3$ . It shows that this simple model can well describe the *PTO/STO(1/1)* system which includes many order parameters. It can confirm that such a system can exhibit a typical improper ferroelectric behavior (linear evolution of  $P$  and no divergence of dielectric constant). This is however reproduced for a specific choice  $T_2 = T_3$ . This is not imposed by symmetry. It can only be coincidental and seems rather unlikely. Now, it is very interesting to observed that the improper ferroelectric behavior seems not restricted to that case.

It is observed in Figure 3.9 that, if we set  $T_1=50K$ ,  $T_2=490K$  and  $T_3=500K$ , there are two critical points.  $\phi_{zo}$  mode appears first at  $T_3=500K$  and  $P_z$  appears then together with  $\phi_{zi}$  at around  $T_2=490K$ . The polarization keeps its linear behavior and the dielectric constant does not exhibit divergence around phase transition temperatures. The system is in  $P4/nbm$  phase in a small temperature range ( $490K < T < 500K$ ). It demonstrates that  $\phi_{zi}$  does not have to condense with  $\phi_{zo}$ , in order to reproduce an improper ferroelectric behavior. This appears as an unexpected and seems a very important result.

Although  $T_1$  and  $T_2$  does not have to condense at the same temperature, we see that the system can continue to behave as an improper ferroelectric as long as they remain sufficiently close to each others.

This is more likely what happens experimentally. We notice that only  $P_z$  has been measured and that both  $\phi_{zi}$  and  $\phi_{zo}$  as only the latter appear at the same temperature. We also notice that the fact we have one or two consecutive phase transitions might also depend on the strength of the trilinear term. In case it is large enough it could produce an avalanche transition even when  $T_2 \neq T_3$ . The key point here is that the trilinear behavior of  $P$  appears rether robust and seems not restricited to the specific case  $T_2 = T_3$ .

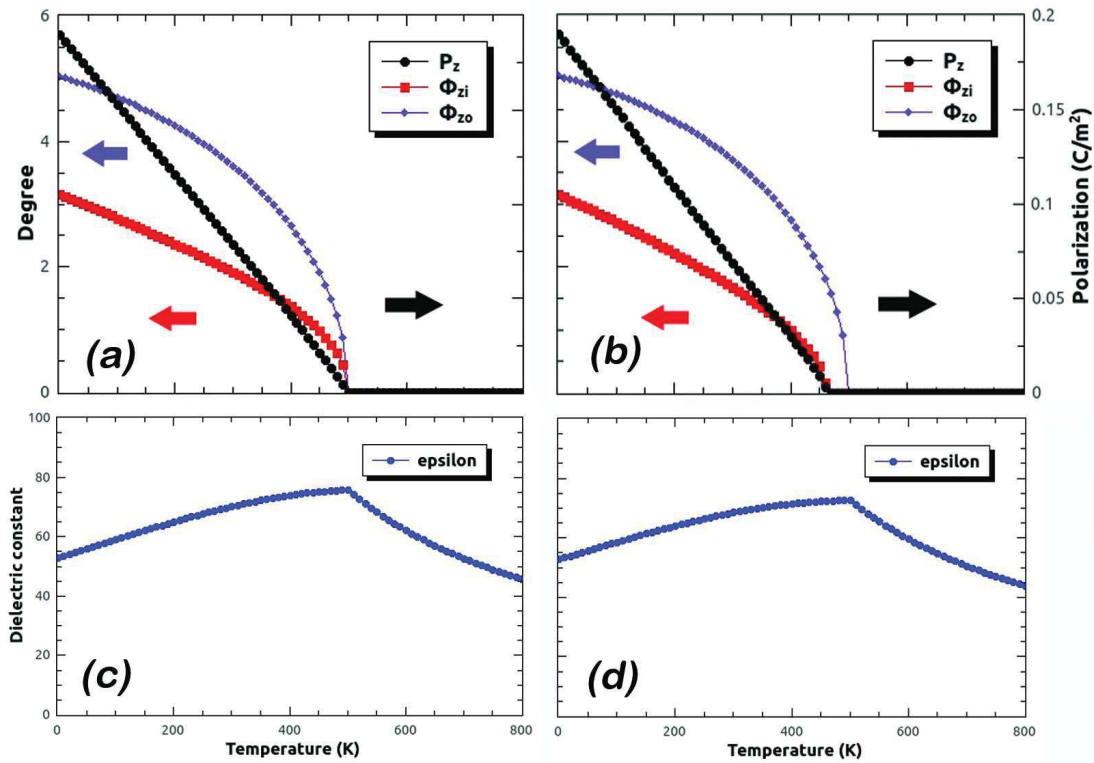


FIGURE 3.9: Different values for  $T_1$ ,  $T_2$  and  $T_3$  in equation 3.2: (a) The amplitude of each atomic distortion mode for polarization mode (right axis) and for rotation mode (left axis) under different temperatures when we set  $T_1=52K$ ,  $T_2=500K$  and  $T_3=500K$ ; (b) The amplitude of each atomic distortion mode for polarization mode (right axis) and for rotation mode (left axis) under different temperatures when we set  $T_1=50K$ ,  $T_2=490K$  and  $T_3=500K$ ; (c) Dielectric constant under different temperatures when we set  $T_1=52K$ ,  $T_2=500K$  and  $T_3=500K$ ; (d) Dielectric constant under different temperatures when we set  $T_1=50K$ ,  $T_2=490K$  and  $T_3=500K$ .

It is worth to point out that the above investigations have been performed at the phenomenological level. It is interesting to confirm such a possibility at the microscopic level. To study this issue from first-principles, a finite temperature model potential approach is needed, which will be introduced in the next section.

### 3.5 Model potential

As discussed above, the limitations of our Landau model approach arise mainly from two aspects: i) only  $P_z$ ,  $M_z$  and  $R_z$  are considered while other degrees of freedom exist; ii) the parameters are fitted on first-principles results at 0 K and the temperature dependence can only be introduced in a phenomenological way. In order to access

TABLE 3.6: Energy (in  $meV/f.u.$ ) of  $PTO/STO(1/1)$  superlattice, for  $P4/mmm$  phase, and intermediate phases in the case of relaxed and fixed  $z$  component lattice constants under zero in-plane strain. the values are obtained by  $DFT$  calculations (using the  $LDA$  approximation) and from the effective model potential  $E_{eff}$ . The error between them is in the last column.

Mode	Symmetry	Space group	Lattice constant( $c$ )	Energy( $meV/f.u.$ )		Error(%)
				DFT( $LDA$ )	$E_{eff}$	
—	$P4/mmm$	123		0.000	0.000	—
$P_z$	$P4mm$	99	relaxed	-0.68	—	—
			fixed	-0.53	-0.49	-7.58
$P_x$	$Pmm2$	25	relaxed	-5.83	—	—
			fixed	-5.83	-4.33	-25.79
$P_{xy}$	$Amm2$	38	relaxed	-5.40	—	—
			fixed	-5.40	-5.58	3.30
$M_z$	$P4/mbm$	127	relaxed	-10.13	—	—
			fixed	-9.64	-9.71	0.77
$M_x$	$Pmmm$	47	relaxed	-3.15	—	—
			fixed	-3.00	-2.83	-5.67
$M_{xy}$	$P4/mmm$	123	relaxed	-3.09	—	—
			fixed	-2.93	-2.88	-1.56
$R_z$	$P4/nbm$	125	relaxed	-33.45	—	—
			fixed	-32.53	-33.47	2.89
$R_x$	$Cmmm$	65	relaxed	-25.39	—	—
			fixed	-24.19	-24.19	0.45
$R_{xy}$	$Pmma$	51	relaxed	-27.59	—	—
			fixed	-26.32	-26.23	-0.34
$R_z M_z P_z$	$P4bm$	100	relaxed	-37.26	—	—
			fixed	-34.41	-34.56	0.43
$R_{xy} M_z P_{xy}$	$Pmc2_1$	26	relaxed	-31.48	—	—
			fixed	-31.25	-31.95	2.23
$R_x M_z P_x$	$Amm2$	38	relaxed	-26.38	—	—
			fixed	-25.99	-26.23	0.93
$R_{xyz} M_z P_{xyz}$	$Pc$	7	relaxed	-37.46	—	—
			fixed	-35.14	-34.75	-1.11
$R_x R_z M_z$	$Cm$	8	relaxed	-37.44	—	—
			fixed	-35.03	—	—
$R_x R_z$	$C2/m$	12	relaxed	-33.51	—	—
			fixed	-32.76	—	—

the structural phase transitions in perovskites, a finite temperature microscopic theory, called “Effective Hamiltonian” method was introduced in literature [101–104], in which the thermal average of the quantities of interest are calculated by a standard Metropolis Monte Carlo method. However, in this “Effective Hamiltonian” method only a small set of relevant degrees of freedom are typically considered, which is

not sufficient for the *PTO/STO(1/1)* case, since many phonon instabilities coexist in the reference high-symmetry phase. Recently, a new “model potential” method was suggested by Wojde et al.[105] that is inspired from the “Effective Hamiltonian” approach but includes all the atomic degrees of freedom (briefly summarized in Chapter 2). In this section, we will apply this new ‘model potential’ method on our *PTO/STO(1/1)* system and investigate its finite temperature phase transition behavior.

In our Monte Carlo simulations, the Metropolis algorithm is applied to obtain the thermal averages. A  $8 \times 8 \times 4$  supercell was used with periodic boundary conditions which implies that for each sweep,  $8 \times 8 \times 4 \times 10$  displacement attempts were included. Our procedure started from 1000 K to 0 K; 20,000 thermalization sweeps and 20,000 sweeps for averages were performed.

### 3.5.1 Effective potential training set

Based on our model, we report, in figure 3.10, the energy curve of each intermediate phase compared with the minimum energy value obtained from first-principles for each phase. The minimum value of each curve (in figure 3.10) is reported in Table 3.6 as well. These results demonstrate that the first-principles results are well reproduced by our atomic potentials. It is observed that each phase shows a similar double-well behavior, and the lowest energy is found for the  $R_{xyz}M_zP_{xyz}$  almost superimposed to that of  $R_zM_zP_z$ . In addition,  $R_z$ ,  $R_{xy}M_zP_{xy}$  and  $R_zM_zP_z$  phases all have very low energy as well. This is consistent with our results from first-principles.

### 3.5.2 Temperature dependent behavior

The T-dependent behavior of our *PTO/STO(1/1)* system is studied by running Monte Carlo simulations in which all the degrees of freedom of atomic displacements and strains are involved. The results are shown in figure 3.10 in which it is observed that the  $P4/mmm$  phase is the stable state at high temperatures. When the temperature decreases, different atomic distortion modes condense and the amplitude of which increases in this anneal procedure. There are three phase transition temperatures  $T_1 \approx 330K$ ,  $T_2 \approx 200K$  and  $T_3 \approx 75K$  which correspond to three main phase transitions:  $P4/mmm \rightarrow P4/nbm \rightarrow P4bm \rightarrow Pmc2_1$ .

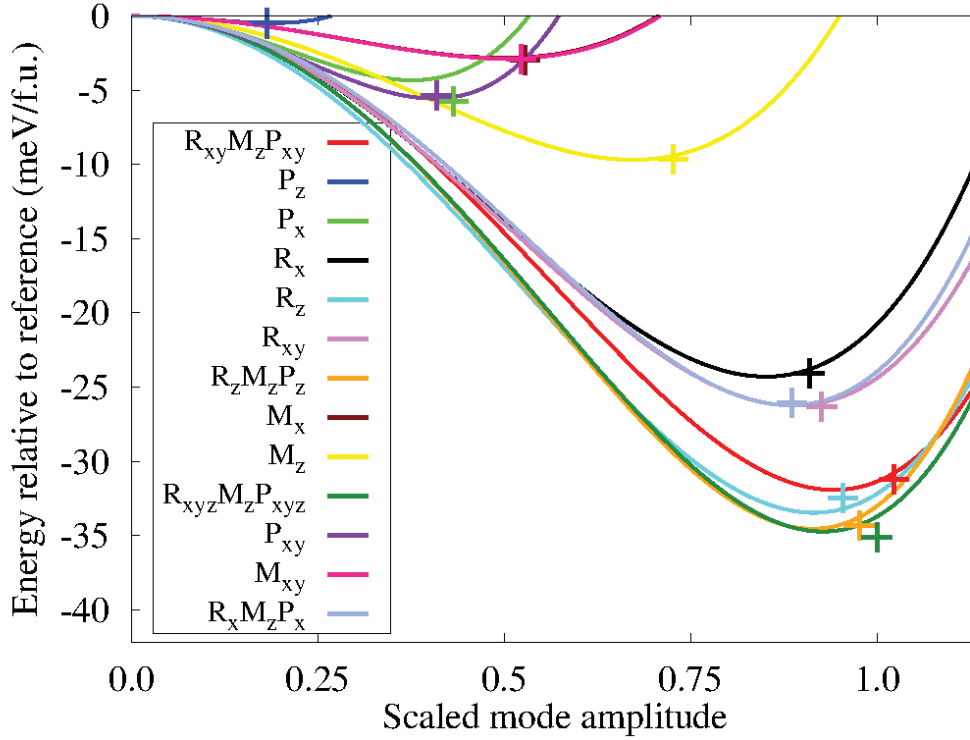


FIGURE 3.10: Total energy (in  $meV$ ) of each intermediate phase, relative to the reference  $P4/mmm$  phase, with respect to the scaled mode amplitude which are obtained from model potential. The crosses points indicate the total energy of each intermediate phase obtained from first-principle calculations.

The  $R_z$  mode appears first at  $T_1$ . The symmetry is broken from  $P4/mmm$  to  $P4/nbm$ . The amplitude of related  $\phi_{zo}$  rotation increases rapidly when the temperature decreases from  $T_1$  to  $T_2$ . This first phase transition supports the results from our Landau model at 0 K. It is observed that at  $T_2$ ,  $P_z$  and  $M_z$  appear together due to the trilinear coupling. Below  $T_2$ , the  $R_z$  mode exhibits linear behavior while the other two modes do not. Besides, the amplitudes of related  $P_z$  and  $\phi_{zi}$  modes increase rapidly while the  $\phi_{zo}$  amplitude still increases smoothly. The symmetry is broken into  $P4bm$  in which  $P_z$ ,  $M_z$  and  $R_z$  atomic distortions coexist.

When the temperature goes below  $T_3 \approx 75$  K,  $P_x$  and  $R_x$  modes start appearing and the symmetry is then  $Pmc2_1$ ;  $R_x$ ,  $P_z$ ,  $M_z$  and  $R_z$  all coexist below  $T_3 \approx 75$  K. Besides, at 0 K, the amplitude of each mode matches the results from first-principle. Figure 3.11 shows that the amplitudes of  $P_z$ ,  $\phi_{zi}$  and  $\phi_{zo}$  modes are significantly larger than that of  $\phi_{xo}$   $P_x$  which confirms that the main physics of the ground-state domains in the atomic distortion polarized or rotated along the  $z$  axis. The ones in-plane make negligible contributions, and only appear at very low temperatures.

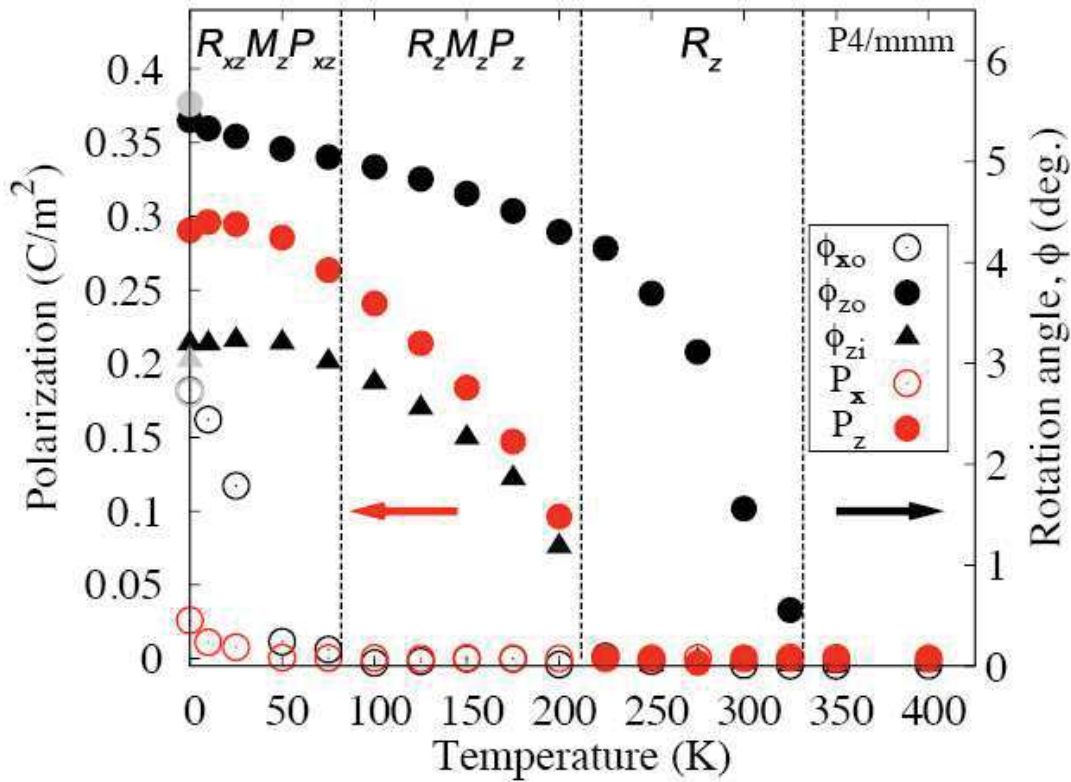


FIGURE 3.11: The amplitude of each atomic distortion mode in ( $C/m^2$ ) for polarization mode (red colour) and in degree for rotation mode (black colour) which are reported under different temperature (in  $K$ ).

This ground state ( $R_{xz}M_zP_{xz}$ ) can be understood as the coexistence of the phases  $R_zM_zP_z$  and  $R_xM_zP_x$  where both of them involve the  $\phi_{zi}$  mode atomic distortion. It suggests the possibility to control the amplitude of in-plane modes ( $\phi_{xo}$  and  $P_x$ ) by tuning the out-of-plane modes ( $\phi_{zo}$  or  $P_z$ ) due to these two types of coupling. Figure 3.12 shows one of the interesting possibility, that the  $z$  component of electric field can tune the in-plane polarization and rotation modes. It is observed that under zero external electric field, the  $PTO/STO(1/1)$  system has spontaneous in-plane and out-of-plane polarization while the amplitude of out-of-plane one is significantly larger than the in-plane one. When we increase the external electric field along  $z$ , the out-of-plane polarization is enhanced and the in-plane one is suppressed. The directions of these two degrees of polarization are switched by the  $z$  component of the electric field and they have the same value of depolarization field. It seems that  $P_x$  and  $P_z$  are in competition, one being suppressed by enhancing the other one under an external electric field along  $z$  direction. Similar features happen in the rotation modes. When there is no external field,  $\phi_{zi}$ ,  $\phi_{zo}$  and  $\phi_{xo}$  coexist in  $PTO/STO(1/1)$  system. The increasing  $z$  component of electric field will significantly increase  $\phi_{zi}$  and suppress the

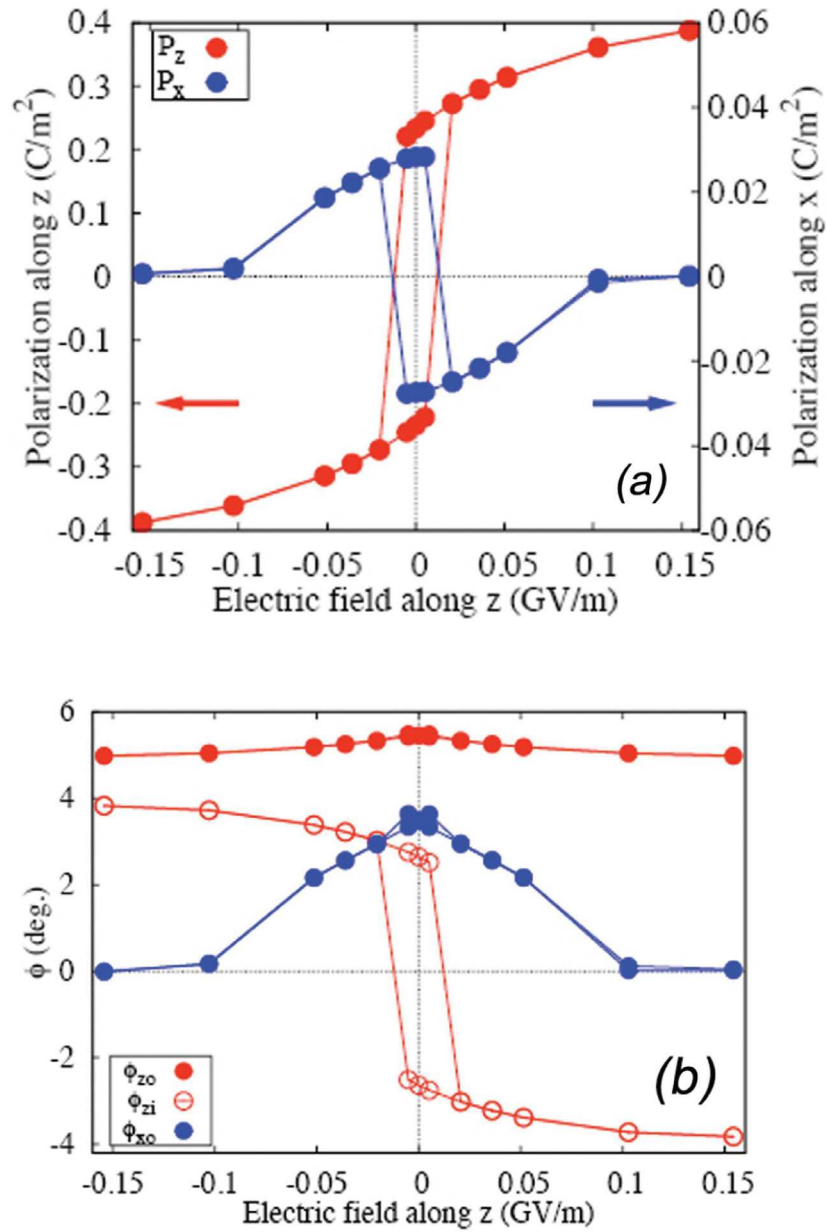


FIGURE 3.12: The amplitude of in-plane (red) and out-of-plane (blue) atomic distortion mode under external electric field (in GV/m) along  $z$  direction: (a) the amplitude of in-plane polarization  $P_x$  and out-of-plane polarization  $P_z$  (in  $C/m^2$ ); (b) the amplitude of in-plane rotation  $\phi_{xo}$  and out-of-plane rotation  $\phi_{zi}$  and  $\phi_{zo}$  (in degree).

amplitude of  $\phi_{xo}$ . The amplitude of  $\phi_{zo}$  is not sensitive in comparison with  $\phi_{zi}$  and  $\phi_{xo}$ , which are slightly decreased under an electric field along  $z$ . These phenomenon imply that under the external electric field along  $z$  direction, the  $PTO/STO(1/1)$  system has the tendency to be switched from the  $Pmc2_1$  phase to the  $P4bm$  phase, in which the in-plane atomic distortion mode  $P_x$  and  $\phi_{xo}$  will be suppressed. This is

similar to the effects of in-plane compressive strain.

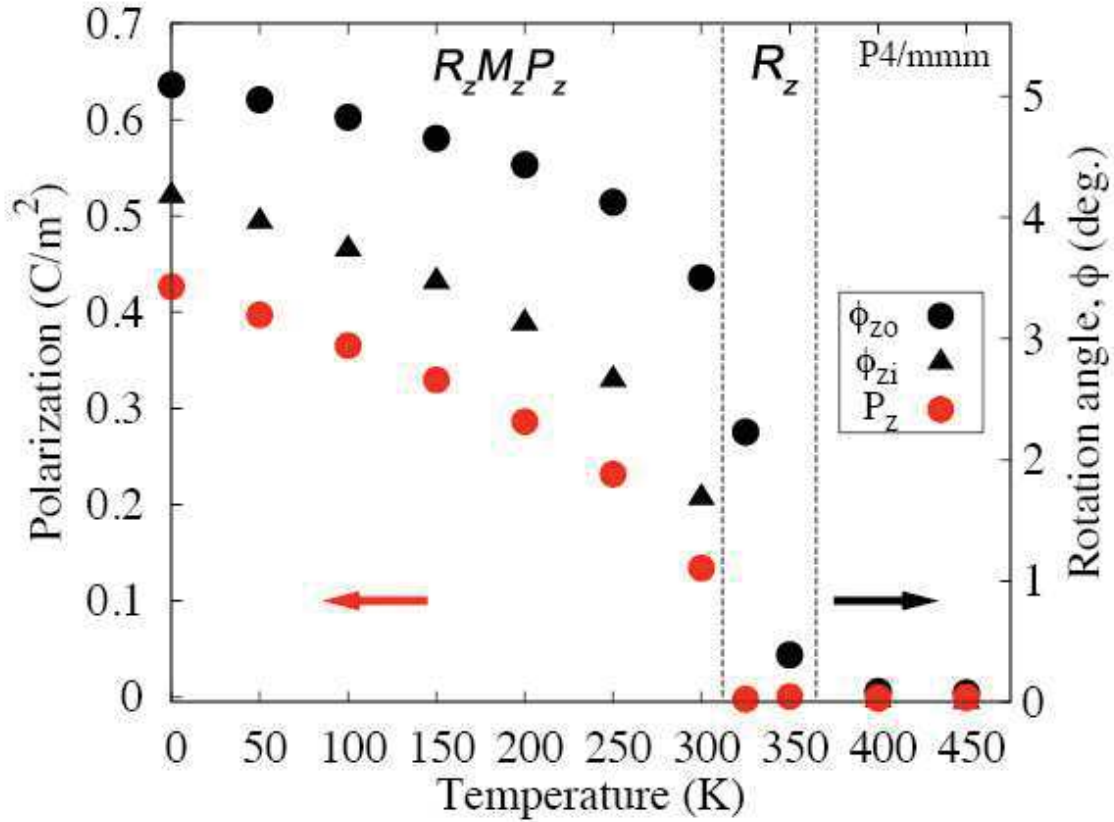


FIGURE 3.13: The temperature dependent amplitude of each atomic distortion mode in ( $C/m^2$ ) for polarization mode (red colour) and in degrees for rotation mode (black colour) which are reported under  $-6.9$  GPa pressure along  $z$  direction.

As previously discussed, the LDA slightly underestimates the lattice constants and lattice instabilities are very sensitive to strains. For these reasons, it is usual, when doing effective Hamiltonian calculations, to apply a negative pressure that compensate for the LDA volume underestimate. This typically provides results in close agreement with the experiments.

Figure 3.13 shows the temperature dependent sequence for the  $PTO/STO(1/1)$  under  $-6.9$  GPa pressure. The  $\phi_{xo}$  and  $P_x$  modes disappear and the ground-state is of purely  $P4bm$  phase. Compared to the previous case under zero external pressure, the two phase transition temperatures increase and become closer to each other ( $T_1 \approx 360K$  and  $T_2 \approx 320K$ ). It means that under tensile strain,  $P_z$ ,  $M_z$  and  $R_z$  modes have tendency to condense together at same temperature and the  $P4bm$  phase exists in a wider temperature range (from 0 K to 320 K). It confirms our results shown in figure 3.4, that under tensile strain, the  $P_z$  phonon mode will be more unstable than  $P_x$ . In addition, the negative pressure increases the phase transition temperatures  $T_1$

and  $T_2$  which implies that the high symmetry phase of the *PTO/STO(1/1)* system is more unstable under tensile pressure. This confirms that the finite temperature behavior is very sensitive to the parameters, although this should be further investigated. It suggests that properly compensating for LDA errors might eventually produce a unique phase transition ( $T_1=T_2$ ) as observed experimentally.

### 3.6 Conclusion and perspectives

In this chapter, we investigated the properties of *PTO/STO(1/1)* superlattices from first-principles. At zero Kelvin, the basic dynamical properties have been studied, including the phonon dispersion curves, the unstable phonon modes at the center and boundary of the Brillouin zone (BZ) and strain effects. There are different kinds of unstable oxygen rotational modes at the BZ boundary ( $\phi_{zi}$ ,  $\phi_{zo}$ ,  $\phi_{xo}$ ,  $\phi_{yo}$ ) and unstable ferroelectric polar modes in-plane ( $P_x$ ,  $P_y$ ) and out-of-plane ( $P_z$ ) at the BZ center. We noticed that the strain can strongly affect the lattice dynamics of the system, either softening or stiffening some modes. The different unstable modes also compete with each others.

The ground state (GS) of epitaxial *PTO/STO(1/1)* superlattices grown on a *STO* substrate was identified as a *Pc* phase corresponding to  $R_{xyz}M_zP_{xyz}$  and resulting from the combination of  $R_zM_zP_z$  and  $R_{xy}M_zP_{xy}$  distortions. However, the  $R_{xy}P_{xy}$  distortion contributes a very small amplitude to that GS and produces a gain of energy lower than the accuracy of the calculations. So, although our calculations support the fact that, on a *STO* substrate, the superlattice is in a configuration where in-plane and out-of-plane distortions can eventually coexist, it confirms that the main physics is dominated by the  $R_zM_zP_z$  distortion as initially proposed in Ref.[20].

A simple Landau type model was then developed, which only includes  $R_z$ ,  $M_z$  and  $P_z$  order parameters. This simple model well reproduces the first-principles energy data of each intermediate phase and highlights the importance of the trilinear coupling term. Such a simple model well reproduces the experimental results from previous literature. It also proposes the possibility that these three orders of atomic distortion may not have to appear at the same temperature; the first two primary order can condense individually, which is different from previous understanding of hybrid improper ferroelectricity.

In order to clarify further the temperature behavior of *PTO/STO* superlattices, first-principles model potentials have been constructed for this system. Then, using Monte-Carlo simulations, the temperature-dependent phase transition sequence was obtained. At high temperature, *PTO/STO(1/1)* system is in the high-symmetry  $P4/mmm$  phase. When the temperature decreases, different atomic distortions appear. Specifically,  $R_z$  phase appears first, then  $M_z$  appears at a lower temperature together with  $P_z$ . Small in-plane  $P_x$  and  $R_x$  distortions finally show up at very low temperature and the GS at zero Kelvin corresponds to a  $R_{xz}M_zP_{xz}$  phase.

This first model potentials supports that the system will exhibit consecutive phase transitions ( $R_z$  condensing before  $M_z$  and  $P_z$ ), contrary to what was reported in Ref.[20]. However, this first result needs to be taken with caution and to be further confirmed since, as already highlighted by the Landau model, the temperature behavior strongly depends on the parameters. If, for instance, we redo our Monte-Carlo simulations applying a negative pressure that correct for the typical LDA volume underestimate,  $P_z$  and  $M_z$  now condense at almost the same temperature as  $R_z$ . Also, in this first model, the oxygen interactions were limited to very short range and it should be checked if a better description of these interactions eventually affect the physics of the system.

Although still preliminary, these results attest that the model potentials technique is a very promising tool to explore the lattice dynamics of complex systems in which various instabilities couple together. It also provide the opportunity to investigate exotic phenomena. For instance, in the  $R_{xz}M_zP_{xz}$  phase stable at very low temperature and in which the in-plane and out of plane components of the polarization coexist, we have demonstrated that it is possible to switch the in-plane polarization with an out-of-plane electric field, taking full advantage of the trilinear coupling terms.

# Chapter 4

## Natural and artificial $ABO_3/AO$ superlattices

### 4.1 Introduction

In the previous chapter, we discussed the case of a short-period  $PTO/STO$  (1/1) superlattice, which is specific and still relatively easy to study from first-principles calculations. Now, it would be very interesting also to be able to access the properties of larger-period systems, with different types of interfaces, for which first-principles calculations cannot be handled easily. Going further, it would be particularly useful as well, although even more challenging, to access those properties at finite temperature.

As a natural extension of the previous Chapter, it is very appealing to try facing these challenges by finding a practical way to extend to larger systems the effective-potential scheme applied to  $PTO/STO$  (1/1) superlattices. To that end, our basic strategy, illustrated in Figure 4.1, is to divide large-period superlattices into central layer parts and interface parts and to fit the parameters of both parts separately from first-principles calculations on bulk and short period superlattices.

Of course the separation into central and interface layers is artificial and defined arbitrarily and, in order to check how realistic such a strategy could be, we have to answer the two following and related questions: i) how fast do we recover the bulk behavior when the thickness of central layer becomes large ? and ii), how thick is the interface layer to be considered ?

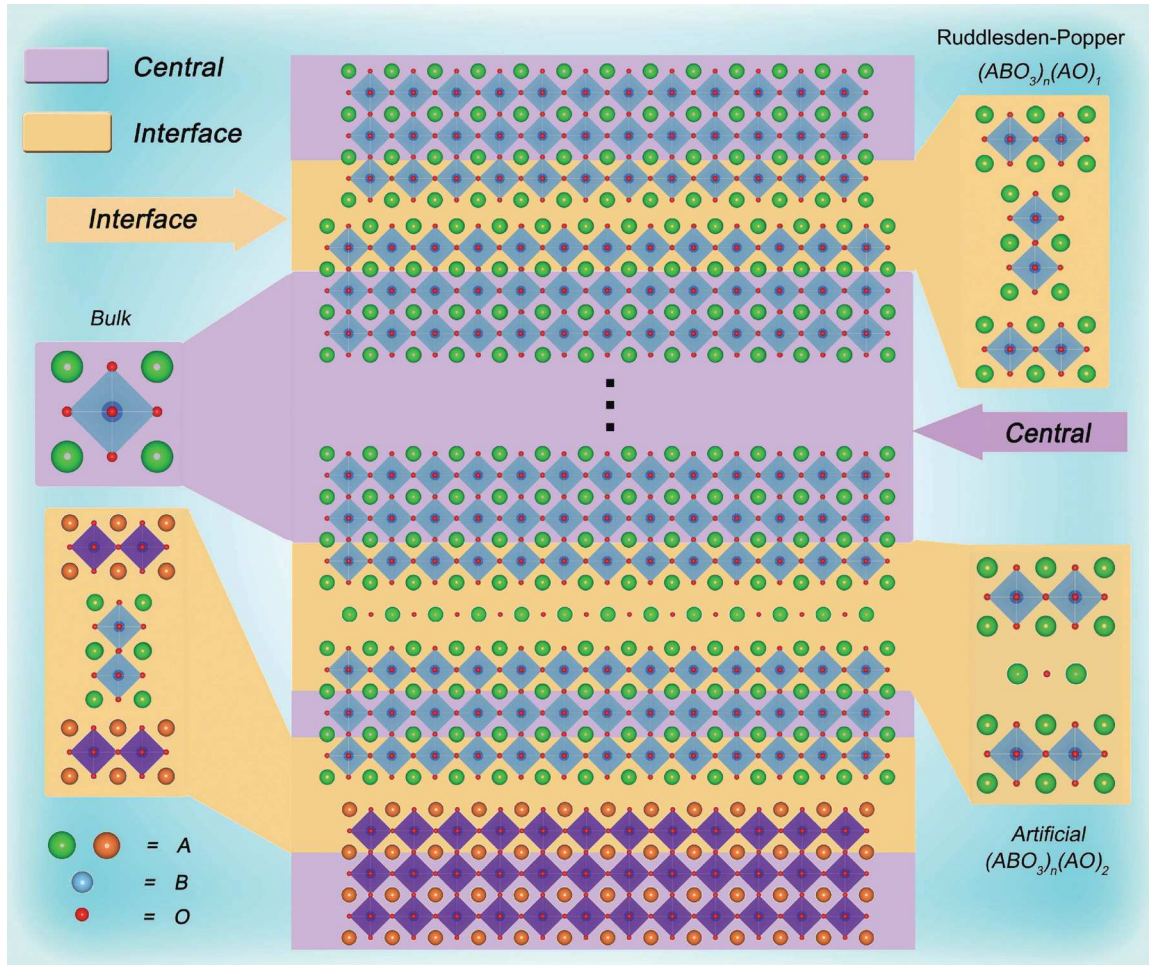


FIGURE 4.1: Motivation: We try to estimate the dynamics of large period superlattices from the knowledge of bulk and short period superlattices. The thick superlattices is divided into two parts, the central layer (purple part) and the interface layer (yellow part). We try to demonstrate that we can use the related quantity of the bulk to approximate the central layer of the thick superlattices, and use the related quantity from the short period superlattices to approximate the interface of the thick ones.

In order to answer these questions, in this chapter, we will consider two types of superlattices, Ruddlesden-Popper  $(ABO_3)_n/(AO)_1$  (*RP*) and so-called artificial  $(ABO_3)_n/(AO)_2$  (*AF*) superlattices, which are shown in Figure 4.2. Both types of superlattice are composed of perovskite blocks separated by a rock-salt type layer. We have chosen two titanate series which differ by the *A* site elements: *Ba* and *Sr*. Our study will mainly focus on the lattice dynamics of these systems including phonon dispersion curves, phonon density of states (*DOS*), the inter-atomic force constants (*IFC*), the Born effective charges, and also the dielectric constant. Beyond this, the relaxed structure of some of these systems will be analyzed. Through our discussion, we will see clearly that the dynamical properties of the superlattices converge very

quickly to the bulk values when going away from the interface region.

## 4.2 System of Interest

To define the cell which is periodically repeated in space, the generic formula  $(ABO_3)_n/(AO)_2$  was used for artificial superlattices ( $AF$ ) while the generic formula  $(ABO_3)_n/(AO)_1$  was used for Ruddlesden-Popper superlattices ( $RP$ ) ( $A=Ba, Sr, Pb$ ,  $B=Ti$ ). Both of them are labelled by  $n$ , where  $n$  is the number of  $ABO_3$  formula units between two interfaces. To establish the notation, we will call the plane parallel to the interface the  $(x,y)$  plane, while the perpendicular direction will be referred to as the  $z$  axis. In  $AF$  superlattices we have two  $AO$  layers inserted after every  $n$  layers of perovskite unit cell. In  $RP$  superlattices we have one  $AO$  layer inserted after every  $n$  layers of perovskite unit cell. According to these notations, the perovskite unit cells are shifted along  $x-y$  direction by  $(1/2, 1/2)$  lattice constant after each  $AO$  interface in  $RP$  superlattices.

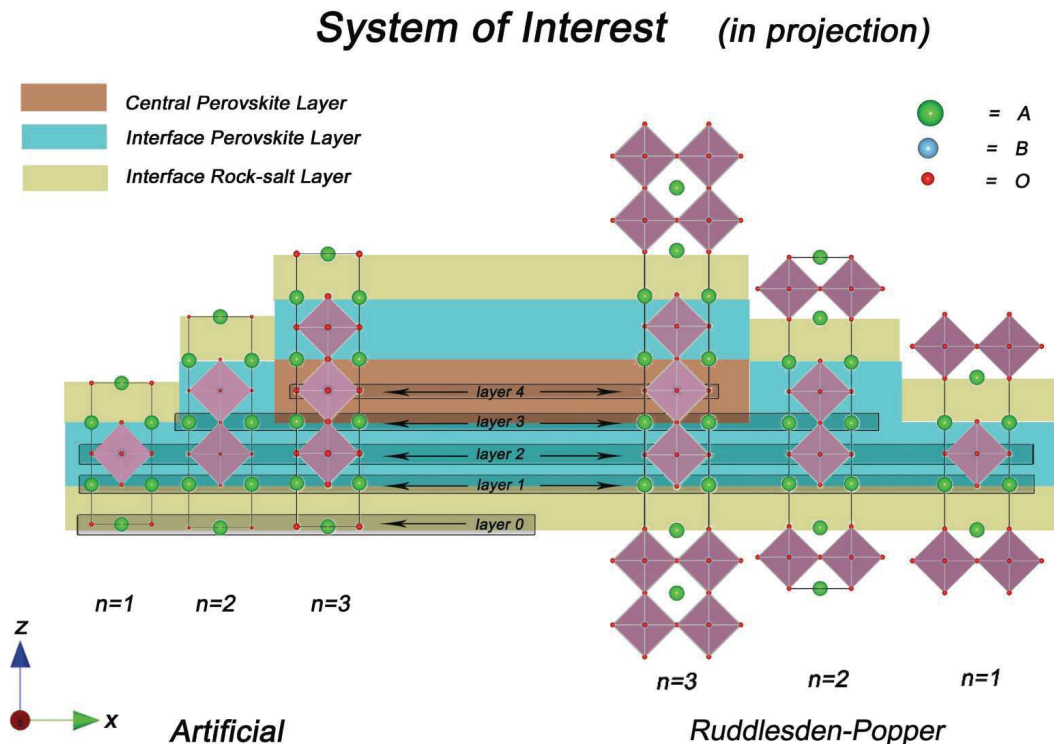


FIGURE 4.2: In the case of  $AF$  (left side) and  $RP$  (right side) superlattices, we label each layer, from  $layer\ 0$  to  $layer\ 4$  ( $layer\ 0$  only exists in  $AF$  series), and define the central perovskite layer (orange part), interface perovskite layer (blue part) and interface rock-salt layer (yellow part).

The labelling of layers ( $AO$  and  $TiO_2$ ) starts from the interface. *Layer 1* is the first  $AO$  layer for the perovskite block. In the  $AF$  structures, there is an additional  $AO$  layer in the interface labelled *layer 0*. As shown in Figure 4.2, *layers 1, 2, 3* are labeled together as interface perovskite layer, *layers 1, 0* are labeled together as interface rock-salt layer, *layers 3, 4* are labeled as central perovskite layer. In this case, *layer 1* is shared by the interface rock-salt layer and the interface perovskite layer, and *layer 3* is shared by interface perovskite layer and the central perovskite layer.

### 4.3 Technical Details of DFT Calculations

First-principles calculations were performed in the framework of density functional theory (DFT) as implemented in the ABINIT package. The generalized gradient approximation of Wu and Cohen (GGA-WC) was used for the exchange-correlation potential. It is well known to be quite accurate in predicting the lattice constants. An energy cutoff of 45 hartree was used for the plane-wave expansions. Optimized norm-conserving pseudopotentials were employed, treating as valence states the  $5s, 5p$  and  $6s$  states of  $Ba$ , the  $4s, 4p$  and  $5s$  states of  $Sr$ , the  $5d, 6s$  and the  $6p$  states of  $Pb$ , the  $3s, 3p, 3d$  and  $4s$  states of  $Ti$  and the  $2s$  and  $2p$  states of  $O$ .

The lattice constants and atomic positions were relaxed while keeping the high-symmetry tetragonal phase of space group  $P4/mmm$  (No.123), and the cubic space group  $Pm-3m$  (No.221) for superlattices and bulk perovskite structures respectively. For the cubic phase of bulk  $ABO_3$ , a  $n$ -layers super-cell  $(ABO_3)_3$  was used in order to compare with the two types of superlattices mentioned above.

### 4.4 Relaxed Reference Structure

We considered  $n$  from 1 to 3  $AF$  and  $RP$  superlattices for relaxation without any epitaxial strain. Relaxed lattice constants are reported in Table 4.1 and compared with the experimental values for cubic  $BaTiO_3$ ,  $SrTiO_3$  and  $PbTiO_3$  from Refs.[140] (in which the lattice constants are reported as 3.996Å for  $BaTiO_3$ , 3.905Å for  $SrTiO_3$  and 3.969Å for  $PbTiO_3$ ). We see that the  $GGA\_WC$  exchange correlation functional is efficient for lattice constants, predicting cell parameters within 1% error of the

experimental value. It is observed that by increasing  $n$  the in-plane lattice constant converges to the cubic perovskite value. In the *BTO* system, the in-plane lattice constant of *RP* superlattices is larger than the cubic perovskite value and decreases when  $n$  increases but in other the cases, including *AF BTO*, *AF* and *RP* of *STO* and *PTO*, the in-plane lattice constant is smaller than the cubic value and gets larger when  $n$  is increasing. In previous works[142], the in-plane lattice constant of  $Sr_2TiO_4$  is calculated as 3.822Å within DFT calculations, i.e. slightly underestimated due to the *LDA* approximation used. For  $Pb_2TiO_4$ , the in-plane lattice constant (3.857Å) and out-of plane lattice constant (12.70Å) were calculated from DFT-LDA in Refs.[36]. These value are in good agreement with our results, although underestimating the lattice constants as expected within the *LDA*.

Tables 4.2 and 4.3 show the atomic rumpling, defined as  $R_{aver}=(z_{cat}-z_O)/2$ , along  $z$  axis due to relaxation, and corresponding *Ti-O* bond lengths. Before analyzing the rumpling in details, we need to label each *Ti-O* bond and define the average plane of each layer. As shown in Figure 4.3, the labeling starts from the interface: *Ti-O* bonds are labeled as bond 1, 2 and 3 from the interface to the central of perovskite block. As shown in Figure 4.3, we define the average plane as the average of the cation and the oxygen  $z$  coordinate( $z_{aver}=(z_{cat}+z_O)/2$ ). Then we can define the thicknesses of the interface perovskite layer as  $c_i=|z_{aver1}-z_{aver2}|$ , and of the central perovskite layer as  $c_c=|z_{aver2'}-z_{aver2}|$ . As shown in Figure 4.3  $z_{averj}$  and  $z_{averj'}$  refer to the  $z$  atomic coordinates in *layer j* and its mirror layer. The values of  $c_i$  and  $c_c$  for different  $n$  values are reported in Table 4.1.

The symmetry along  $z$  direction is broken by the interface relaxation, since *Ti-O* bond 1 is significantly smaller than bond 2, while they have same length in bulk perovskite. The rumpling can be as large as 0.105Å (in *STO RP n=3*) in *layer 1* and gets rapidly smaller in the layers farther away from the interface (in *layer 2*, the amplitude is smaller than 0.02Å). This is in agreement with rumpling data reported in previous works [37] (0.232Å for *layer 1*, 0.041Å for *layer 2* and 0.036Å for *layer 3*).

From Table 4.3, we can see that the *Ti* atom in the first neighbor perovskite layer of interface is off-centred along  $z$ . Comparing with the central layer in the case  $n=3$ , the interface layer is no longer cubic-like since there is a significant rumpling in layer 1 with an off centred *Ti* atom in layer 2. In layer 2, the *Ti* atom moves towards the interface, which induces two different *Ti-O* bond lengths. The bond 1 is about 2.5% shorter than bond 2 in the superlattices of *BTO*, *STO* and *PTO* system. We also

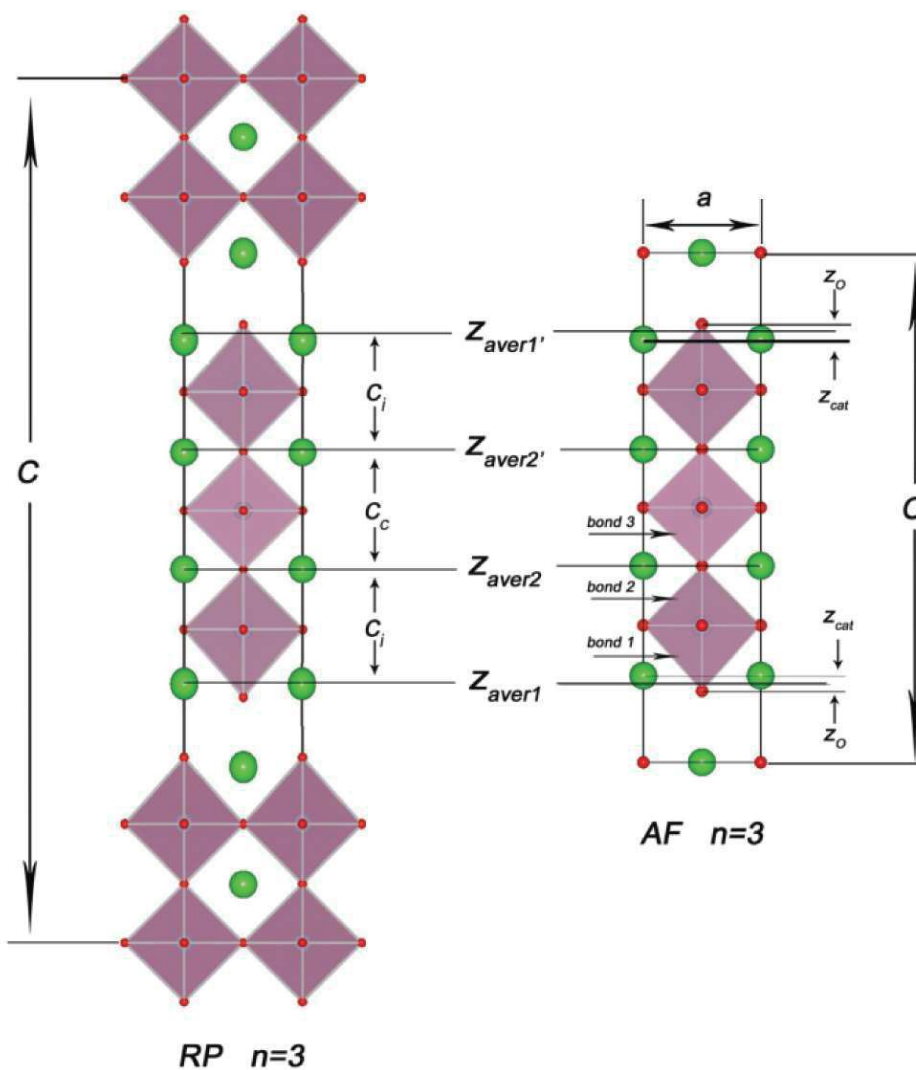


FIGURE 4.3: The in-plane lattice constant ( $a$ ) and out-of-plane lattice ( $c$ ) are shown here. We label each bond (from bond 1 to bond 3) and define the average plane for each layer. The thickness of central perovskite layer ( $c_c$ ) and the one of interface perovskite layer ( $c_i$ ) are defined as well.

notice that when  $n=3$ , the length of bond 3 is close to the average value of bond 1 and bond 2 in *BTO* and *PTO* superlattices, while it is close to the length of bond 1 in *STO*. This means that, in *STO*, the first neighbor *O-Ti-O* chain of the interface is compressed while it is not in *BTO* and *PTO*.

TABLE 4.1: In-plane lattice constant ( $a$ ), out-of-plane lattice constant ( $c$ ), thickness of interface perovskite layer ( $c_i$ ) and the thickness of central perovskite layer ( $c_c$ ) under zero epitaxial strain of  $Ba, Sr$  and  $Pb$  based superlattices for  $AF$  and  $RP$  types (in Å).

	n=1			n=2			n=3			Bulk cubic	
	a	c	$c_i$	a	c	$c_i$	a	c	$c_i$		$c_c$
BTO											
$AF$	3.978	9.361	3.919	3.984	13.344	3.944	3.986	17.329	3.948	3.968	3.987
$RP$	3.997	13.257	3.897	3.996	21.230	3.938	3.993	29.206	3.931	3.980	3.987
STO											
$AF$	3.838	8.850	3.870	3.868	12.733	3.874	3.880	16.632	3.873	3.896	3.905
$RP$	3.886	12.526	3.809	3.900	20.275	3.829	3.903	28.072	3.836	3.898	3.905
PTO											
$AF$	3.852	9.030	3.969	3.888	12.938	3.946	3.901	16.860	3.948	3.948	3.933
$RP$	3.896	12.856	3.918	3.917	20.690	3.907	3.924	28.549	3.914	3.914	3.933

TABLE 4.2: Rumpling in interface perovskite layers, which is defined as the displacement along  $z$  between cations and oxygen atoms ( $R_{aver} = (z_{cat} - z_O)/2$ ), of  $Ba, Sr$  and  $Pb$  based superlattices for  $AF$  and  $RP$  types (in Å).

		AF			RP		
		n=1	n=2	n=3	n=1	n=2	n=3
		BTO	layer 1	0.031	0.036	0.038	0.032
	layer 2	—	0.006	0.008	—	0.007	0.009
	layer 3	—	—	0.006	—	—	0.000
STO	layer 1	0.065	0.076	0.078	0.085	0.101	0.105
	layer 2	—	0.011	0.013	—	0.016	0.018
	layer 3	—	—	0.011	—	—	0.001
PTO	layer 1	0.025	0.034	0.038	0.041	0.053	0.059
	layer 2	—	0.003	0.008	—	0.010	0.014
	layer 3	—	—	0.006	—	—	0.013

## 4.5 Phonon Dispersion Curves

In this part, Density Functional Perturbation Theory ( $DFPT$ ) was used to obtain the phonon dispersion curves of the two types of superlattices, and of the bulk simple cubic phase as well. High symmetry points of the Brillouin zone ( $BZ$ ) are labeled as

TABLE 4.3:  $Ti-O$  bond lengths of  $Ba, Sr$  and  $Pb$  based superlattices for  $AF$  and  $RP$  types (in Å). Each bond is defined in figure 4.3.

		AF			RP		
		n=1	n=2	n=3	n=1	n=2	n=3
BTO	bond 1	1.99	1.96	1.95	1.98	1.95	1.94
	bond 2	—	2.02	2.03	—	2.02	2.03
	bond 3	—	—	1.99	—	—	1.99
STO	bond 1	2.00	1.96	1.95	1.99	1.95	1.95
	bond 2	—	1.99	1.99	—	1.98	1.99
	bond 3	—	—	1.96	—	—	1.95
PTO	bond 1	2.01	1.98	1.97	2.00	1.96	1.95
	bond 2	—	2.00	2.01	—	2.00	2.01
	bond 3	—	—	1.98	—	—	1.97

: $\Gamma(0, 0, 0)$   $X(1/2, 0, 0)$ ,  $M(1/2, 1/2, 0)$ ,  $R(1/2, 1/2, 1/2)$ ,  $Z(0, 0, 1/2)$  and  $W(0, 1/2, 1/2)$  in units of the reciprocal lattice unit vectors.

In Figure 4.4-Figure 4.7, we report the phonon dispersion curves and the zero-frequency isosurface of the lowest unstable phonon branch for cubic  $BaTiO_3$ ,  $SrTiO_3$  and  $PbTiO_3$ . Our results are comparable with the result from Refs.[90] and [143]. The phonon dispersion curves of  $BTO$ ,  $STO$  and  $PTO$  systems, both  $AF$  and  $RP$  types, are shown here as well. Imaginary phonon frequencies of unstable modes are represented as negative values. Our analysis will mainly trace these phonon modes in the Brillouin zone, since they are relevant for phase transitions. The lowest phonon frequency at some selected points of each structure is reported in Table 4.4.

### 4.5.1 Barium Compounds

As well known [144], there are three degenerated unstable transverse optic modes at  $\Gamma$  point for cubic  $BaTiO_3$ . Examination of the associated eigenvectors reveals that they correspond to displacements of the atoms  $Ti$  toward the  $O$  atoms along  $x$ ,  $y$  and  $z$  directions, which drives the ferroelectric phase transition. The instability is visualized in Figure 4.4 where the zero frequency isosurface of the lowest unstable phonon modes is plotted out. The unstable region consists in 3 orthogonal sheets region including  $\Gamma$ . The planar (2D) character of the ferroelectric instability in reciprocal space is associated to a chain-like character in real space. Since the width of the unstable

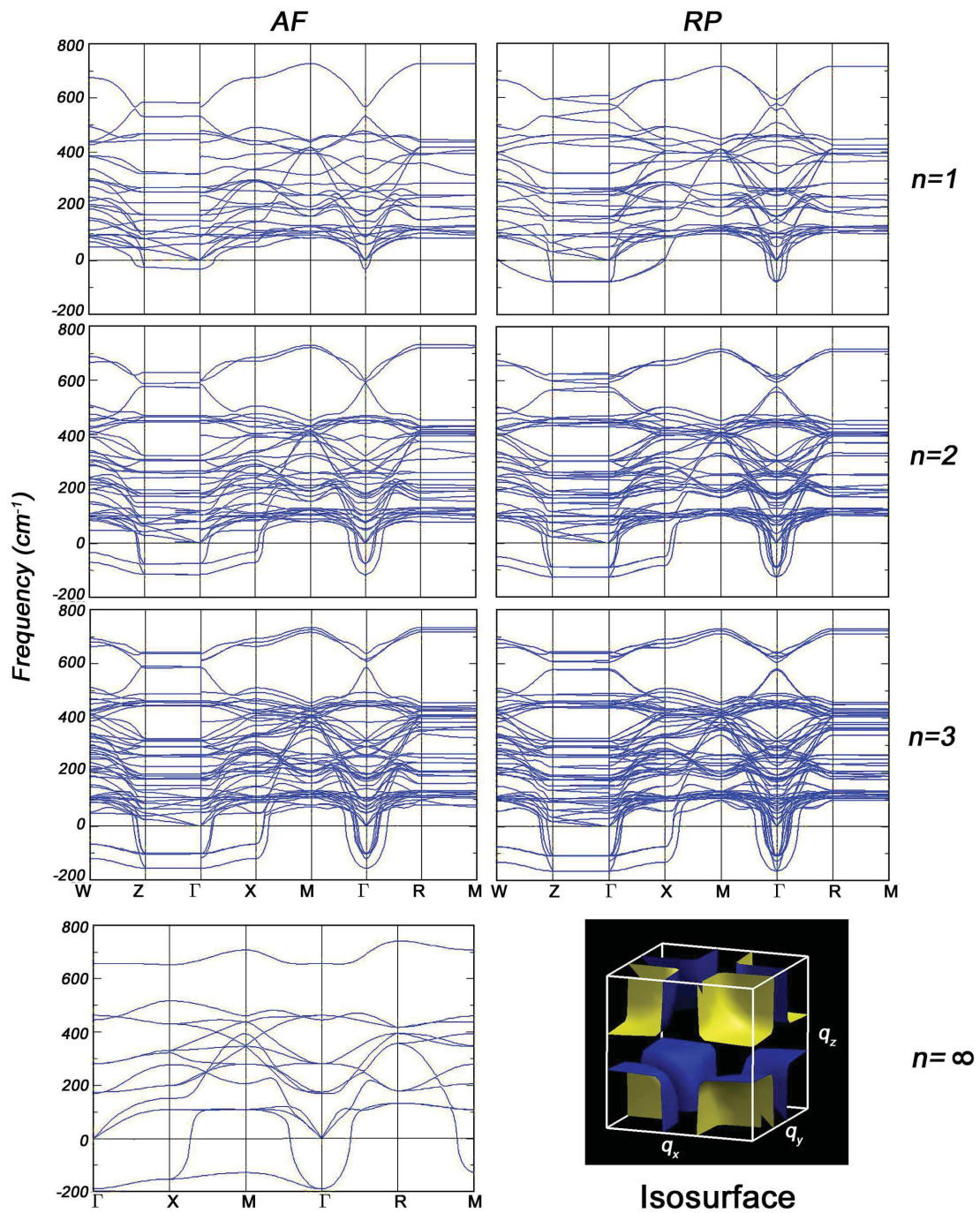


FIGURE 4.4: Phonon dispersion curves of bulk cubic  $BaTiO_3$  ( $n=\infty$ ) and  $Ba$  based superlattices for  $AF$  and  $RP$  types,  $n$  from 1 to 3. The phonon frequencies are presented in units of  $cm^{-1}$ . The imaginary values are reported as negative ones. The zero frequency isosurface of bulk cubic  $BaTiO_3$  is plotted at the right bottom corner.

planar region in reciprocal space is about  $1/4$  of the  $BZ$ , we can estimate that the correlation length of  $Ti$  motion required to produce the ferroelectric instability is of

about 4 unit cells.

Similar unstable polar modes appear in *AF* and *RP* superlattices already for  $n=1$  but the amplitude is weakened significantly compared to bulk, and the motion of the atoms is restrained in the  $x$ - $y$  plane. This mode remains unstable along  $\Gamma$ - $Z$  line with very little dispersion. By increasing the value of  $n$ , another unstable mode appears for  $n=2$  and 3 which corresponds to anti-polar atomic motions in the  $x$ - $y$  plane. This anti-polar mode has the second lowest frequency and the polar mode remains the lowest one. When  $n \geq 2$ , these two modes remain unstable not only at  $\Gamma$  point but also along the  $W$ - $Z$ - $\Gamma$ - $X$  lines. As clearly shown in Table 4.4, the frequency of the unstable polar mode converges to the perovskite value when  $n$  increases.

In contrast to the case of bulk *BaTiO<sub>3</sub>*, there is no unstable mode with atomic motion along  $z$  in the superlattice. On the one hand, the interface layer might act as a dead layer which enables to preserve the depolarizing field killing the ferroelectric instability. On the other hand, a correlation length of about 4 Ti atoms is needed to produce polar and anti-polar instability and this threshold is not reached at  $n=3$ . More discussion on the finite size effect and the “ferroelectric correlation volume“ can be found in previous works [145, 146].

### 4.5.2 *Strontium Compounds*

In cubic *SrTiO<sub>3</sub>*, two kinds of phonon instabilities appear, one at the  $\Gamma(0, 0, 0)$  point and the other at the  $R(1/2, 1/2, 1/2)$  and  $M(1/2, 1/2, 0)$  points. At  $\Gamma$  point, there are three unstable phonon modes, which have the same frequency and correspond to a polar motion along  $x$ ,  $y$  and  $z$  directions. These unstable polar modes stiffen up quickly away from the  $BZ$  center. The unstable phonon modes at the  $R$  point have the lowest frequencies and drive the antiferro-distortive phase transition. They correspond to the rotation of the oxygen octahedra along  $x$ ,  $y$  and  $z$  axis. One of them, which corresponds to a rotation along  $z$  axis, remains unstable along the  $R$ - $M$  line with significant dispersion. The other two stabilize quickly away from the  $R$  point.

In *STO* systems, as observed from Figure 4.5, the phonon dispersion curves for *AF* and *RP* superlattices are similar. Both do not have any unstable phonon mode for  $n=1$ , and an instability appears at  $n=2$  in *AF* and at  $n=3$  in *RP* superlattices. As seen in Table 4.4, with increasing  $n$  value, the unstable modes at  $M$  and  $R$  points

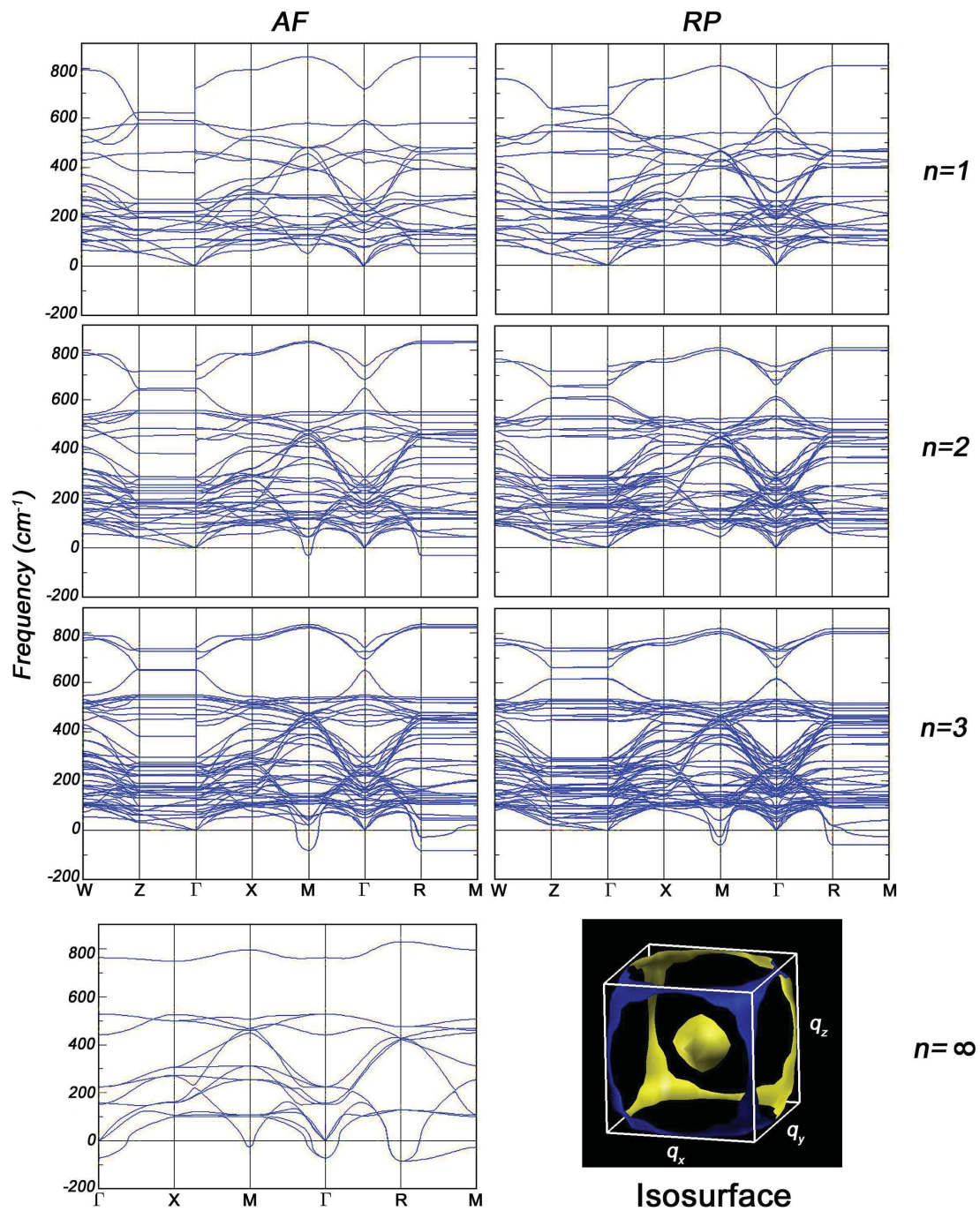


FIGURE 4.5: Phonon dispersion curves of bulk cubic  $SrTiO_3$  ( $n=\infty$ ) and  $Sr$  based superlattices for  $AF$  and  $RP$  types,  $n$  from 1 to 3. The phonon frequency are in units of  $cm^{-1}$ . The imaginary values are reported as negative ones. The zero frequency isosurface of bulk cubic  $SrTiO_3$  is plotted at the right bottom corner.

soften and their frequencies converge to the values for cubic  $SrTiO_3$ . Examination of the eigenvectors reveals that these latter modes correspond to oxygen octahedra rotations along the  $z$  axis. When  $n \geq 2$ , two consecutive octahedra along  $z$  rotate in

opposite directions (out-of-phase mode  $AFD_{zo}$ ). From the zero frequency isosurface of cubic  $SrTiO_3$ , showing narrow cylinders along the  $BZ$  edges, we can roughly conclude that, in order to build an instability based on these rotation modes, we need correlation of oxygen motions in the plane perpendicular to the rotation axis. Our superlattice systems exhibit no unstable rotation modes along  $x$  or  $y$ . Since these rotations would involve the oxygen in *layer 1*, where the octahedra is strongly distorted, this  $AFD_{xyo}$  mode can not appear for  $n=3$ . Only the unstable rotation mode along  $z$  can exist.

The reason why the unstable polar mode does not appear in  $AF$  and  $RP$  superlattices can be traced from the zero frequency isosurface of cubic  $SrTiO_3$ . As discussed above, Figure 4.5 implies that, to build ferroelectric instability in  $STO$ , the shortest chain length required is around 7~8 (or more) perovskite unit cells in the directions not only parallel but also perpendicular to the polarization direction. In our  $AF$  and  $RP$  superlattices, the value of  $n$  is still far from the required chain length. As it is discussed in Ref. [37], artificially suppressing the rumpling or applying strain may tune the coherence length and induce the ferroelectric instability in  $RP$  superlattices of the  $STO$  system.

TABLE 4.4: Phonon frequency of the lowest unstable mode (in  $cm^{-1}$ ) of  $Ba, Sr$  and  $Pb$  based superlattices for  $AF$  and  $RP$  types.

		BTO		STO		PTO	
		X	$\Gamma$	R	$\Gamma$	R	$\Gamma$
cubic		-151.96	-188.43	-84.74	-70.12	-79.50	-151.40
	n=3	-119.46	-155.05	-80.32	—	-202.79	-187.05
AF	n=2	-8.70	-144.45	-31.06	—	-207.68	-185.52
	n=1	49.12	-32.41	52.52	—	-206.32	-180.85
	n=3	-131.41	-163.81	-58.74	—	-91.52	-141.60
RP	n=2	-83.02	-125.91	80.87	—	-89.64	-141.23
	n=1	5.94	-77.90	123.20	—	-97.71	-144.17

### 4.5.3 Lead compounds

In cubic  $PbTiO_3$ , the phonon behavior has similarities with both cubic  $BaTiO_3$  and  $SrTiO_3$ . As in the latter, the unstable rotation mode, which corresponds to the oxygen octahedra rotations along  $x, y, z$  axis, appears at  $M, R$  points and remains along the  $R-M$  lines with little dispersion and is more dispersive along the  $R-\Gamma$

and the  $M$ - $X$  line. The unstable polar mode that appears at  $\Gamma$  point and drives a ferroelectric phase transition, has the lowest phonon frequency as in cubic  $BaTiO_3$ .

The phonon dispersion curves of  $PTO$   $AF$  and  $RP$  superlattices are reported in Figure 4.6, from which we can see large differences compared to  $BTO$  and  $STO$  superlattices. The frequency of the lowest unstable phonon modes do not converge to the cubic value but keep relatively the same amplitude, which is shown in Table 4.4 as well. In agreement with Ref. [36]  $Pb$  based  $RP$  structures, when  $n=2$ , display a ferroelectric instability. However, the frequency of this mode is not comparable to Ref. [36] ( $96i\text{ cm}^{-1}$ ). In our calculations, we found more than one unstable mode at  $\Gamma$  as are reported in the  $LDA$  case. The different lattice constants we used might be the origin of this discrepancy, since the ferroelectric instability is very sensitive to the lattice volume. It is needed to point out that in the  $AF$  case, the eigenvectors of the lowest unstable phonon mode at  $\Gamma$  point correspond to an in-plane anti-polar motion of atoms, in which the direction of polarization in *layer 0* is opposite to the one in perovskite slab. The unstable ferroelectric polar mode along  $z$  direction ( $FE_z$ ) appears at the  $BZ$  center already from  $n=1$  in  $AF$  superlattices. This  $FE_z$  mode exists in  $RP$  superlattices but only from  $n=3$ . We report the frequencies of this  $FE_z$  mode in Table 4.5 in which we can see that the  $FE_z$  instability is weaker than the one in  $x$ - $y$  plane. The frequency converges to the perovskite value when  $n$  increases.

It is worth pointing out that, by checking the eigenvectors in  $AF$  superlattices of  $PTO$ , *layer 0* shows the largest values for polar motions. In Figure 4.7, we plot out the amplitude of the polar motions for each layer, in the case of  $n=2$  for  $PTO$  in comparison with the  $BTO$  system. Here, the amplitude of the polar motion is defined as

$$p_{am} = \sum_{ij} Z_{ij}^* \eta_{ij} \quad (4.1)$$

where the  $\eta_{ij}$  is the eigenvector component of atom  $i$  along direction  $j$  and  $Z_{ij}^*$  is the Born effective charge of atom  $i$  along the direction  $j$ . It is clearly shown in Figure 4.7, in the case of  $AF$   $PTO$  superlattices, that the  $p_{am}$  in *layer 0* is significantly larger than in  $RP$   $PTO$  and  $BTO$  systems. Here, mode 1 refers to the lowest unstable phonon mode at  $\Gamma$  and mode 2 refers to the second lowest one. Thus the enhanced ferroelectric phonon instability in  $AF$   $PTO$  corresponds to the contribution of *layer*

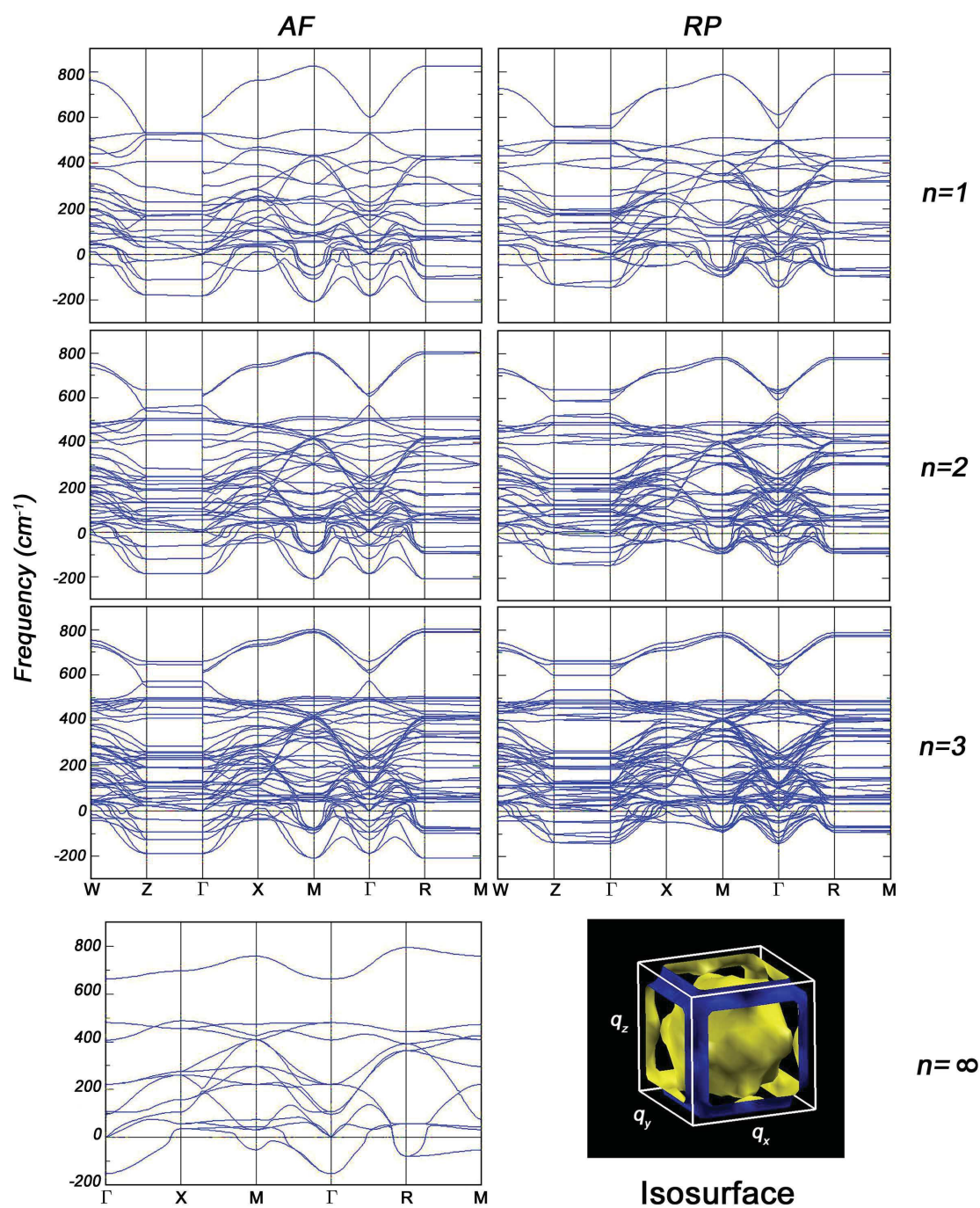


FIGURE 4.6: Phonon dispersion curves of bulk cubic  $PbTiO_3$  ( $n=\infty$ ) and  $Pb$  based superlattices for  $AF$  and  $RP$  types,  $n$  from 1 to 3. The phonon frequency are in the units of  $cm^{-1}$ . The imaginary values are reported as negative ones. The zero frequency isosurface of bulk cubic  $PbTiO_3$  is plotted at the right bottom corner.

$0$  ( $PbO$  layer). In this  $Pb$  based  $AF$  and  $RP$  superlattices, the  $PbO$  interface plays an important role in tuning the ferroelectric instability.

TABLE 4.5: Phonon frequency of the  $FE_z$  and  $AFD_{zo}$  mode in  $PTO(cm^{-1})$ 

		$FE_z$	$AFD_{zo}$
cubic		-151.40	-79.50
AF	n=3	-69.12	-97.73
	n=2	-52.56	-95.21
	n=1	-32.59	-107.12
RP	n=3	-22.12	-91.52
	n=2	—	-80.45
	n=1	—	-69.69

Furthermore, as observed from figure 4.6, the phonon instabilities of  $AF$  superlattices are not similar to the one of  $RP$ : In the case of  $RP$ , the unstable phonon mode with the lowest frequency is at  $\Gamma$  point while in  $AF$  it is found at  $R$  points.

There are two main unstable anti-ferrodistortive rotation modes at the  $R$  point that expand to  $M$  point with little dispersion in  $AF$  and  $RP$  structure. The first one corresponds to the rotation of octahedra along  $z$ , which is an out-of-phase mode ( $AFD_{zo}$ ). The other one corresponds to the rotation of octahedra along  $x$  or  $y$  plus a polar motion along its rotation axis, which can be treated as the combination of a ferroelectric mode and an anti-ferrodistortive mode ( $FE_x+AFD_{xo}$ ). In  $AF$  superlattices, the ( $FE_x+AFD_{xo}$ ) mode has the lowest phonon frequency and this does not change much when we increase the value of  $n$ . In Table 4.4 and Table 4.5, it is clearly shown that the instability amplitude of the ( $AFD_{zo}$ ) mode is significantly smaller than the one of the ( $FE_x+AFD_{xo}$ ) mode. In addition, the amplitude of the ( $AFD_{zo}$ ) mode does not converge to the perovskite value, and keeps its frequency value close to  $100i\text{ cm}^{-1}$ . In  $RP$  superlattices, as mentioned before, the lowest unstable phonon mode appears at the  $BZ$  center. At the  $R$  point, the ( $FE_x+AFD_{xo}$ ) mode is less soft than it is in  $AF$  structure and its frequency does not change when  $n$  increases. Unlike in the  $AF$  structure, the ( $AFD_{zo}$ ) mode in  $RP$  structure keeps softening when we increase the value of  $n$ , as reported in Table 4.5.

The phonon behavior in  $PTO$  superlattices,  $AF$  and  $RP$ , is more complex than it is in  $BTO$  and  $STO$  cases. Due to the contribution of the very polarizable  $Pb^{2+}$ , a different dynamic behavior appears. New phonon instabilities emerge,  $FE_z$  and ( $FE_x+AFD_{xo}$ ), in  $Pb$  based systems.

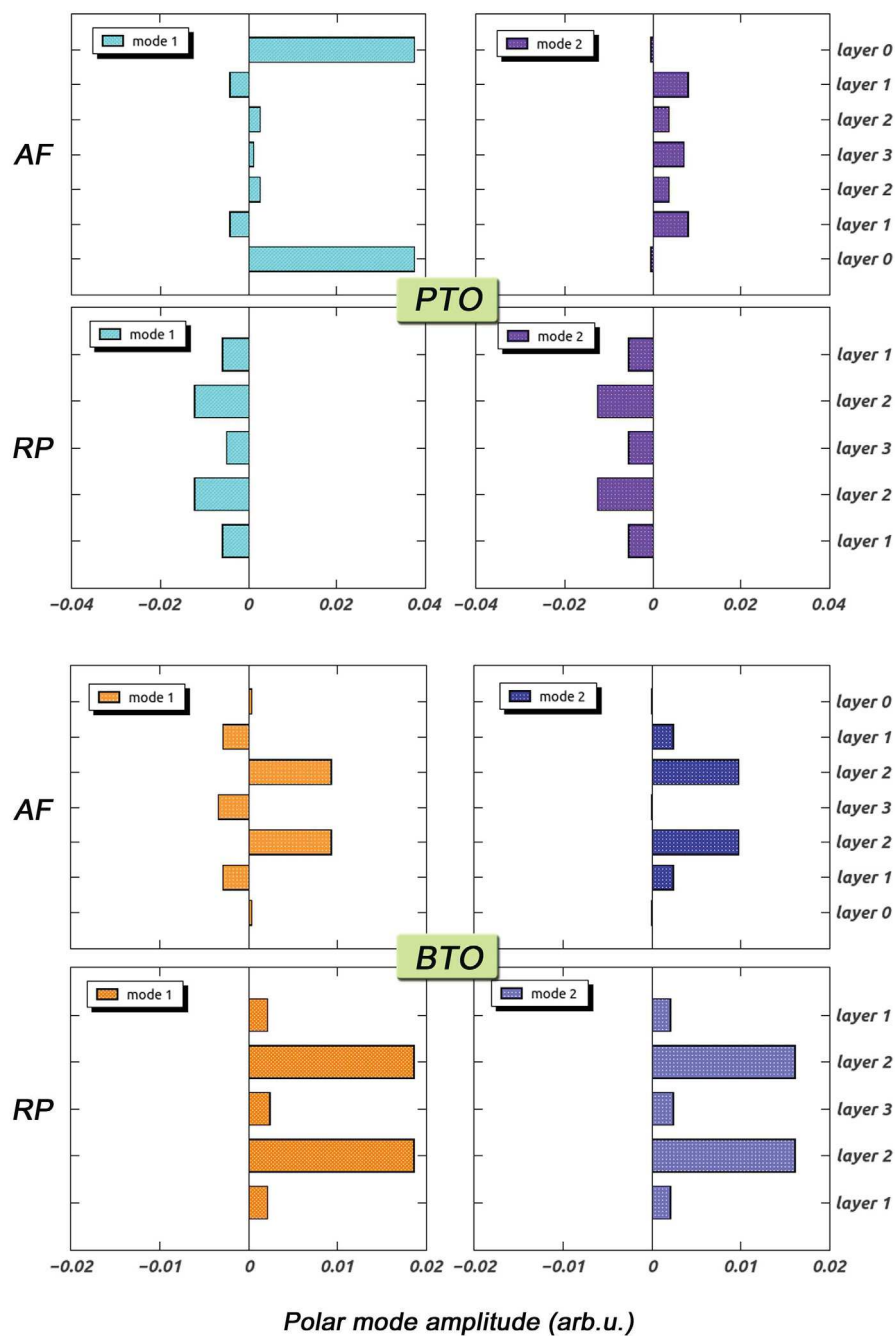


FIGURE 4.7: Amplitude of unstable polar phonon motion in the arbitrary units. Here, mode 1 refers the lowest unstable phonon mode and mode 2 refers the second lowest one. The data are selected from  $Pb$  and  $Ba$  based superlattices for  $n=2$ .

## 4.6 Phonon Density of States

In order to study the phonon contribution from each layer, we here report the phonon density of states ( $DOS$ ) of  $AF$  and  $RP$  superlattices in the case of  $n=3$ , and the phonon  $DOS$  of bulk cubic system. For the superlattices phonon  $DOS$ , we separate the contributions of the central perovskite layer and of interface perovskite layers (which are defined in Figure 4.2), then compare them with the  $DOS$  of bulk cubic perovskite. The results are shown in Figure 4.8, 4.9, 4.10 and 4.11. The region of negative frequencies are zoomed in the insets.

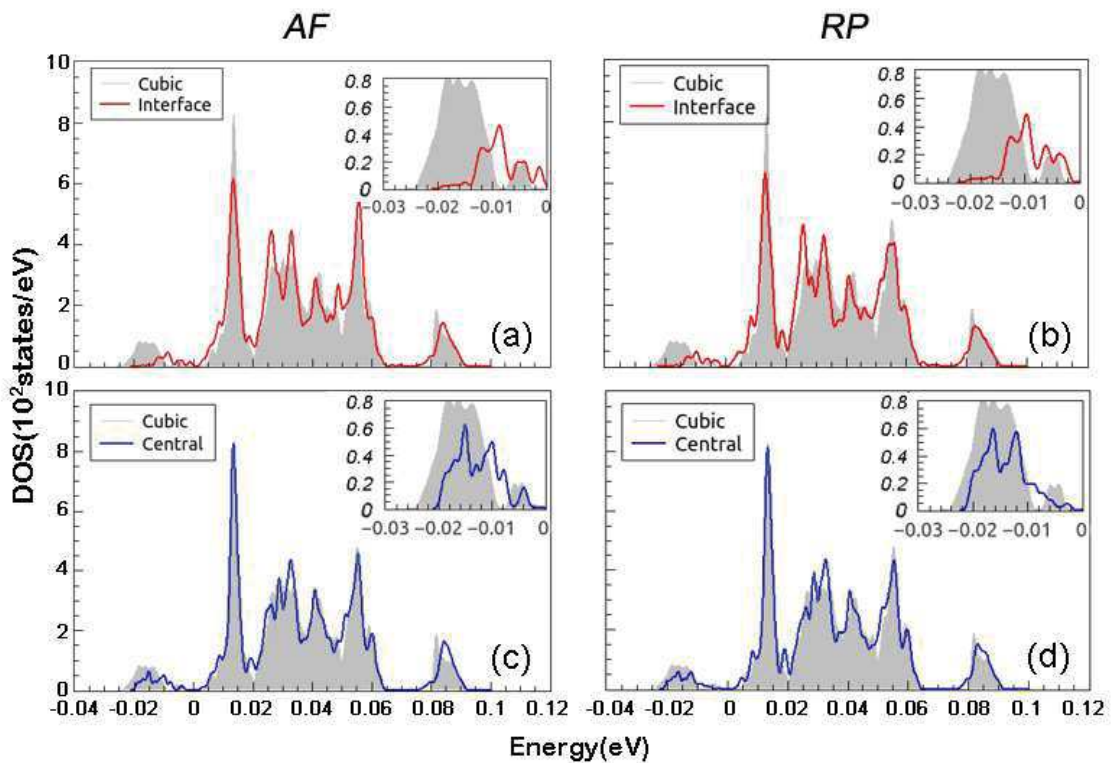


FIGURE 4.8: Phonon density of states ( $DOS$ ) of  $Ba$  based superlattices, in the case of  $n=3$  for  $AF$  and  $RP$  types. The region of imaginary frequencies is zoomed in insets. The gray color part refers the phonon  $DOS$  of the bulk cubic  $BaTiO_3$ , the red line indicates the phonon  $DOS$  contribution of the interface perovskite layer in superlattices while the blue line indicates the phonon  $DOS$  contribution of the central perovskite layer in superlattices

In  $BTO$  superlattices, it is clearly seen in Figure 4.8 that the phonon  $DOS$  of the central perovskite layer reproduces the bulk  $DOS$  better than the interface perovskite layer, both in  $AF$  and  $RP$  structures. In the positive energy region of bulk  $DOS$ ,

there is a peak between  $0\text{ eV}$  and  $0.02\text{ eV}$  which mainly corresponds to the contribution of  $Ba$  atoms. The  $DOS$  of interface perovskite layer does not fully recover this peak (i.e. same energy position but lower magnitude). In the region between  $0.05\text{ eV}$  and  $0.06\text{ eV}$ , there is a peak which originates from the  $TiO_2$  layer. Both the interface and the central perovskite layer recover this peak nicely in energy and magnitude. In the negative energy region, the peak position of the interface perovskite layer is shifted toward higher energies compared with the bulk cubic  $DOS$ , while the central perovskite layer  $DOS$  agrees better with the bulk. This confirms that i) the ferroelectric instability of cubic  $BaTiO_3$  is weakened in  $AF$  and  $RP$  superlattices for  $n=3$ , ii) the central perovskite layer provides the main contribution to the ferroelectric instability, which is suppressed in the interface perovskite layer.

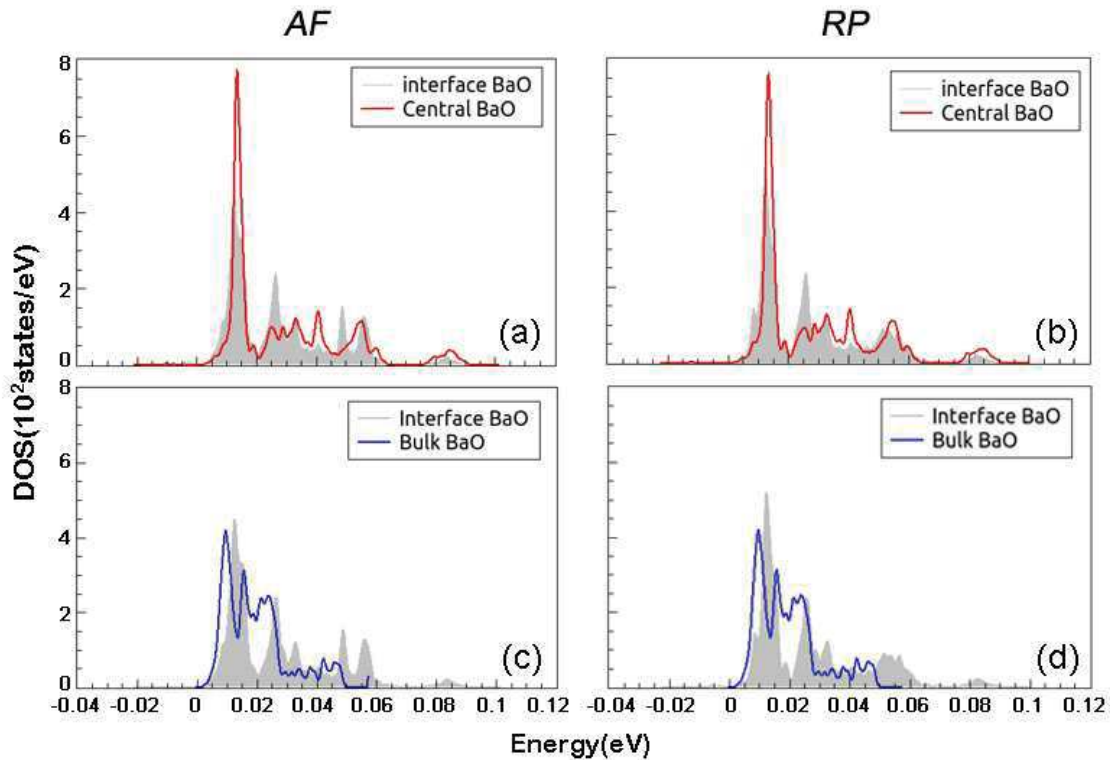


FIGURE 4.9: Phonon density of states ( $DOS$ ) of  $BaO$  layer, in the case of  $n=3$  for  $AF$  and  $RP$  types superlattices. The gray color part refers the phonon  $DOS$  of interface perovskite layer in superlattices, the red line indicates the phonon  $DOS$  contribution of the  $BaO$  layer in central perovskite layer in superlattices while the blue line indicates the phonon  $DOS$  contribution of the bulk rock-salt  $BaO$ .

The phonon  $DOS$  for the  $BaO$  layer at the interface and central region are reported as well. Comparing with the phonon  $BaO$   $DOS$  for bulk, we can see from Figure 4.9 that the  $BaO$  layer does not contribute to the unstable modes in the superlattice, which

confirms that the ferroelectric instability mainly originates from the  $Ti-O$  chains in  $AF$  and  $RP$  superlattices of  $BTO$ . By looking at the position, the magnitude and the width of the  $DOS$  peak, it is obvious that the dynamic behavior of the  $BaO$  layer is similar at the interface and at the center of the perovskite layer. It is however different in bulk  $BaO$ .

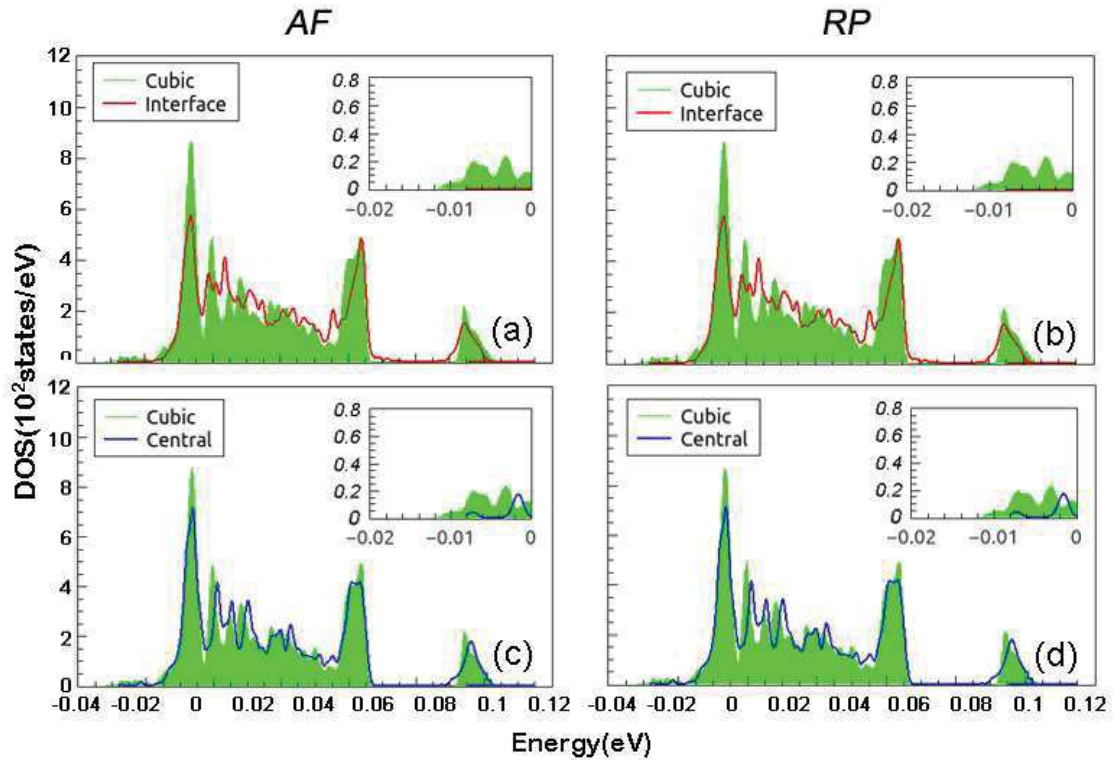


FIGURE 4.10: Phonon density of states ( $DOS$ ) of  $Sr$  based superlattices, in the case of  $n=3$  for  $AF$  and  $RP$  types. The region of imaginary frequencies is zoomed in insets. The green color part refers the phonon  $DOS$  of the bulk cubic  $SrTiO_3$ , the red line indicates the phonon  $DOS$  contribution of the interface perovskite layer in superlattices while the blue line indicates the phonon  $DOS$  contribution of the central perovskite layer in superlattices.

The case of  $STO$  is similar with  $BTO$  in the positive energy region of phonon  $DOS$ . Figure 4.10 shows a peak of large magnitude between 0 and 0.02 eV, which corresponds to the contribution of  $Sr$  atoms mainly from the central perovskite layer. Around 0.06 eV, there is a peak originating from the  $TiO_2$  layer, also from the central perovskite layer. In the negative energy region, the phonon  $DOS$  of cubic  $SrTiO_3$  shows two peaks: the one with lower energy corresponds to the unstable rotation mode and the other one corresponds to the ferroelectric instability. There is no significant contribution from the interface perovskite layer. In the phonon  $DOS$  of

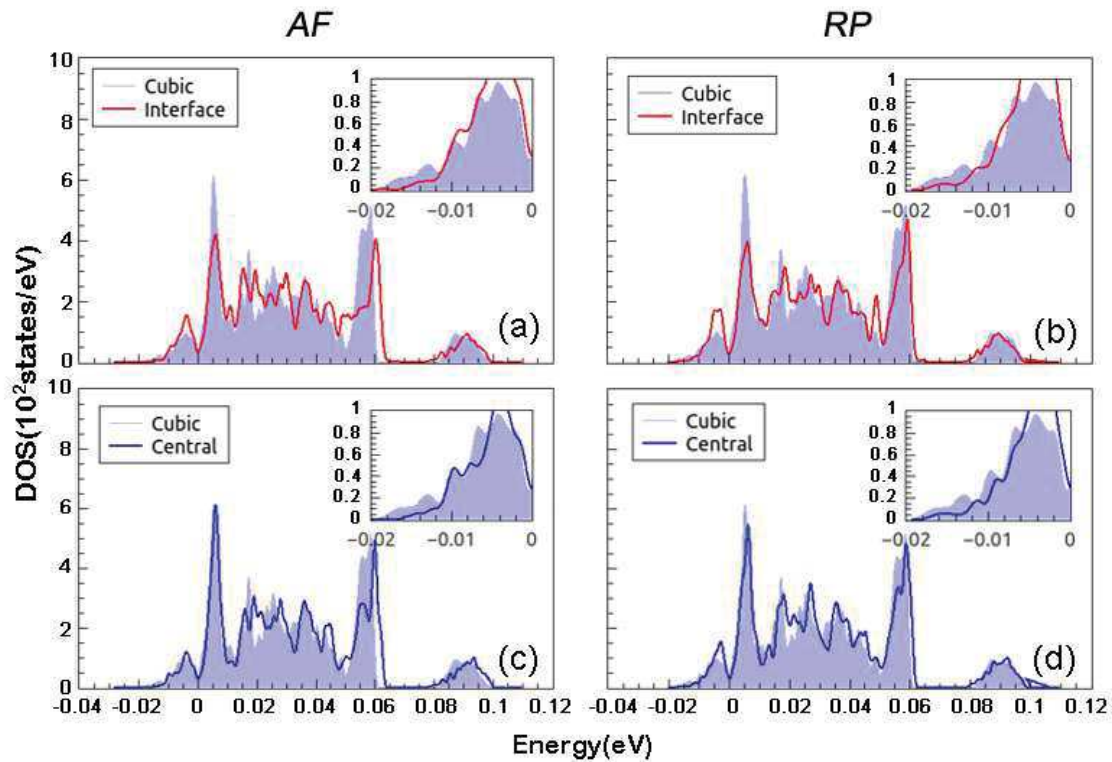


FIGURE 4.11: Phonon density of states ( $DOS$ ) of  $Pb$  based superlattices, in the case of  $n=3$  for  $AF$  and  $RP$  types. The region of imaginary frequencies is zoomed in insets. The green color part refers the phonon  $DOS$  of the bulk cubic  $PbTiO_3$ , the red line indicates the phonon  $DOS$  contribution of the interface perovskite layer in superlattices while the blue line indicates the phonon  $DOS$  contribution of the central perovskite layer in superlattices

central perovskite layer, only one peak appears in the negative energy region, which corresponds to the unstable rotation modes. This peak is shifted toward higher energies compared with the one in cubic  $SrTiO_3$ , and it is confirmed that the anti-ferro distortion instability is suppressed in the interface perovskite layer.

Figure 4.11 shows the phonon  $DOS$  for  $PTO$ . Two large amplitude peaks in the  $DOS$  of cubic  $PbTiO_3$  are found in the positive energy region. The first one, around  $0.01$  eV, corresponds to the contribution of  $Pb$  atoms. The second one, corresponding to the contribution of  $TiO_2$  layers, is found at around  $0.06$  eV. The  $DOS$  of central perovskite layer recovers the first peak better in energy and in amplitude. The phonon  $DOS$  for interface and central perovskite layer of  $RP$  superlattice recovers the second peak in energy and magnitude, However in  $AF$  series, this peak shifts toward higher energy in both interface and central perovskite layer. In negative energy region, the amplitude of instability in interface perovskite layer is larger than

the bulk cubic, which corresponds to an enhanced ferroelectric instability. The *DOS* of central perovskite layer and bulk cubic correspond well.

The phonon *DOS* reveal that the different layers in superlattices have different dynamic behaviors. The fact that the superlattices can not fully reproduce the phonon properties of bulk cubic perovskites does not mean that the physical quantities in central perovskite layer can not rapidly converge to the bulk ones. Besides, the interaction between atoms in a single perovskite unit cell might converge to the cubic value even more rapidly. Thus, it is interesting to evaluate the inter-atomic force constants in real space, as reported in the next section.

## 4.7 Interatomic Force Constants

In this section, we will investigate the inter-atomic force constants (*IFC*) in real space for *AF* and *RP* superlattices, in the case of  $n=3$ . The *IFC* is defined between each couple of atoms. As described in literature [144], the force  $F_\alpha(\kappa)$ , along  $\alpha$  direction, induced on atom  $\kappa$  by the displacement  $\Delta\tau_\beta(\kappa')$  of atom  $\kappa'$  along  $\beta$  direction is given by

$$F_\alpha(\kappa) = -C_{\alpha,\beta}(\kappa, \kappa') \cdot \Delta\tau_\beta(\kappa')$$

Where  $C_{\alpha,\beta}(\kappa, \kappa')$  is the *IFC* and thus the on-site force constant ( $C_{on}(\kappa)$ ) is defined by  $\kappa = \kappa'$ . The total force (*TT*) between two atoms is defined as the sum of two parts: the dipole-dipole part (*DD*) and the short-range part (*SR*). The dipole-dipole part corresponds the long-range electric interaction between two atoms, which can be calculated analytically. We define the remaining force contribution as the short-range (*SR*) part, which is sensitive to the atomic distance and nature.

From the definition of the *IFC*, we can conclude that the on-site force  $F_{on}(\kappa)$  induced on atom  $\kappa$  is the interatomic forces  $F_{inter}(\kappa, \kappa')$  summed over all other atoms:

$$F_{on}(\kappa) = \sum_{\kappa'} F_{inter}(\kappa, \kappa')$$

This implies that the dynamic behavior of one atom originally depends on  $C_{inter}(\kappa, \kappa')$  (which corresponds to  $F_{inter}(\kappa, \kappa')$ ). Two atoms have the same dynamical properties, if their  $C_{inter}(\kappa, \kappa')$  values are the same, which is a very strict requirement.

In Table 4.6, we report the on-site force constant  $C_{on}(\kappa)$  (which corresponds to  $F_{on}(\kappa)$ ) of each atom, in superlattices and in bulk cubic perovskite structures. For  $Ti$  and  $A$  site atoms the ‘main axis’ component of each atoms refers to the  $z$  direction. The direction along  $Ti-O$  bond was chosen as main axis for  $O$  atoms.  $O_{xy}$  and  $O_z$  refer to the equatorial and apical oxygen atoms in the  $TiO_6$  octahedra.  $Ba$  and  $Sr$  atom have larger mass and smaller on-site force constant ( $<0.1 Ha./Bohr^2$ ) than  $Ti$  and  $O$ , related to low vibration frequencies, which is similar in central and interface layers.

The values for  $O_{xy}$  and  $O_z$  atoms in central layer recover the bulk cubic with small differences ( $<10\%$ ), while the values for  $O_z$  atom in the interface layer show larger differences ( $15\% \sim 20\%$ ). The on-site force constant values for  $Ti$  atoms, in both interface and central layers, recover the bulk values within  $\sim 5\%$ . Next, we have checked the  $C_{inter}(\kappa, \kappa')$  value for the central layer atoms and interface  $Ti$  atoms.

In Figure 4.12, we report the total part of  $C_{inter}(\kappa, \kappa')$  induced on  $Ti$  atoms by its first 100 neighbour atoms given as a function of interatomic distance. The  $Ti$  atom is selected in central and interface perovskite layer of  $Ba$  based  $AF$  and  $RP$  superlattices, in the case of  $n=3$ , and compared with the case of bulk.

In the case of bulk  $BaTiO_3$ , the maximum value of  $C_{inter}(\kappa, \kappa')$  induced on  $Ti$  atoms corresponds to its first  $Ti$  neighbor atom, with a negative value.  $C_{inter}(\kappa, \kappa')$  values between  $Ti$  and  $O$  are weak and positive.  $Ti-Ba$  values are in between and are negative. According to the definition of interatomic force constants, this implies that all  $Ti$  atoms have tendency to move along the same direction along with  $Ba$  atoms, while  $O$  atoms move in opposite direction. These interactions in  $O-Ti-O$  chains play an important role in driving the ferroelectric instability in perovskite lattices.  $Ti-Ti$  and  $Ti-Ba$   $C_{inter}(\kappa, \kappa')$  absolute values decrease when the distance increases. It is interesting to point out that  $C_{inter}(\kappa, \kappa')$  for first neighbor  $Ti$  atom splits into two close values although the distances are equal. This arises for the 3-layers cell we used in our calculation. The error will appear between  $Ti-Ti$  in x-y plane and out-of plane. This kind of error will also appears in our superlattice calculations so that we can compare the values between bulk cubic and superlattices at the same level of error. Similar considerations are valid for  $O$  and  $Ba$  atoms.

TABLE 4.6: The  $z$  component on-site force constant for  $Ti$  and A site atoms and the component along  $Ti-O$  chain of on-site force constant for  $O$  atoms (in  $Ha./Bohr^2$ ) of  $Ba,Sr$  and  $Pb$  based superlattices in  $AF$  and  $RP$  types.  $TT$  refers the total part of the force constants and  $SR$  refers the short range part.  $O_{xy}$  and  $O_z$  refers to the equatorial and apical oxygen atoms in the  $TiO_6$  octahedra.

		BTO		STO		PTO	
		TT	SR	TT	SR	TT	SR
Bulk cubic	Ti	0.15902	0.45660	0.19516	0.53340	0.15507	0.37371
	A	0.08749	0.05730	0.05627	0.02379	0.04033	0.00880
	O	0.13909	0.50493	0.20632	0.62003	0.17763	0.44753
AF Central	Ti	0.16355	0.38037	0.18813	0.41959	0.13875	0.29417
	A	0.08869	0.05987	0.06009	0.02866	0.04316	0.00524
	$O_{xy}$	0.14475	0.57395	0.22712	0.73212	0.19816	0.47480
	$O_z$	0.13654	0.39734	0.19666	0.48172	0.16366	0.36426
AF Interface	Ti	0.17316	0.36996	0.18397	0.39552	0.13125	0.24857
	A	0.08701	0.06952	0.07858	0.06328	0.05064	0.03797
	$O_{xy}$	0.15179	0.54946	0.22984	0.71521	0.19878	0.46815
	$O_z$	0.11921	0.25477	0.16325	0.31807	0.11954	0.21142
RP Central	Ti	0.16566	0.39544	0.19554	0.46371	0.14986	0.32858
	A	0.08837	0.05835	0.06036	0.02808	0.04407	0.00907
	$O_{xy}$	0.14064	0.54513	0.21234	0.66720	0.18802	0.46188
	$O_z$	0.13703	0.41126	0.19737	0.51760	0.16607	0.38296
RP Interface	Ti	0.17800	0.38831	0.18731	0.43298	0.14047	0.29339
	A	0.08692	0.07236	0.09505	0.09072	0.05521	0.05041
	$O_{xy}$	0.14917	0.51873	0.21485	0.64761	0.18887	0.45390
	$O_z$	0.12251	0.24910	0.15266	0.31750	0.11935	0.22244

In the  $AF$  and  $RP$  types superlattices,  $C_{inter}(\kappa, \kappa')$  values for  $Ti$  atoms in central perovskite layers are very similar with the one for bulk cubic. The  $C_{inter}(\kappa, \kappa')$  values for the atoms in  $x-y$  planes are significantly different from the apical one, due to the different atomic distances along these directions. These results imply that the dynamic behavior of  $Ti$  atom selected from central perovskite layers of  $AF$  and  $RP$  superlattices recovers the bulk behavior. To illustrate this, we report in Figure 4.13 the difference of total interatomic force constants between  $Ti$  atoms in central perovskite layer of superlattices ( $C_{SL}$ ) and the one in bulk cubic ( $C_{Cubic}$ ) i.e.  $C_{diff} = C_{Cubic} - C_{SL}$ .  $C_{diff}$  values are very small, in the range between -0.01 and 0.01(in  $Ha./Bohr^2$ ), which is smaller than 1% of the  $C_{on}(Ti)$ .

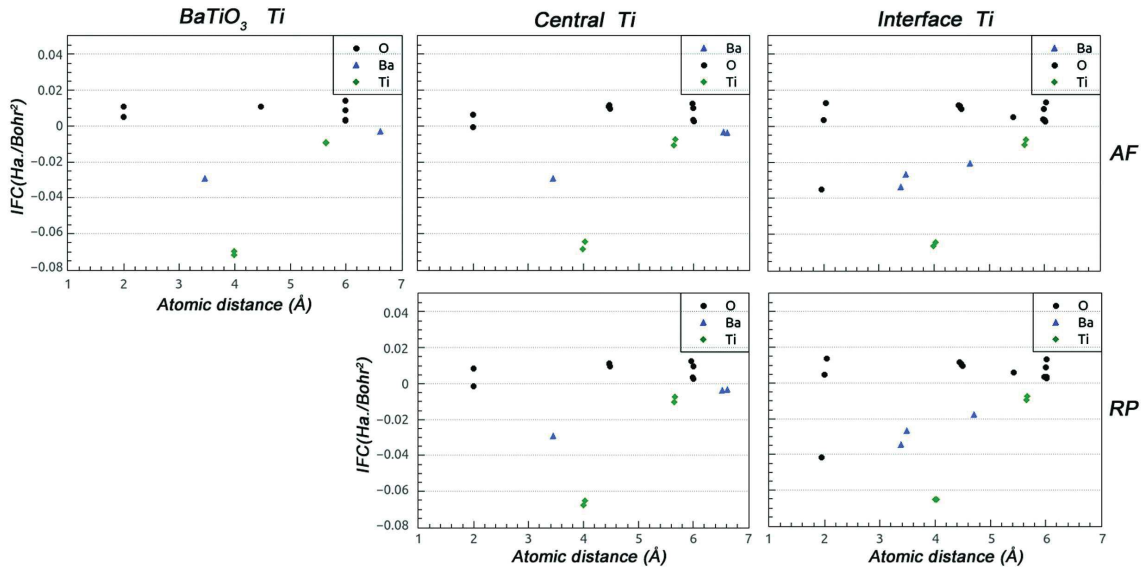


FIGURE 4.12: Interatomic Force Constant ( $IFC$ ) induced on  $Ti$  atom in bulk cubic  $BaTiO_3$  and  $Ba$  based superlattices,  $AF$  and  $RP$  types. The  $IFC$  values depend on different atoms and atomic distances with reference  $Ti$  atom. Atoms differ by colors, green for  $Ti$ , blue for  $Ba$  and black for  $O$ .

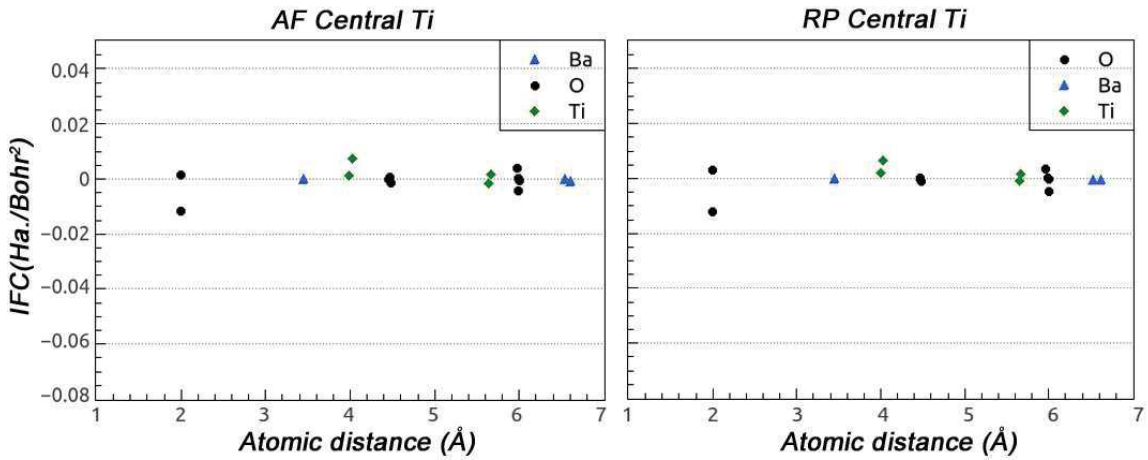


FIGURE 4.13: Difference between the interatomic force constant ( $IFC$ ) induced on  $Ti$  atom in bulk cubic  $BaTiO_3$  and the ones induced on  $Ti$  atom in superlattices. The values depend on different atoms and atomic distances with reference  $Ti$  atom. Atom differ by colors, green for  $Ti$ , blue for  $Ba$  and black for  $O$ .

It is shown in Figure 4.12 that the  $Ti$  atom selected in the interface perovskite layer shows different  $IFC$  values from  $Ti$  in bulk cubic. Its first  $O$  neighbors have significantly different  $C_{inter}(\kappa, \kappa')$  values. Moreover, the second nearest  $Ba$  atom is found at the distance of 4.6 Å while it is found at around 6.6 Å in bulk cubic. These structure features imply that the dynamic behavior of  $Ti$  atom in interface perovskite layer of  $AF$  and  $RP$  superlattices is not expected to recover the one for

bulk perovskite.

*IFC* values reported above confirm that the dynamics of the superlattices converge to the bulk behavior very quickly, i.e. only one perovskite layer away from the interface. Long-range dipole-dipole interactions, which dominate in *IFC* components beyond the first coordination shell, are not significantly affected in the *x-y* directions of the superlattices; this may explain why the dynamics, at least in these directions, converge so fast to the bulk behavior. From Table 4.3 and Figure 10, one can readily figure out that the changes in atomic distances, from the bulk to the superlattices, are not large enough to drastically change *IFC* values.

*IFC* values mentioned above confirm that the dynamics of the superlattices converge to the bulk behavior very quickly, i.e. only one perovskite layer away from the interface. The long-range dipole-dipole interaction is proportional to the term  $\frac{1}{r^2}$  which will not be significantly modified by a relatively small displacement under large atomic distance. From Table 4.3 and figure 4.13, one can readily figure out that the changes in atomic distances, from the bulk to the superlattices, are not large enough to drastically change *IFC* values.

Also, *IFCs* and related dynamic matrices are key input quantities to determine the parameters of model potentials [105], so that there is good hope to develop robust and transferable effective Hamiltonians for simulating the dynamic behavior of more complex or extended (i.e., larger *n* values) superlattices.

## 4.8 Hartree Potential

In order to find more evidences about the effect of rumpling at the interface, we plot the Hartree potential distribution of 3-layers *BTO* in Figure 4.14. We keep the atomic position as they are in cubic and simply move the *Ti* in the perovskite layer with a displacement of 0.4 Å along *z* direction or *x* direction. It is equivalent to creating a small dipole in the cell. In Figure 4.14 the hartree potential of these dipoles are reported as well. It is observed that the hartree potential of these dipoles are localized in a small region inside one perovskite unit cell even for an amplitude of the displacement ten times larger than the rumpling (0.04Å) in the two types superlattices. This means that the rumpling in the interface does not change the hartree potential of the central layer, and that is why the central layer can recover the dynamic properties of cubic-like just one layer away from the interface.

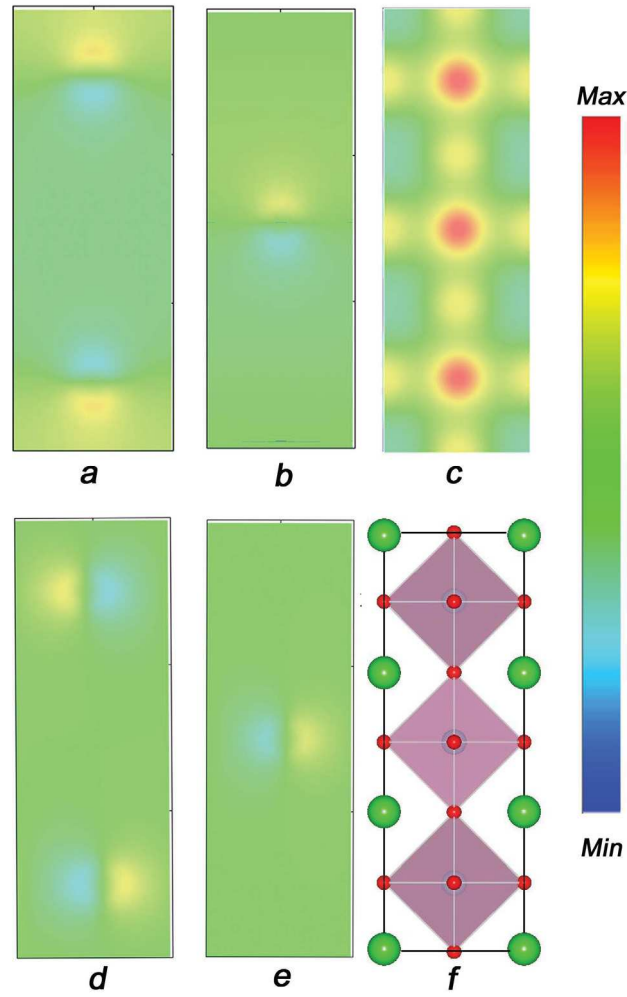


FIGURE 4.14: Hartree Potential in 3-layers *BTO*. a) Dipole created by *Ti* atom in interface layer, moved along  $z$ ; b) Dipole created by *Ti* atom in central layer, moved along  $z$ ; c) Hartree potential of 3-layers *BTO*; d) Dipole created by *Ti* atom in interface layer, moved along  $x$ ; e) Dipole created by *Ti* atom in central layer, moved along  $x$ ; f) Structure of 3-layers *BTO* supercell

## 4.9 Born effective charges and dielectric constants

The long-range Coulomb part of the interatomic force constants relates to the interaction of the Born effective charge ( $Z^*$ , alias dynamic effective charge) screened by the optical dielectric constant. These quantities therefore give precious information in lattice dynamical studies. The Born effective charge is a theoretical concept which can not be experimentally measured directly. In contrast, the optical dielectric tensor can be measured in experiments. In this part, we will investigate the Born effective charge of atoms and the optical dielectric tensor in *AF* and *RP* superlattices.

### 4.9.1 Born effective charges

As it is discussed in Refs [147] and [148], the definition of the Born effective charge is distinct from that of the usual static charge. For periodic solids, the Born effective charge of atom  $\kappa$  is a tensor defined as the coefficient of proportionality at the linear order and under the condition of zero macroscopic electric field, between the macroscopic polarization per unit cell created in direction  $\beta$  and cooperative displacement of atoms  $\kappa$  in direction  $\alpha$  :

$$Z_{\kappa\alpha\beta}^* = \Omega_0 \left. \frac{\partial P_\beta}{\partial \tau_{\kappa\alpha}} \right|_{\varepsilon=0} \quad (4.2)$$

where  $\Omega_0$  is the unit cell volume. The Born effective charge is therefore a dynamical concept in the sense that it concerns the response to an atomic displacement. The Born effective charge must obey a dynamical neutrality condition (i.e. their sum must vanish over the crystal cell). This neutrality condition was extended to the case of surface and interfaces [149, 150] showing that  $Z^*$  can substantially deviate there from their bulk counterparts.

TABLE 4.7:  $Z^*$  in bulk cubic perovskite and rock-salt oxides (in  $|q_{e^-}|$ ),  $\perp$  refers the direction perpendicular to the  $x$ - $y$  plane,  $\parallel$  refers the direction parallel to the  $x$ - $y$  plane.

	BTO		STO		PTO		Nominal charge
	$\perp$	$\parallel$	$\perp$	$\parallel$	$\perp$	$\parallel$	
Ti	+7.458	+7.458	+7.403	+7.403	+7.328	+7.328	+4
A	+2.734	+2.734	+2.552	+2.552	+3.919	+3.919	+2
O	-5.903	-2.145	-5.865	-2.045	-6.042	-2.602	-2
	BaO		SrO		PbO		Nominal charge
	$\perp$	$\parallel$	$\perp$	$\parallel$	$\perp$	$\parallel$	
A	+2.769	+2.769	+2.475	+2.475	+4.718	+4.718	+2
O	-2.769	-2.769	-2.475	-2.475	-4.718	-4.718	-2

In Table 4.7, we report the calculated Born effective charges along different directions for atoms in the superlattices, in the cubic perovskite and in the bulk rock-salt oxides.  $\perp$  and  $\parallel$  refer to the direction perpendicular and parallel respectively to the  $x$ - $y$  plane. Comparing with the nominal charges, anomalously large effective charges appear in

cubic perovskite structures, especially for the  $Ti$  atom and the  $O$  atom along the  $Ti-O$  direction. This implies that  $Ti-O$  chains can be easily polarized along the chain direction, in close relation with the ferroelectric instability. It is worth to point out that the  $Pb$  atom in cubic  $PbTiO_3$  has anomalous large effective charge as well, which confirms that the  $Pb$  atom can be easily polarized in  $PbO$  layer.

TABLE 4.8:  $Z^*$  of atoms (in  $|q_e^-|$ ) in  $Ba$ ,  $Sr$  and  $Pb$  based superlattices of  $AF$  and  $RP$  types.  $\perp$  refers the direction perpendicular to the  $x-y$  plane,  $\parallel$  refers the direction parallel to the  $x-y$  plane. Notations are defined in the main text.

		BTO		STO		PTO	
		$\perp$	$\parallel$	$\perp$	$\parallel$	$\perp$	$\parallel$
AF	Ti <sub>2</sub>	5.731	7.162	5.761	7.281	6.347	7.246
	Ti <sub>4</sub>	6.041	7.382	5.947	7.391	7.090	7.351
	O <sub>0</sub>	-3.402	-2.634	-3.293	-2.276	-3.821	-3.523
	A <sub>0</sub>	4.148	2.671	3.998	2.296	4.734	3.503
	A <sub>1</sub>	2.801	2.592	2.692	2.363	3.928	3.618
	A <sub>3</sub>	2.295	2.759	2.138	2.572	3.902	3.976
RP	Ti <sub>2</sub>	6.008	7.095	6.203	7.178	6.368	7.114
	Ti <sub>4</sub>	6.313	7.351	6.397	7.315	6.832	7.229
	A <sub>1</sub>	3.239	2.632	3.106	2.356	4.326	3.659
	A <sub>3</sub>	2.382	2.759	2.260	2.573	3.695	3.976

In Tables 4.8 and 4.9, we report the Born effective charges in  $AF$  and  $RP$  superlattices in the case of  $n=3$ . Atom  $\kappa_i$  refers to atom  $\kappa$  from layer  $i$  (see Figure 4.2) of the superlattice.  $\parallel_{Ti-O}$  refers to the direction along  $Ti-O$  bond,  $\perp_1$  and  $\perp_2$  refer to the other directions perpendicular to  $\parallel_{Ti-O}$ . It can be easily seen that  $Z^*$  converge to the cubic perovskite values, going from the interface to the central layer. Especially, the component in the  $x-y$  direction is larger than the component along  $z$  (since the infinite  $Ti-O$  chain interactions is preserved along  $x-y$  only). Therefore the ferroelectricity can be more easily induced in the  $x-y$  planes.

In the layer 0 for  $AF$  superlattices, which is of rock-salt type structure, the effective charges of atoms are different from the one in perovskite structures, and from the one of bulk rock-salt oxide: the  $A_0$  atoms are more easily polarized along the  $z$  direction; the effective charges of  $O_0$  atoms along  $z$  direction are larger than the one along  $x-y$  plane, but remain weaker than the values in perovskite cells, since they are not in the same chain than  $Ti$ .

TABLE 4.9:  $Z^*$  of  $O$  atoms (in  $|q_e^-|$ ) in  $Ba$ ,  $Sr$  and  $Pb$  based superlattices of  $AF$  and  $RP$  types.  $\parallel_{Ti-O}$  refers the direction along  $Ti-O$  bond,  $\perp_1$  and  $\perp_2$  refer to the other two directions perpendicular to  $\parallel_{Ti-O}$ .

		BTO			STO			PTO		
		$\parallel_{Ti-O}$	$\perp_1$	$\perp_2$	$\parallel_{Ti-O}$	$\perp_1$	$\perp_2$	$\parallel_{Ti-O}$	$\perp_1$	$\perp_2$
AF	O <sub>1</sub>	-4.242	-2.252	-2.252	-4.218	-2.105	-2.105	-4.834	-2.828	-2.828
	O <sub>2</sub>	-5.656	-2.150	-1.717	-5.751	-2.037	-1.658	-6.054	-2.569	-2.458
	O <sub>3</sub>	-4.816	-2.172	-2.172	-4.727	-2.082	-2.082	-5.873	-2.726	-2.726
	O <sub>4</sub>	-5.828	-2.157	-1.740	-5.844	-2.050	-1.657	-6.073	-2.588	-2.554
RP	O <sub>1</sub>	-4.347	-2.240	-2.240	-4.415	-2.056	-2.056	-4.960	-2.796	-2.796
	O <sub>2</sub>	-5.602	-2.176	-1.800	-5.672	-2.053	-1.758	-5.947	-2.620	-2.367
	O <sub>3</sub>	-5.034	-2.164	-2.164	-5.082	-2.062	-2.062	-5.696	-2.696	-2.696
	O <sub>4</sub>	-5.602	-2.161	-1.807	-5.784	-2.058	-1.754	-5.974	-2.633	-2.415

The Born effective charges are defined for atoms but are related to the global dynamical behavior of the lattice, and especially to the long-range dipole-dipole interactions. Our results show that  $Z^*$  of central perovskite layers in superlattices reproduce well those of cubic perovskite. For displacement in the  $x$ - $y$  plane, the convergence is much slower along the  $z$  direction. At the interfaces,  $Z^*$  can deviate substantially from the bulk values.

### 4.9.2 Optical dielectric tensor

The dielectric tensor is a macroscopic concept related to the macroscopic displacement field  $D$ , the macroscopic electric field  $\xi$  and the macroscopic polarization  $P$  as follows:

$$D_\alpha = \xi_\alpha + 4\pi P_\alpha \quad (4.3)$$

while the dielectric tensor is introduced as

$$\varepsilon_{\alpha\beta} = \left. \frac{\partial D_\alpha}{\partial \xi_\beta} \right|_{\xi=0} \quad (4.4)$$

From the definition we can see that the dielectric tensor globally describes the screening of a macroscopic electric field by a polarizable medium. In solids, both the electrons and the ions may polarize under the action of a macroscopic electric field. In this part, we will only address the contribution of the electronic polarization to the dielectric tensor (i.e. the optical dielectric tensors).

In Table 4.10 we report the optical dielectric tensor values of  $AF$  and  $RP$  superlattices, cubic perovskites and bulk rock-salt oxides.  $\epsilon_i$  refers to the component of the dielectric tensor along  $i$  direction. In bulk cubic systems the dielectric tensor reduces to a scalar. Table 4.10 shows that the dielectric tensor of each  $AF$  and  $RP$  superlattice converges to the cubic perovskite values, especially the component along the  $x$ - $y$  plane.

Comparing to the experimental data, the theoretical calculation overestimates the dielectric constant values of bulk cubic perovskite. The error is around 30% in  $BaTiO_3$ , 22% in  $SrTiO_3$  and 2% in  $PbTiO_3$ . The origin of this error is complex and has been briefly discussed in Ref. [90]. On one hand, it comes at least partly from the approximation used for the exchange-correlation functional: the  $GGA$  approximation we used, in which the long-range interactions are not included in the exchange-correlation potential. On the other hand, the cubic structure of  $BaTiO_3$  and  $SrTiO_3$  observed in experiment is actually the average of local distortions which depend on the material.

It is worth to mention that the dielectric tensor of superlattices have smaller values than the cubic perovskite in both  $BTO$  and  $STO$  systems, while in  $PTO$  system the relation between them is opposite. This may arise from the rock-salt type layer in superlattices. As it is shown in Table 4.10, the dielectric tensor of bulk cubic is larger than the one in cubic perovskite in  $Pb$  based system, the  $Pb$  atom is easily polarizable in rock-salt type structure. The values for  $AF$  and  $RP$  superlattice is in between since they are as combination of these two types of structures.

In order to estimate how each type of structure, perovskite and rock-salt, contributes to the dielectric tensor of the superlattice, we calculate the effective dielectric tensor by treating the superlattice as a capacitor arising from the stacking of the perovskite and rock-salt unit cell. Each component of the effective dielectric tensor  $\epsilon'$  is defined by the following expressions:

TABLE 4.10: Dielectric constant in superlattices, bulk cubic perovskite and bulk rock-salt oxides.  $z$  refers to the component along  $z$  and  $x-y$  refers to the component along  $x-y$  plane.

		n=1		n=2		n=3		Cubic		Rock-salt
		$z$	$x-y$	$z$	$x-y$	$z$	$x-y$	Theory	Exp.[151]	AO
BTO	AF	4.910	5.099	5.325	5.580	5.599	5.864	6.834	5.24	4.325
	RP	5.083	5.386	5.540	5.866	5.833	6.124	6.834	5.24	4.325
STO	AF	4.557	4.818	4.984	5.284	5.251	5.548	6.430	5.18	3.871
	RP	4.904	5.177	5.355	5.613	5.608	5.835	6.430	5.18	3.871
PTO	AF	9.181	10.662	8.980	9.802	8.852	9.521	8.832	8.64	26.666
	RP	8.409	9.106	8.371	8.820	8.442	8.777	8.832	8.64	26.666

$$\frac{d_{sl}}{\varepsilon'_z} = \frac{d_p}{\varepsilon_{p(z)}} + \frac{d_r}{\varepsilon_{r(z)}} \quad (4.5)$$

$$\varepsilon'_{xy} d_{sl} = \varepsilon_{p(xy)} d_p + \varepsilon_{r(xy)} d_r \quad (4.6)$$

Here,  $d_{sl}$  refers to the thickness of the superlattices unit cell,  $d_p$  and  $d_r$  refer to the thickness of perovskite and rock-salt slab respectively.  $\varepsilon_{p(i)}$  and the  $\varepsilon_{r(i)}$  refer to the dielectric component of the cubic perovskite and bulk rock-salt oxides along direction  $i$ .

TABLE 4.11: Effective dielectric constant ( $\varepsilon'_z$ ), dielectric constant ( $\varepsilon_z$ ) and the relative difference between them ( $(\varepsilon'_i - \varepsilon_i)/\varepsilon_i$ ) in  $AF$  type of  $Ba$ ,  $Sr$  and  $Pb$  based superlattices.

		$\varepsilon'_z$	$\varepsilon_z$	Diff( $\varepsilon'_z$ )	$\varepsilon'_{xy}$	$\varepsilon_{xy}$	Diff( $\varepsilon'_{xy}$ )
BTO	n=1	5.110	4.910	4.0%	5.375	5.099	5.4%
	n=2	5.524	5.325	3.7%	5.808	5.580	4.1%
	n=3	5.777	5.599	3.2%	6.043	5.864	3.1%
STO	n=1	4.687	4.557	2.8%	4.990	4.818	3.6%
	n=2	5.108	4.984	2.5%	5.428	5.284	2.7%
	n=3	5.366	5.251	2.2%	5.662	5.548	2.1%
PTO	n=1	14.127	9.181	53.9%	18.827	10.662	76.6%
	n=2	11.949	8.980	33.1%	15.787	9.802	61.1%
	n=3	11.025	8.852	24.6%	14.136	9.521	48.5%

In Table 4.11 and 4.12, we report the values of effective dielectric tensor of  $AF$  and  $RP$  superlattices from  $n=1$  to 3, in which the relative difference is defined as  $(\varepsilon'_i - \varepsilon_i)/\varepsilon_i$ . When  $n$  increases, the difference between  $\varepsilon'$  and  $\varepsilon$  tensors decreases. We can see that in the  $Ba$  and  $Sr$  based superlattices, the effective dielectric tensor matches the dielectric constant value from calculations very well, both in  $AF$  and  $RP$  cases (the value difference is below 9% and can decrease below 3% when  $n$  increases to 3). However, in  $Pb$  based superlattices, this difference is larger than 18%. Such a big difference might arise because bulk  $PbO$  has a significantly large dielectric constant. In  $AF$  and  $RP$  superlattices, the  $PbO$  type  $layer\ 0$  has different  $Z^*$  value with the one in bulk  $PbO$ , which implies that the  $PbO$   $layer\ 0$  has different dielectric contribution to the bulk rock-salt. That is why such big difference arises when we use the value from the bulk to build the effective dielectric tensor. In the case of  $Ba$ ,  $Sr$  based superlattices, the  $layer\ 0$  has similar contribution so that the difference between  $\varepsilon'$  and the  $\varepsilon$  is relatively small. It is worth to point out that all the significant differences converge to zero in  $AF$  and  $RP$  structure when  $n$  increases.

TABLE 4.12: Effective dielectric constant ( $\varepsilon'_z$ ), dielectric constant ( $\varepsilon_z$ ) and the relative difference between them ( $(\varepsilon'_i - \varepsilon_i)/\varepsilon_i$ ) in  $RP$  type of  $Ba$ ,  $Sr$  and  $Pb$  based superlattices.

		$\varepsilon'_z$	$\varepsilon_z$	Diff( $\varepsilon'_z$ )	$\varepsilon'_{xy}$	$\varepsilon_{xy}$	Diff( $\varepsilon'_{xy}$ )
BTO	n=1	5.515	5.083	8.5%	5.800	5.386	7.7%
	n=2	5.941	5.540	7.2%	6.184	5.866	5.4%
	n=3	6.159	5.833	5.6%	6.360	6.124	3.8%
STO	n=1	5.107	4.904	4.1%	5.427	5.177	4.8%
	n=2	5.534	5.355	3.4%	5.804	5.613	3.4%
	n=3	5.761	5.608	2.7%	5.981	5.835	2.5%
PTO	n=1	11.954	8.409	42.2%	15.796	9.106	73.5%
	n=2	10.560	8.371	26.1%	13.195	8.820	49.6%
	n=3	10.020	8.442	18.7%	11.995	8.777	36.7%

## 4.10 Conclusion and perspectives

The rock-salt interface plays an important role in  $AF$  and  $RP$  superlattices, by breaking the long-range  $Ti-O$  chain coherence in the direction perpendicular to the interface. In this case, most phonon instabilities, appearing in bulk cubic perovskites, and corresponding to atomic motions along  $z$  direction, disappear in  $Ba$ ,  $Sr$ ,  $Pb$

based *AF* and *RP* superlattices. This suggests the importance of the long-range interaction between perovskite blocks in periodic lattices for phonon instabilities, including ferroelectric and anti-ferrodistortive instabilities. To generate the phonon instabilities of bulk cubic perovskites, we need to reach a size compatible with the “correlation volume” in superlattices with *Ba* and *Sr*. In *Pb* based superlattices, the ferroelectric phonon instability is partly driven by the *PbO* interface, which appears in bulk *PbO* as well. This is independent from  $n$  and especially enhanced in *AF* series. This might indicate a potential possibility to tune further the ferroelectric properties in *Pb* based perovskite superlattices.

Although the “correlation volume” is not achieved when  $n \leq 3$ , the dynamical properties of central perovskite layers has already recovered the one of bulk cubic perovskite, as shown in our results. Comparing with the ideal structure of bulk cubic perovskite, significant atomic rumpling appears in the interface perovskite layers, which distorts the structure of the perovskite unit cell so that the lattice constants and the atomic bond lengths are affected in this layer. In the central perovskite layer, the unit cell has similar lattice constant and the atomic positions are cubic-like. Thus, the atomic rumpling in the interface perovskite layer does not have a long-range effect. It has been shown that the dynamic properties of cubic perovskite is well reproduced by the central perovskite layer, including phonon *DOS*, interatomic force constants and Born effective charges. We can conclude that these physical quantities converge fast from the interface to the central perovskite layer, and this requires only one perovskite layer away from the interface perovskite layer.

The results about the distribution of Hartree potential in Figure 4.14 demonstrate that the local structure distortion, at least in perovskite series superlattices, is only efficient in a local region and will not change the dynamics of the next perovskite layer. This analysis may suggest a way to distinguish the interface part from the central part in thick superlattices.



# Chapter 5

## *PbTiO<sub>3</sub>/SrTiO<sub>3</sub> (m/n)* superlattices

### 5.1 Introduction

As discussed in Chapter 3, in the very-short period limit, *PTO/STO(1/1)* superlattices can exhibit unusual couplings between lattice modes, yielding eventually hybrid improper ferroelectricity. Independently, larger period systems have also been the topic of intensive studies [152–155]. Strontium titanate is not ferroelectric. Depending of its thickness, the *PTO* layers can be more or less electrostatically coupled or decoupled, yielding different kinds of domain structures. Few first-principles investigations of such systems have been reported [3,4] but are computationally very costly. Accessing the dynamical properties of large superlattices using the effective potentials introduced in Chapter 3 would be very useful. However, we need to clarify how to fit such a model from first-principles calculations on very simple systems. Chapter 4 has demonstrated that the dynamical properties converge very quickly to bulk values when increasing thicknesses. We here check these results explicitly on *PTO/STO(m/n)* superlattices.

We will briefly introduce the structure we are interested in and then study the phonon density of states (*DOS*) and the interatomic force constants (*IFC*). We do not report the phonon dispersion curves since it is more difficult to distinguish the layers contribution than in *DOS*. We will see that the conclusions in Chapter 4 hold in *PTO/STO(1/3)* and *PTO/STO(3/1)* systems as well, which opens the possibility of

building effective Hamiltonians for thick superlattices, by using the data from short period superlattices.

## 5.2 Structures of interest and technical details

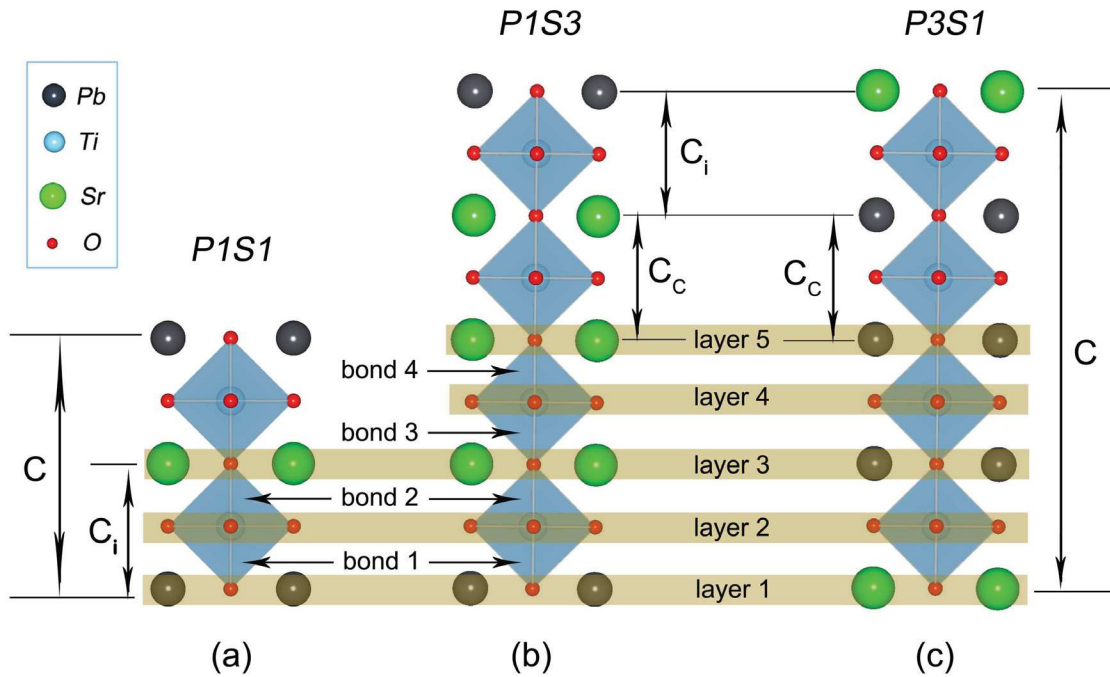


FIGURE 5.1:  $PTO/STO(m/n)$  superlattices with different periods. (a)  $PTO/STO(1/1)$ ; (b)  $PTO/STO(1/3)$ ;  $PTO/STO(3/1)$ . Layers are labeled from layer 1 to layer 5 and the  $Ti-O$  bonds are labeled from bond 1 to bond 4.  $C_c$  refers to the thickness of central layer,  $C_i$  refers to the thickness of interface layer and  $C$  is lattice constant along  $z$ .

$PTO/STO(1/3)$  ( $P1S3$ ) and  $PTO/STO(3/1)$  ( $P3S1$ ) unit cells are shown in Figure 5.1, where the superlattices are built by stacking the perovskite unit cells along the  $z$  direction. In  $P1S3$  there is one  $PbTiO_3$  unit cell after each block of 3  $SrTiO_3$  unit cells, and vice versa in  $P3S1$ . As shown in Figure 5.1, the first  $AO$  ( $A=Pb, Sr$ ) layer from the interface is labeled layer 1, layer 2 is the next  $TiO_2$  layer along  $z$  and so on. In this case we can define layer 1, layer 2 and layer 3 as the ‘interface layer’ while layer 5, layer 4 and layer 3 can be combined as ‘central layer’. Thus, layer 3 is shared by interface and central layers.

As it is discussed in Chapter 4, we try to estimate the dynamical properties of interface layers from the knowledge of the  $PTO/STO(1/1)$  ( $P1S1$ ) system and estimate the central layer behavior from bulk perovskite. All the results of first-principles

calculations are obtained by using the ABINIT software package as in previous chapters.  $6 \times 6 \times 6$  k-grid for Brillouin-zone sampling was used for bulk cubic  $SrTiO_3$  and tetragonal  $PbTiO_3$  and a  $6 \times 6 \times 2$  k-grid was applied for  $P1S3$  and  $P3S1$  superlattices, For  $P1S1$ , we used a  $6 \times 6 \times 4$  k-grid.

### 5.3 Structure Relaxation

All structures in this chapter were fully relaxed along the  $z$  axis in high symmetry phase, and at the same time we fixed the in-plane lattice constant to the value of cubic  $SrTiO_3$ . Thus, in-plane strain was induced for  $PbTiO_3$ . In this case the bulk  $PbTiO_3$  and  $PTO/STO(m/n)$  superlattices are in the tetragonal phase of space group  $P4/mmm$  (123).

As in Chapter 4, we define the average plane coordinate for each layer as  $z_{aver} = (z_{cat} + z_O)/2$  and the rumpling of each layer as  $R_{aver} = (z_{cat} - z_O)/2$ . We relaxed the lattice constant along  $z$  of each structure and the thickness of the interface ( $C_i$ ) and central layers ( $C_c$ ) for  $P1S3$  and  $P3S1$  superlattices. In Table 5.1, we observe that the thickness of each perovskite layers in  $P1S1$  is around the average of cubic  $SrTiO_3$  and tetragonal  $PbTiO_3$ . The thickness of interface layer in  $P1S3$  and  $P3S1$  perfectly recovers the value of  $P1S1$  with a difference below 0.1%. The thicknesses of central layer in  $P1S3$  and  $P3S1$  are similar to the values of cubic  $SrTiO_3$  and  $PbTiO_3$  respectively, with a difference below 0.1%. The lattice constant along  $z$  of  $P3S1$  is significantly larger than the one of  $P1S3$ , since it contains a larger number of tetragonal  $PbTiO_3$  unit cells.

TABLE 5.1: The lattice constant  $C$  (along  $z$ ) for  $PTO/STO(m/n)$  ( $P1S3$ ,  $P3S1$  and  $P1S1$ ), bulk cubic  $SrTiO_3$  and bulk tetragonal  $PbTiO_3$ . Thickness of central layer  $C_c$ , and interface layer  $C_i$  (in Å).

	P1S3	P3S1	P1S1	$PbTiO_3$	$SrTiO_3$
$C_i$	3.876	3.874	3.875	3.906	3.845
$C_c$	3.843	3.907	3.875	3.906	3.845
$C/(m+n)$	3.860	3.891	3.875	3.906	3.845

The  $PTO/STO(m/n)$  system shows atomic rumpling as well. In relaxed structures, the rumpling appears mainly at interface and reduces quickly away from interface to the central layer. In Table 5.2, we observe that layer 2 ( $TiO_2$  type) shows the

maximum rumpling amplitude which is around  $0.016\text{\AA}$  in each system. From layer 3 to layer 5, the rumpling of each layer become negligible.

Another related quantity are the  $Ti-O$  bond lengths along  $z$ , which are reported in Table 5.3. We can see that in  $PTO/STO(m/n)$  systems, the  $Ti-O$  bond length in the  $PbTiO_3$  layer is similar to the one in tetragonal bulk  $PbTiO_3$  with a difference below 0.1%. The  $Ti-O$  bond length in the  $SrTiO_3$  layer nicely recovers the one in cubic bulk  $SrTiO_3$  with a difference also below 0.1%.

TABLE 5.2: Value of rumpling for each layer in  $PTO/STO(m/n)$  superlattices ( $P1S3$ ,  $P3S1$  and  $P1S1$ ) (in  $\text{\AA}$ ). Each layer is labeled in Figure 5.1.

	P1S3	P3S1	P1S1
layer 1	0	0	0
layer 2	-0.016	0.016	-0.015
layer 3	0.001	-0.002	0
layer 4	-0.000	0.000	—
layer 5	0	0	—

These results indicate that the interface breaks the symmetry along the  $z$  direction and leads to atomic rumpling. This kind of effect is localized in the interface region and does not propagate beyond one perovskite layer (around  $4\text{\AA}$ ). The  $Ti-O$  bond length relies on the  $A$  site atom in each perovskite layer as well.

TABLE 5.3:  $Ti-O$  bond lengths along  $z$  in  $PTO/STO(m/n)$  superlattices ( $P1S3$ ,  $P3S1$  and  $P1S1$ ) and bulk (in  $\text{\AA}$ ), Each bond is labeled in Figure 5.1.

	P1S3	P3S1	P1S1	$PbTiO_3$	$SrTiO_3$
bond <sub>1</sub>	1.954	1.921	1.954	1.953	1.922
bond <sub>2</sub>	1.921	1.955	1.921	1.953	1.922
bond <sub>3</sub>	1.923	1.953	—	1.953	1.922
bond <sub>4</sub>	1.922	1.953	—	1.953	1.922

## 5.4 Phonon density of states

The contribution of each layer to the phonon  $DOS$  is divided into central and interface layer and reported in Figure 5.2. There are mainly two peaks reported in the negative region (unstable modes). The one with lowest energy corresponds to the unstable

rotation modes involving  $O$ ; the other one with higher energy indicates the unstable polar modes.

Four narrow peaks with large amplitude, which are related to atomic motions of only one kind of atom, are found in the positive energy region. The first one, around  $0.005eV$ , corresponds to the contribution of  $Pb$  atoms. The second one, around  $0.015eV$ , corresponds to the contribution of  $Sr$  atoms. The third and the fourth are found around  $0.07eV$  and  $0.1eV$  and arise from the contribution of  $O$  atoms. The broad region involves the motion of  $Ti$  and  $O$  atoms.

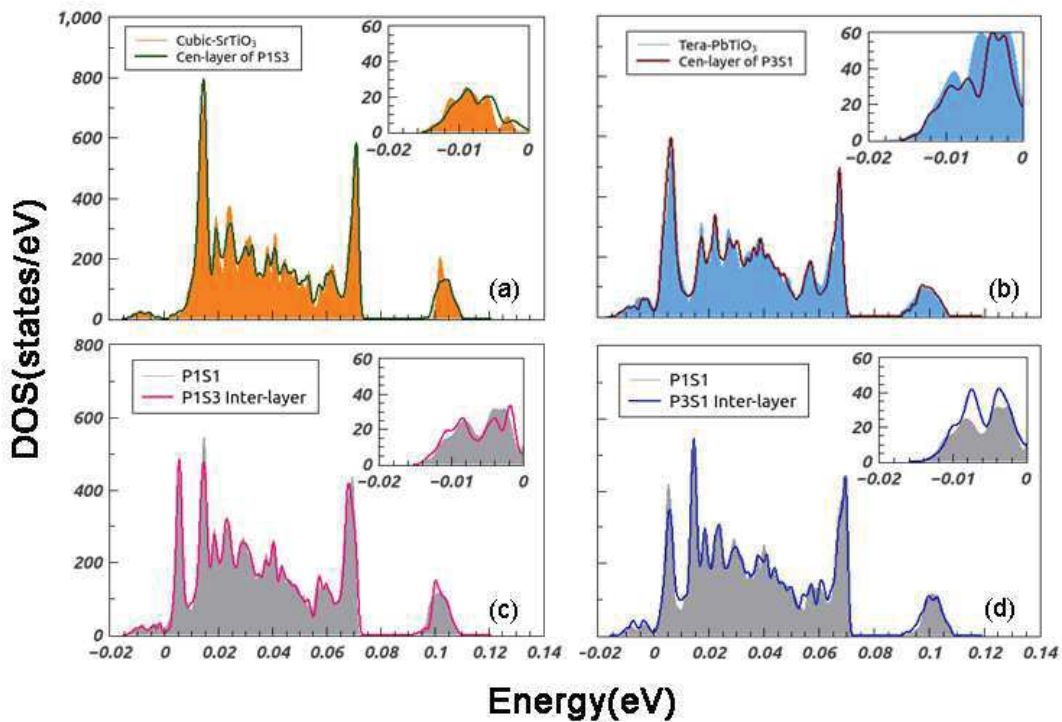


FIGURE 5.2: Phonon density of states( $DOS$ ) of interface and central layer in  $P1S3$  and  $P3S1$  cases and the  $DOS$  for bulk. (a) bulk cubic  $SrTiO_3$  (orange) and central layer in  $P1S3$  (green line); (b) bulk tetragonal  $PbTiO_3$  (light blue ) and central layer in  $P3S1$  (brown line); (c)  $P1S1$  case (gray) and the interface layer in  $P1S3$  (pink line); (d)  $P1S1$  case (gray) and the interface layer in  $P3S1$  (dark blue line).

Figure 5.2 shows that the phonon  $DOS$  of the central layer in  $P1S3$  and  $P3S1$  reproduces almost identically the  $DOS$  of bulk perovskite; the same conclusion holds for interface phonon  $DOS$  which fully recovers the  $DOS$  for  $P1S1$  structures.

These results confirm that the dynamic behavior quickly converge to bulk, and one perovskite layer away from interface is enough. This can be explained by the fact that

the central layer has similar atomic positions and lattice constants with bulk. This explains also that the interface part reproduces well the dynamic behavior of  $P1S1$  superlattices. It is worth to mention that the contribution of unstable polar modes can be separated into two parts: the in-plane and out-of-plane part. By checking the atomic motions, we can see that, for the out-of-plane parts, the atomic polar motions are mainly from  $O$  atoms, both in  $Ti-O$  chain and in  $PbO-SrO$  plane, while the  $Pb$ ,  $Sr$  and  $Ti$  atoms are relatively fixed; for the in-plane part, the atomic polar motions arise not only from the  $Ti-O$  chains but also from the  $PbO$  layers.

## 5.5 Interatomic force constants

As in chapter 4, the interatomic force constant ( $IFC$ ) were calculated in view of simulating the dynamical behavior of superlattices. We will follow the same steps as above, comparing the central layer of  $P1S3$  and  $P3S1$  with the bulk perovskite, and the interface perovskite layer of  $P1S3$  and  $P3S1$  with the  $P1S1$  superlattices. We illustrate our results by reporting the total part  $IFC$  of  $Ti$  atoms in Figure 5.3.

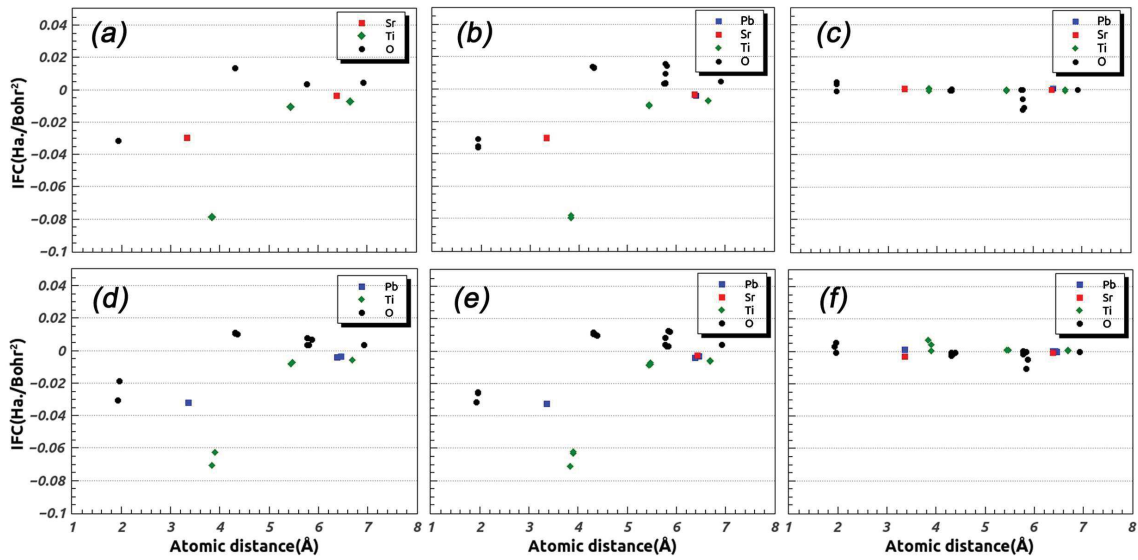


FIGURE 5.3: Interatomic force constant ( $IFC$ ) for each  $Ti$  atom in  $PTO/STO(m/n)$  ( $P1S3$  and  $P3S1$ ) superlattices, bulk cubic  $SrTiO_3$  and bulk tetragonal  $PbTiO_3$  and the difference of  $IFC$  values. (a) Distribution of  $IFC$  for  $Ti$  atom in bulk cubic  $SrTiO_3$ ; (b) Distribution of  $IFC$  for  $Ti$  atom in central layer of  $P1S3$ ; (c) Difference of  $IFC$  between the  $Ti$  values in (b) and the ones in (a); (d) Distribution of  $IFC$  for  $Ti$  atom in bulk tetragonal  $PbTiO_3$ ; (e) Distribution of  $IFC$  for  $Ti$  atom in central layer of  $P3S1$ ; (f) Difference of  $IFC$  between the  $Ti$  values in (e) and the one in (d).

It is observed that the  $IFC$  values for Ti decrease when the atomic distance increases. The maximum absolute  $IFC$  value is found between  $Ti$  and its first neighbor  $Ti$ , with a negative value. In Figure 5.3 we can see that the central layer of  $P1S3$  and cubic  $SrTiO_3$  have similar  $IFC$  values distribution while the one of for central layer of  $P3S1$  matches well tetragonal  $PbTiO_3$  data. The only difference is that there are two different atoms ( $Pb$  and  $Sr$ ) found at around  $6.4 \text{ \AA}$  in superlattices, while there is only one in bulk system. Hopefully this kind of difference may not cause big changes for the dynamic behavior of selected  $Ti$  atom, since the atomic distance is large enough (more than one perovskite cell) and the amplitude is small (below  $0.01 \text{ Ha./bohr}^2$ ). Considering the differences between the central layer of superlattices and the bulk material reported in Figure 5.3(c) and (f), we can expect that the  $Ti$  atom in central layer of superlattices will nicely reproduce the dynamic behavior of the one in bulk.

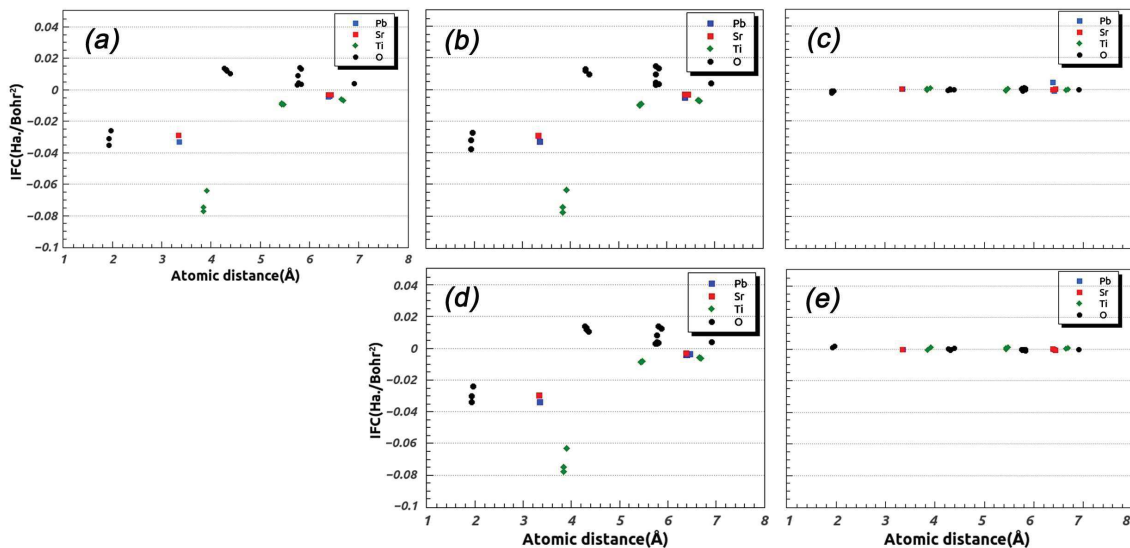


FIGURE 5.4: Interatomic force constants ( $IFC$ ) for each  $Ti$  atom in  $P1S1$  ( $P1S3$ ,  $P3S1$  and  $P1S1$ ) superlattices, and the difference of  $IFC$  between them. (a) Distribution of  $IFC$  for  $Ti$  atom  $P1S1$ ; (b) Distribution of  $IFC$  for  $Ti$  atom in interface layer of  $P1S3$ ; (c) Difference of  $IFC$  between the  $Ti$  values in (b) and the one in (a); (d) Distribution of  $IFC$  for  $Ti$  atom in  $P3S1$ ; (e) Difference of  $IFC$  between the  $Ti$  values in (d) and the ones in (a).

For the case of  $Ti$  atom in the interface layer of  $P1S3$  and  $P3S1$ , we compare  $IFC$  values with the ones in  $P1S1$  superlattices. The difference with the  $Ti$  in bulk is that  $Pb$  and  $Sr$  atoms are both found at around  $3.4 \text{ \AA}$ . We observed similar  $IFC$  distributions in the amplitude with small differences of  $IFC$  value between them shown in Figure 5.3. Thus, we can expect that these three selected  $Ti$  atoms will have similar dynamic behaviors.  $IFC$  for other atoms are not reported here since they lead to the same conclusions.

## 5.6 Conclusion

In this chapter, we studied the relaxed structure of  $PTO/STO(1/3)$  and  $PTO/STO(3/1)$  superlattices under fixed in-plane lattice constant at the value of cubic  $SrTiO_3$ . At the same time, we took the bulk cubic  $SrTiO_3$ , tetragonal  $PbTiO_3$  and  $PTO/STO(1/1)$  superlattices as the reference structures.

Lattice constant along  $z$ , atomic position and  $Ti-O$  bond lengths of  $P1S1$  are well reproduced in the interface region of  $P1S3$  and  $P3S1$ . Due to the broken symmetry along  $z$  direction, atomic rumpling appears at interface region of  $P1S3$  and  $P3S1$  superlattices. However, the effect of this additional rumpling is localized at interface region. In the central layer of  $P1S3$  and  $P3S1$  the atomic position and lattice constants recover well the bulk values. The  $Ti-O$  bond lengths recover the bulk values and the rumpling rapidly become negligible after one perovskite layer away from interface.

The atomic positions is an important factor for the force induced on each atom. We investigated the layer dependent dynamic properties of  $P1S3$  and  $P3S1$  and reported the phonon density of states. Finally we reach similar conclusions than in Chapter 4, that the dynamics of central layers in  $P1S3$  and  $P3S1$  recover the bulk behavior, while the dynamics of interface layer recover the short periodic  $P1S1$  superlattice.

# Conclusions and perspectives

In the present thesis, we investigated the dynamical properties of perovskite compounds from bulk to layered systems. A timely challenge in the field is to succeed describing the behavior of such systems at finite temperatures. Recently, a new type of first-principles effective atomic potential was introduced and that provided successfully access to the finite temperature properties of some simple bulk perovskite compounds. On the one hand, in our investigations, we demonstrated that this new effective potential approach is suitable for more complex systems combining numerous structural instabilities. On the other hand, since such first-principle effective atomic potentials are built from the output of first-principles calculations, we explored possible strategies for extending this to larger superlattices that is not directly accessible at the first-principles level. Our main results can be summarized as follows.

In Chapter 3, we first investigated the dynamical properties of  $PTO/STO(1/1)$  superlattices at ‘zero Kelvin’. It was observed that many lattice instabilities are present in the Brillouin zone (BZ) of the high-symmetry  $P4/mmm$  phase, including in-plane ( $P_x, P_y$ ) and out-of-plane ( $P_z$ ) atomic polar motions as well as unstable oxygen rotational modes at the BZ boundary ( $\phi_{zi}, \phi_{zo}, \phi_{xo}, \phi_{yo}$ ). These unstable phonon modes typically compete with each others at the bi-quadratic level but can cooperate through trilinear couplings. Besides, we noticed that strain can strongly affect the lattice dynamics of the system by stiffening or softening some phonon modes.

We identified the ground state of  $PTO/STO(1/1)$  superlattices epitaxially grown on  $SrTiO_3$  substrate, as a  $P_C$  phase combining  $R_{xyz}M_zP_{xyz}$  distortions. This ground state appears as the combination of a strongly dominant  $R_zM_zP_z$  distortion with an almost negligible  $R_{xy}M_zP_{xy}$  distortion, producing an additional gain of energy at the limit of our calculation accuracy.

We developed a simple Landau type model in terms of the dominant  $R_z, M_z$  and  $P_z$  order parameters. This simple model well reproduced the first-principles energy

data and highlights the importance of the trilinear coupling between  $R_z$ ,  $M_z$  and  $P_z$ . Furthermore, we phenomenologically investigated the temperature-dependent phase transition behavior with this model. We demonstrated that such simple model fitted on first-principles well describes the complex hybrid improper ferroelectric behavior and reproduces the experimental results from the literature. It also shows that even in case  $R_z$  and  $M_z$  condense individually at different temperatures,  $P$  can keep its improper characters.

First-principles model atomic potentials were then constructed for this  $PTO/STO(1/1)$  system to further investigate the temperature dependent behaviors. As the temperature decreases, consecutive phase transitions were observed:  $R_z$  condenses first, then  $M_z$  and  $P_z$  appear together due to the trilinear coupling, and finally  $R_x$  and  $P_x$  appear at very low temperatures. This seems to contradict initial experimental results that report the simultaneous appearance of  $R_x$ ,  $M_x$  and  $P_x$ . However, when a negative pressure is applied (-6.9 GPa) to our model to empirically correct for the LDA volume underestimation,  $M_z$  and  $P_z$  show tendency to condense more closely together with  $R_z$ . These have to be considered as preliminary results. They attest of the ability of the model potentials to describe complex systems. Now, further works are still needed to confirm these results and to clarify the effects of different approximations such as the LDA, or the truncation of some atomic interactions. Beyond this, our work illustrate the interest of such calculations to access many other properties. For instance, playing with the coexistence of  $R_z M_z P_z$  and  $R_{xy} M_z P_{xy}$  distortions, we have shown the possibility of tuning the in-plane component of polarization with an out-of-plane electric field.

In Chapter 4, we studied the convergence of interatomic force constant (*IFC*) and dynamical properties with the layer thicknesses, in natural and artificial *Ba*, *Sr*, *Pb*-based  $AO/ABO_3$  superlattices. It is observed that i) ferroelectric and antiferrodistortive instabilities require relatively long-range correlations. To reproduce the phonon instabilities of bulk cubic perovskites, the correlation volume must be achieved in superlattices; ii) the dynamical properties of perovskite layers one unit cell away from the interface have already recovered the behavior of bulk cubic perovskite, since the atomic rumpling at the interface perovskite layer does not have a long-range effect. One cell away from the interface, the crystal structure is very close to the one of the pristine bulk oxide and the dynamical properties are also very similar to bulk ones, including phonon *DOS*, interatomic force constants and Born

effective charges. These investigations demonstrate the possibility to treat the central and interface parts separately when building atomic potentials for large periodic superlattices.

In Chapter 5, we confirmed this conclusion in other systems,  $PTO/STO(1/3)$  and  $PTO/STO(3/1)$  superlattices: the dynamics of central layers recover that of the bulk material due to the short-range interface rumpling, and the dynamics of the interface part can be estimated from the related short periodic superlattices  $PTO/STO(1/1)$ , which can be directly obtained from the first-principles calculations.

This thesis so opens promising perspectives: starting from the first-principles calculations at zero Kelvin for bulk crystals and short-period superlattices, effective atomic potentials can be built providing access to describe the temperature dependent phase transition behaviors and the lattice dynamics of complex systems, in which various instabilities coexist. This technique does not only work for short period systems, but can be extended to larger period ones. It will renders possible a theoretical investigation, based on first-principles, of the dynamics and temperature dependent phase transition behavior of more complex materials of more direct interest to experimentalists. Based on these remarks, we can propose some guidelines for future investigations.

First, as discussed in Chapter 3, our model potentials still need to be taken with caution and validated, especially testing the approximations that are used. For instance, the dependence on lattice parameters, since the lattice instabilities are very sensitive to them. Also, in this preliminary model, the oxygen interactions were limited to very short range, which should be carefully checked. A better description of these interactions may eventually be required for properly addressing the physics of the system.

Second, as it mentioned above, the ability of the first-principles effective atomic potential is not limited in reproducing DFT results. It opens the door to more physics such as phase transition behavior, the switching of polarization and various functional properties at finite temperatures. Taking an example, since the strain can strongly effect the lattice dynamics, such model will allow us to follow the evolution of physics vs. epitaxial strain. In the  $PTO/STO$ , compressive strain will strongly increase the instability of out-of-plane polar mode ( $P_z$ ), that may become eventually more unstable than the out-of-phase octahedral rotation mode ( $R_z$ ). This will possibly

make  $P_z$  condense at higher temperatures and some new phase transition behavior will likely appear.

Beside, since we have already proposed the possibility of extending the effective atomic potential approach to larger system, it is interesting to concretize this idea, i.e. on  $PTO/STO(m/n)$  and on  $ABO_3/AO$  series superlattices which have different type of interfaces, by using the method suggested in Chapter 4 and 5. We plan to make a combination of the model potential of bulk perovskite ( such as  $BaTiO_3$ ,  $SrTiO_3$  and  $PbTiO_3$  ) and the short period system (  $PTO/STO(1/1)$ , short period  $ABO_3/AO$  member) that can be easily calculated from first-principles.

Last, but not least, as reported in Chapter 4, the series of  $ABO_3/AO$  superlattices exhibit many lattice instabilities. It will be interesting to do further investigations in order to identify the ground states and see what kind of physics will dominate there, for example, if there will be strong in-plane polarization in  $Pb$  based  $ABO_3/AO$  superlattices; what is the role of  $PbO$  layers in perovskite series superlattices?

To summarize, our investigations in the present thesis open a window to further study ferroelectricity in perovskite-based materials, not only report benchmark results on selected systems of interest but also open interesting perspectives for the study of the finite temperature properties of many other complex layered perovskite compounds. The spirit of building a model potential for effective Hamiltonian, not only for ‘small’ systems but also ‘larger’ and more complex ones, may also work for other family of compounds.

# Bibliography

- [1] Pavlo Zubko, Stefano Gariglio, Marc Gabay, Philippe Ghosez, and Jean-Marc Triscone. *Annu. Rev. Condensed Matter Phys.*, 24:141–165, 2011.
- [2] W Cochran. Crystal Stability and the theory of Ferroelectricity. *ADVANCES IN PHYSICS*, 9(36):387–423, 1960. ISSN 0001-8732.
- [3] Robert M. Pick, Morrel H. Cohen, and Richard M. Martin. Microscopic Theory of Force Constants in the Adiabatic Approximation. *Phys. Rev. B*, 1:910–920, Jan 1970.
- [4] T Wolfram and S Ellialtioglu. *Electronic and optical properties of D-Band Perovskites*. Cambridge University Press. 2006.
- [5] A. Chroneos, R. V. Vovk, I. L. Goulatis, and L. I. Goulatis. Oxygen transport in perovskite and related oxides: A brief review. *JOURNAL OF ALLOYS AND COMPOUNDS*, 494(1-2):190–195, APR 2 2010.
- [6] P. K. Davies, H. Wu, A. Y. Borisevich, I. E. Molodetsky, and L. Farber. Crystal chemistry of complex perovskites: New cation-ordered dielectric oxides. *ANNUAL REVIEW OF MATERIALS RESEARCH*, 38:369–401, 2008.
- [7] Lines M. E. and A.M. Glass. *Principles and applications of ferroelectrics and related materials*. Clarendon Press. 1977.
- [8] J H Haeni, P Irvin, W Chang, R Uecker, P Reiche, Y L Li, S Choudhury, W Tian, M E Hawley, B Craigo, A K Tagantsev, X Q Pan, S K Streiffer, L Q Chen, S W Kirchoefer, J Levy, and D G Schlom. Room-temperature ferroelectricity in strained  $SrTiO_3$ . *Nature*, 430(7001):758–61, 2004.
- [9] K. A. Müller and H. Burkard.  $SrTiO_3$ : An intrinsic quantum paraelectric below 4 K. *Phys. Rev. B*, 19:3593–3602, Apr 1979.

- [10] V. Železný, Eric Cockayne, J. Petzelt, M. F. Limonov, D. E. Usvyat, V. V. Lemanov, and A. A. Volkov. Temperature dependence of infrared-active phonons in  $CaTiO_3$ : A combined spectroscopic and first-principles study. *Phys. Rev. B*, 66:224303, Dec 2002.
- [11] Chen Ang, A. S. Bhalla, and L. E. Cross. Dielectric behavior of paraelectric  $KTaO_3$ ,  $CaTiO_3$ , and  $(Ln_{1/2}Na_{1/2})TiO_3$  under a dc electric field. *Phys. Rev. B*, 64:184104, Oct 2001.
- [12] G. A. Samara and B. Morosin. Anharmonic Effects in  $KTaO_3$ : Ferroelectric Mode, Thermal Expansion, and Compressibility. *Phys. Rev. B*, 8:1256–1264, Aug 1973.
- [13] C.H Perry and T.F. McNelly. Ferroelectric soft mode in  $KTaO_3$ . *PHYSICAL REVIEW*, 154(2):456–&, 1967. ISSN 0031-899X.
- [14] P. Hermet, M. Goffinet, J. Kreisel, and Ph. Ghosez. Raman and infrared spectra of multiferroic bismuth ferrite from first principles. *Phys. Rev. B*, 75:220102, Jun 2007.
- [15] Igor A. Kornev, S. Lisenkov, R. Haumont, B. Dkhil, and L. Bellaiche. Finite-Temperature Properties of Multiferroic  $BiFeO_3$ . *Phys. Rev. Lett.*, 99:227602, Nov 2007.
- [16] Satadeep Bhattacharjee, Eric Bousquet, and Philippe Ghosez. Engineering Multiferroism in  $CaMnO_3$ . *Phys. Rev. Lett.*, 102:117602, Mar 2009.
- [17] David J. Singh. Structure and energetics of antiferroelectric  $PbZrO_3$ . *Phys. Rev. B*, 52:12559–12563, Nov 1995.
- [18] M. D. Johannes and D. J. Singh. Crystal structure and electric field gradients of  $PbZrO_3$  from density functional calculations. *Phys. Rev. B*, 71:212101, Jun 2005.
- [19] H. Y. Hwang, Y. Iwasa, M. Kawasaki, B. Keimer, N. Nagaosa, and Y. Tokura. Emergent phenomena at oxide interfaces. *Nat Mater*, 11:103–113, 2012.
- [20] Eric Bousquet, Matthew Dawber, Nicolas Stucki, Celine Lichtensteiger, Patrick Hermet, Stefano Gariglio, Jean-Marc Triscone, and Philippe Ghosez. Improper ferroelectricity in perovskite oxide artificial superlattices. *Nature*, 452(7188):732–736, 2008.

- [21] J. Chakhalian, A. J. Millis, and J. Rondinelli. Whither the oxide interface. *NATURE MATERIALS*, 11(2):92–94, FEB 2012.
- [22] K. S. Takahashi, M. Kawasaki, and Y. Tokura. Interface ferromagnetism in oxide superlattices of  $CaMnO_3/CaRuO_3$ . *Applied Physics Letters*, 79(9):1324–1326, 2001.
- [23] John B. Goodenough. Theory of the Role of Covalence in the Perovskite-Type Manganites  $La, M(II)MnO_3$ . *Phys. Rev.*, 100:564–573, Oct 1955.
- [24] John B. Goodenough. *Journal of Physics and Chemistry of Solids*, 6(2–3): 287–297, 1958.
- [25] A. Ohtomo, D. A. Muller, J. L. Grazul, and H. Y. Hwang. Artificial charge-modulation in atomic-scale perovskite titanate superlattices. *Nature*, 419:378–380, 2002.
- [26] S. Thiel, G. Hammerl, A. Schmehl, C. W. Schneider, and J. Mannhart. Tunable Quasi-Two-Dimensional Electron Gases in Oxide Heterostructures. *Science*, 313(5795):1942–1945, 2006.
- [27] J. Mannhart and D. G. Schlom. Oxide Interfaces—An Opportunity for Electronics. *Science*, 327(5973):1607–1611, 2010.
- [28] A. D. Caviglia, S. Gariglio, N. Reyren, D. Jaccard, T. Schneider, M. Gabay, S. Thiel, G. Hammerl, J. Mannhart, and J.-M. Triscone. Electric field control of the  $LaAlO_3/SrTiO_3$  interface ground state. *Nature*, 456:624–627, 2008.
- [29] C. Cen, S. Thiel, G. Hammerl, C. W. Schneider, K. E. Andersen, C. S. Hellberg, J. Mannhart, and J. Levy. Nanoscale control of an interfacial metal-insulator transition at room temperature. *Nat Mater*, 7:298–302, 2008.
- [30] Craig J. Fennie and Karin M. Rabe. Magnetic and Electric Phase Control in Epitaxial  $EuTiO_3$  from First Principles. *Phys. Rev. Lett.*, 97:267602, Dec 2006.
- [31] N. A. Pertsev, A. G. Zembilgotov, and A. K. Tagantsev. Effect of Mechanical Boundary Conditions on Phase Diagrams of Epitaxial Ferroelectric Thin Films. *Phys. Rev. Lett.*, 80:1988–1991, Mar 1998.
- [32] Darrell G. Schlom, Long-Qing Chen, Chang-Beom Eom, Karin M Rabe, Stephen K Streiffer, and Jean-Marc Triscone. Strain Tuning of Ferroelectric Thin Films. *Annual Review of Materials Research*, 37(1):589–626, 2007.

- [33] Posadas A-B, M Lippmaa, Walker FJ, M Dawber, Ahn CH, and Jean-Marc Triscone. *In physics of ferroelectrics, A Modern perspective*, pages 219–304.
- [34] J. Junquera and Ph. Ghosez. *J. Comput. Theor. Nanoscience*, 5:2071–88.
- [35] S. N. Ruddlesden and P. Popper. The compound  $Sr_3Ti_2O_7$  and its structure. *Acta Crystallographica*, 11(1):54–55, Jan 1958.
- [36] Craig J. Fennie and Karin M. Rabe. First-principles investigation of ferroelectricity in epitaxially strained  $Pb_2TiO_4$ . *Phys. Rev. B*, 71:100102, Mar 2005.
- [37] Turan Birol, Nicole A. Benedek, and Craig J. Fennie. Interface Control of Emergent Ferroic Order in Ruddlesden-Popper  $Sr_{n+1}Ti_nO_{3n+1}$ . *Phys. Rev. Lett.*, 107:257602, Dec 2011.
- [38] Andrew Peter Mackenzie and Yoshiteru Maeno. The superconductivity of  $Sr_2RuO_4$  and the physics of spin-triplet pairing. *Rev. Mod. Phys.*, 75:657–712, May 2003.
- [39] R. S. Perry, L. M. Galvin, S. A. Grigera, L. Capogna, A. J. Schofield, A. P. Mackenzie, M. Chiao, S. R. Julian, S. I. Ikeda, S. Nakatsuji, Y. Maeno, and C. Pfleiderer. Metamagnetism and Critical Fluctuations in High Quality Single Crystals of the Bilayer Ruthenate  $Sr_3Ru_2O_7$ . *Phys. Rev. Lett.*, 86:2661–2664, Mar 2001.
- [40] S. A. Grigera, R. S. Perry, A. J. Schofield, M. Chiao, S. R. Julian, G. G. Lonzarich, S. I. Ikeda, Y. Maeno, A. J. Millis, and A. P. Mackenzie. Magnetic Field-Tuned Quantum Criticality in the Metallic Ruthenate  $Sr_3Ru_2O_7$ . *Science*, 294(5541):329–332, 2001.
- [41] S. A. Grigera, P. Gegenwart, R. A. Borzi, F. Weickert, A. J. Schofield, R. S. Perry, T. Tayama, T. Sakakibara, Y. Maeno, A. G. Green, and A. P. Mackenzie. Disorder-Sensitive Phase Formation Linked to Metamagnetic Quantum Criticality. *Science*, 306(5699):1154–1157, 2004.
- [42] G. Cao, S. K. McCall, J. E. Crow, and R. P. Guertin. Ferromagnetism in  $Sr_4Ru_3O_{10}$  : Relationship to other layered metallic oxides. *Phys. Rev. B*, 56:R5740–R5743, Sep 1997.
- [43] G. Cao, L. Balicas, W. H. Song, Y. P. Sun, Y. Xin, V. A. Bondarenko, J. W. Brill, S. Parkin, and X. N. Lin. Competing ground states in triple-layered

- $Sr_4Ru_3O_{10}$  : Verging on itinerant ferromagnetism with critical fluctuations. *Phys. Rev. B*, 68:174409, Nov 2003.
- [44] D. Fobes, M. H. Yu, M. Zhou, J. Hooper, C. J. O'Connor, M. Rosario, and Z. Q. Mao. Phase diagram of the electronic states of trilayered ruthenate  $Sr_4Ru_3O_{10}$ . *Phys. Rev. B*, 75:094429, Mar 2007.
- [45] G. Cao, S. McCall, M. Shepard, J. E. Crow, and R. P. Guertin. Magnetic and transport properties of single-crystal  $Ca_2RuO_4$  : Relationship to superconducting  $Sr_2RuO_4$ . *Phys. Rev. B*, 56:R2916–R2919, Aug 1997.
- [46] M. Braden, G. André, S. Nakatsuji, and Y. Maeno. Crystal and magnetic structure of  $Ca_2RuO_4$  : Magnetoelastic coupling and the metal-insulator transition. *Phys. Rev. B*, 58:847–861, Jul 1998.
- [47] A. V. Puchkov, M. C. Schabel, D. N. Basov, T. Startseva, G. Cao, T. Timusk, and Z.-X. Shen. Layered Ruthenium Oxides: From Band Metal to Mott Insulator. *Phys. Rev. Lett.*, 81:2747–2750, Sep 1998.
- [48] I. I. Mazin and D. J. Singh. Competitions in Layered Ruthenates: Ferromagnetism versus Antiferromagnetism and Triplet versus Singlet Pairing. *Phys. Rev. Lett.*, 82:4324–4327, May 1999.
- [49] Wei Bao, Z. Q. Mao, Z. Qu, and J. W. Lynn. Spin Valve Effect and Magnetoresistivity in Single Crystalline  $Ca_3Ru_2O_7$ . *Phys. Rev. Lett.*, 100:247203, Jun 2008.
- [50] J. H. Haeni, C. D. Theis, D. G. Schlom, W. Tian, X. Q. Pan, H. Chang, I. Takeuchi, and X.-D. Xiang. Epitaxial growth of the first five members of the  $Sr_{n+1}Ti_nO_{3n+1}$  Ruddlesden–Popper homologous series. *Applied Physics Letters*, 78(21):3292–3294, 2001.
- [51] Nicole A. Benedek and Craig J. Fennie. Hybrid Improper Ferroelectricity: A Mechanism for Controllable Polarization-Magnetization Coupling. *Phys. Rev. Lett.*, 106:107204, Mar 2011.
- [52] R. A. McKee, F. J. Walker, and M. F. Chisholm. Crystalline Oxides on Silicon: The First Five Monolayers. *Phys. Rev. Lett.*, 81:3014–3017, Oct 1998.
- [53] Javier Junquera, Magali Zimmer, Pablo Ordejón, and Philippe Ghosez. First-principles calculation of the band offset at  $BaO/BaTiO_3$  and  $SrO/SrTiO_3$  interfaces. *Phys. Rev. B*, 67:155327, Apr 2003.

- [54] Eric Bousquet, Javier Junquera, and Philippe Ghosez. First-principles study of competing ferroelectric and antiferroelectric instabilities in  $BaTiO_3/BaO$  superlattices. *Phys. Rev. B*, 82:045426, Jul 2010.
- [55] Tong Zhao, Zheng-Hao Chen, Fan Chen, Wen-Sheng Shi, Hui-Bin Lu, and Guo-Zhen Yang. Enhancement of second-harmonic generation in  $BaTiO_3/SrTiO_3$  superlattices. *Phys. Rev. B*, 60:1697–1700, Jul 1999.
- [56] S Ríos, A Ruediger, A Q Jiang, J F Scott, H Lu, and Z Chen. Orthorhombic strontium titanate in  $BaTiO_3 - SrTiO_3$  superlattices. *Journal of Physics: Condensed Matter*, 15(21):L305, 2003.
- [57] K. Iijima, T. Terashima, Y. Bando, K. Kamigaki, and H. Terauchi. Atomic layer growth of oxide thin films with perovskite-type structure by reactive evaporation. *Journal of Applied Physics*, 72(7):2840–2845, 1992.
- [58] Hitoshi Tabata, Hidekazu Tanaka, and Tomoji Kawai. Formation of artificial  $BaTiO_3/SrTiO_3$  superlattices using pulsed laser deposition and their dielectric properties. *Applied Physics Letters*, 65(15):1970–1972, 1994.
- [59] Hitoshi Tabata and Tomoji Kawai. Dielectric properties of strained  $(Sr, Ca)TiO_3/(Ba, Sr)TiO_3$  artificial lattices. *Applied Physics Letters*, 70(3):321–323, 1997.
- [60] Takaaki Tsurumi, Tomoyoshi Ichikawa, Terukiyo Harigai, Hirofumi Kakemoto, and Satoshi Wada. Dielectric and optical properties of  $BaTiO_3/SrTiO_3$  and  $BaTiO_3/BaZrO_3$  superlattices. *Journal of Applied Physics*, 91(4):2284–2289, 2002.
- [61] Toru Shimuta, Osamu Nakagawara, Takahiro Makino, Seiichi Arai, Hitoshi Tabata, and Tomoji Kawai. Enhancement of remanent polarization in epitaxial  $BaTiO_3/SrTiO_3$  superlattices with “asymmetric” structure. *Journal of Applied Physics*, 91(4):2290–2294, 2002.
- [62] J. B. Neaton and K. M. Rabe. Theory of polarization enhancement in epitaxial  $BaTiO_3/SrTiO_3$  superlattices. *Applied Physics Letters*, 82(10):1586–1588, 2003.
- [63] Oswaldo Diéguez, Karin M. Rabe, and David Vanderbilt. First-principles study of epitaxial strain in perovskites. *Phys. Rev. B*, 72:144101, Oct 2005.

- [64] Sergey Lisenkov and L. Bellaiche. Phase diagrams of  $BaTiO_3/SrTiO_3$  superlattices from first principles. *Phys. Rev. B*, 76:020102, Jul 2007.
- [65] A. Q. Jiang, J. F. Scott, Huibin Lu, and Zhenghao Chen. Phase transitions and polarizations in epitaxial  $BaTiO_3/SrTiO_3$  superlattices studied by second-harmonic generation. *Journal of Applied Physics*, 93(2):1180–1185, 2003.
- [66] Karen Johnston, Xiangyang Huang, J. B. Neaton, and Karin M. Rabe. First-principles study of symmetry lowering and polarization in  $BaTiO_3/SrTiO_3$  superlattices with in-plane expansion. *Phys. Rev. B*, 71:100103, Mar 2005.
- [67] Y. L. Li, S. Y. Hu, D. Tenne, A. Soukiassian, D. G. Schlom, L. Q. Chen, X. X. Xi, K. J. Choi, C. B. Eom, A. Saxena, T. Lookman, and Q. X. Jia. Interfacial coherency and ferroelectricity of  $BaTiO_3/SrTiO_3$  superlattice films. *Applied Physics Letters*, 91(25):252904, 2007.
- [68] M. Sepliarsky, S. R. Phillpot, D. Wolf, M. G. Stachiotti, and R. L. Migoni. Long-ranged ferroelectric interactions in perovskite superlattices. *Phys. Rev. B*, 64:060101, Jul 2001.
- [69] M. Sepliarsky, S. R. Phillpot, D. Wolf, M. G. Stachiotti, and R. L. Migoni. Ferroelectric properties of  $KNbO_3/KTaO_3$  superlattices by atomic-level simulation. *Journal of Applied Physics*, 90(9):4509–4519, 2001.
- [70] M. Sepliarsky, S. R. Phillpot, M. G. Stachiotti, and R. L. Migoni. Ferroelectric phase transitions and dynamical behavior in  $KNbO_3/KTaO_3$  superlattices by molecular-dynamics simulation. *Journal of Applied Physics*, 91(5):3165–3171, 2002.
- [71] E. D. Specht, H.-M. Christen, D. P. Norton, and L. A. Boatner. X-Ray Diffraction Measurement of the Effect of Layer Thickness on the Ferroelectric Transition in Epitaxial  $KTaO_3/KNbO_3$  Multilayers. *Phys. Rev. Lett.*, 80:4317–4320, May 1998.
- [72] J. C. Jiang, X. Q. Pan, W. Tian, C. D. Theis, and D. G. Schlom. Abrupt  $PbTiO_3/SrTiO_3$  superlattices grown by reactive molecular beam epitaxy. *Applied Physics Letters*, 74(19):2851–2853, 1999.
- [73] M. Dawber, C. Lichtensteiger, M. Cantoni, M. Veithen, P. Ghosez, K. Johnston, K. M. Rabe, and J.-M. Triscone. Unusual Behavior of the Ferroelectric

- Polarization in  $PbTiO_3/SrTiO_3$  Superlattices. *Phys. Rev. Lett.*, 95:177601, Oct 2005.
- [74] W. Zhong and David Vanderbilt. Competing Structural Instabilities in Cubic Perovskites. *Phys. Rev. Lett.*, 74:2587–2590, Mar 1995.
- [75] W. Zhong and David Vanderbilt. Effect of quantum fluctuations on structural phase transitions in  $SrTiO_3$  and  $BaTiO_3$ . *Phys. Rev. B*, 53:5047–5050, Mar 1996.
- [76] P. Zubko, N. Jecklin, A. Torres-Pardo, P. Aguado-Puente, A. Gloter, C. Lichtensteiger, J. Junquera, O. Stphan, and J.-M. Triscone. Electrostatic coupling and local structural distortions at interfaces in ferroelectric/paraelectric superlattices. *Nano Letters*, 12(6):2846–2851, 2012. doi: 10.1021/nl3003717.
- [77] Massimiliano Stengel, Craig J. Fennie, and Philippe Ghosez. Electrical properties of improper ferroelectrics from first principles. *Phys. Rev. B*, 86:094112, Sep 2012.
- [78] James M. Rondinelli and Craig J. Fennie. Octahedral Rotation-Induced Ferroelectricity in Cation Ordered Perovskites. *Advanced Materials*, 24(15):1961–1968, 2012. doi: 10.1002/adma.201104674.
- [79] Andrew T. Mulder, Nicole A. Benedek, James M. Rondinelli, and Craig J. Fennie. Turning  $ABO_3$  antiferroelectrics into ferroelectrics: Design rules for practical rotation-driven ferroelectricity in double perovskites and  $A_3B_2O_7$  ruddlesden-popper compounds. *Advanced Functional Materials*, pages n/a–n/a, 2013.
- [80] J. Valasek. Piezo-Electric and Allied Phenomena in Rochelle Salt. *Phys. Rev.*, 17:475–481, Apr 1921.
- [81] A. P. Levanyuk and Daniil G. Sannikov. Improper ferroelectrics. *Sov. Phys. Usp.*, 17:199, 1974.
- [82] Sang-Wook Cheong and Maxim Mostovoy. Multiferroics: a magnetic twist for ferroelectricity. *Nat Mater*, 6(1):13, 2007.
- [83] Andrei Malashevich and David Vanderbilt. First principles study of improper ferroelectricity in  $TbMnO_3$ . *Phys. Rev. Lett.*, 101:037210, Jul 2008.

- [84] Kunihiko Yamauchi and Silvia Picozzi. Magnetically induced ferroelectricity in  $TbMnO_3$  : inverse goodenoughkanamori interaction. *Journal of Physics: Condensed Matter*, 21(6):064203, 2009.
- [85] Craig J. Fennie and Karin M. Rabe. Ferroelectric transition in  $YMnO_3$  from first principles. *Phys. Rev. B*, 72:100103, Sep 2005.
- [86] Pierre Toledano. Pseudo-proper ferroelectricity and magnetoelectric effects in  $TbMnO_3$ . *Phys. Rev. B*, 79:094416, Mar 2009.
- [87] A. Cano and A. P. Levanyuk. Pseudoproper ferroelectricity in thin films. *Phys. Rev. B*, 81:172105, May 2010.
- [88] Zeila Zanolli, Jacek C. Wojdeł, Jorge Íñiguez, and Philippe Ghosez. Electric control of the magnetization in  $BiFeO_3/LaFeO_3$  superlattices. *Phys. Rev. B*, 88:060102, Aug 2013.
- [89] Karin M. Rabe. First-Principles Calculations of Complex Metal-Oxide Materials. *Annual Review of Condensed Matter Physics*, 1(1):211–235, 2010.
- [90] Ph. Ghosez, E. Cockayne, U. V. Waghmare, and K. M. Rabe. Lattice dynamics of  $BaTiO_3$ ,  $PbTiO_3$ , and  $PbZrO_3$ : A comparative first-principles study. *Phys. Rev. B*, 60:836–843, Jul 1999.
- [91] Rici Yu and Henry Krakauer. First-Principles Determination of Chain-Structure Instability in  $KNbO_3$ . *Phys. Rev. Lett.*, 74:4067–4070, May 1995.
- [92] X. Gonze, J.-M. Beuken, R. Caracas, F. Detraux, M. Fuchs, G.-M. Rignanese, L. Sindic, M. Verstraete, G. Zerah, F. Jollet, M. Torrent, A. Roy, M. Mikami, Ph. Ghosez, J.-Y. Raty, and D.C. Allan. First-principles computation of material properties: the {ABINIT} software project. *Computational Materials Science*, 25(3):478–492, 2002. ISSN 0927-0256.
- [93] G. Kresse and J. Furthmüller. Efficiency of ab-initio total energy calculations for metals and semiconductors using a plane-wave basis set. *Computational Materials Science*, 6(1):15–50, 1996. ISSN 0927-0256.
- [94] G. Kresse and J. Furthmüller. Efficient iterative schemes for *ab initio* total-energy calculations using a plane-wave basis set. *Phys. Rev. B*, 54:11169–11186, Oct 1996.

- [95] G. Kresse and J. Hafner. *Ab initio* molecular dynamics for liquid metals. *Phys. Rev. B*, 47:558–561, Jan 1993.
- [96] G. Kresse and J. Hafner. *Ab initio* molecular-dynamics simulation of the liquid-metal–amorphous-semiconductor transition in germanium. *Phys. Rev. B*, 49:14251–14269, May 1994.
- [97] José M Soler, Emilio Artacho, Julian D Gale, Alberto García, Javier Junquera, Pablo Ordejón, and Daniel Sánchez-Portal. The SIESTA method for ab initio order- $N$  materials simulation. *Journal of Physics: Condensed Matter*, 14(11):2745, 2002. URL <http://stacks.iop.org/0953-8984/14/i=11/a=302>.
- [98] <http://www.crystal.unito.it/>.
- [99] Karlheinz Schwarz and Peter Blaha. ISSN 0927-0256.
- [100] Paolo Giannozzi, Stefano Baroni, Nicola Bonini, Matteo Calandra, Roberto Car, Carlo Cavazzoni, Davide Ceresoli, Guido L Chiarotti, Matteo Cococcioni, Ismaila Dabo, Andrea Dal Corso, Stefano de Gironcoli, Stefano Fabris, Guido Fratesi, Ralph Gebauer, Uwe Gerstmann, Christos Gougoussis, Anton Kokalj, Michele Lazzeri, Layla Martin-Samos, Nicola Marzari, Francesco Mauri, Riccardo Mazzarello, Stefano Paolini, Alfredo Pasquarello, Lorenzo Paulatto, Carlo Sbraccia, Sandro Scandolo, Gabriele Sclauzero, Ari P Seitsonen, Alexander Smogunov, Paolo Umari, and Renata M Wentzcovitch. QUANTUM ESPRESSO: a modular and open-source software project for quantum simulations of materials. *Journal of Physics: Condensed Matter*, 21(39):395502, 2009. URL <http://stacks.iop.org/0953-8984/21/i=39/a=395502>.
- [101] K. M. Rabe and J. D. Joannopoulos. *Ab initio* determination of a structural phase transition temperature. *Phys. Rev. Lett.*, 59:570–573, Aug 1987.
- [102] K. M. Rabe and J. D. Joannopoulos. Theory of the structural phase transition of *GeTe*. *Phys. Rev. B*, 36:6631–6639, Oct 1987.
- [103] W. Zhong, David Vanderbilt, and K. M. Rabe. Phase Transitions in *BaTiO<sub>3</sub>* from First Principles. *Phys. Rev. Lett.*, 73:1861–1864, Sep 1994.
- [104] W. Zhong, David Vanderbilt, and K. M. Rabe. First-principles theory of ferroelectric phase transitions for perovskites: The case of *BaTiO<sub>3</sub>*. *Phys. Rev. B*, 52:6301–6312, Sep 1995.

- [105] Jacek C Wojdeł, Patrick Hermet, Mathias P Ljungberg, Philippe Ghosez, and Jorge Íñiguez. First-principles model potentials for lattice-dynamical studies: general methodology and example of application to ferroic perovskite oxides. *Journal of Physics: Condensed Matter*, 25(30):305401, 2013.
- [106] L. D. Landau and E. M. Lifshitz. *Statistical Physics*. 1968.
- [107] C. Kittel. *Physique de l'état solide(7th)*. 1998.
- [108] J. C. Wojdeł, P. Hermet, M. P. Ljungberg, P. Ghosez, and J. Íñiguez. First-principles model potentials for lattice-dynamical studies: general methodology and example of application to ferroic perovskite oxides. *ArXiv e-prints*, January 2013.
- [109] P. Hohenberg and W. Kohn. Inhomogeneous Electron Gas. *Phys. Rev.*, 136: B864–B871, Nov 1964.
- [110] W. Kohn and L. J. Sham. Self-Consistent Equations Including Exchange and Correlation Effects. *Phys. Rev.*, 140:A1133–A1138, Nov 1965.
- [111] Stefano Baroni, Paolo Giannozzi, and Andrea Testa. Green's-function approach to linear response in solids. *Phys. Rev. Lett.*, 58:1861–1864, May 1987.
- [112] Stefano Baroni, Paolo Giannozzi, and Andrea Testa. Elastic Constants of Crystals from Linear-Response Theory. *Phys. Rev. Lett.*, 59:2662–2665, Dec 1987.
- [113] Stefano de Gironcoli, Stefano Baroni, and Raffaele Resta. Piezoelectric properties of III-V semiconductors from first-principles linear-response theory. *Phys. Rev. Lett.*, 62:2853–2856, Jun 1989.
- [114] Stefano de Gironcoli, Paolo Giannozzi, and Stefano Baroni. Structure and thermodynamics of  $Si_xGe_{1-x}$  alloys from *ab initio* Monte Carlo simulations. *Phys. Rev. Lett.*, 66:2116–2119, Apr 1991.
- [115] X. Gonze and J.-P. Vigneron. Density-functional approach to nonlinear-response coefficients of solids. *Phys. Rev. B*, 39:13120–13128, Jun 1989.
- [116] Xavier Gonze. Perturbation expansion of variational principles at arbitrary order. *Phys. Rev. A*, 52:1086–1095, Aug 1995.
- [117] Xavier Gonze. Adiabatic density-functional perturbation theory. *Phys. Rev. A*, 52:1096–1114, Aug 1995.

- [118] Xavier Gonze and Changyol Lee. Dynamical matrices, Born effective charges, dielectric permittivity tensors, and interatomic force constants from density-functional perturbation theory. *Phys. Rev. B*, 55:10355–10368, Apr 1997.
- [119] M. Veithen, X. Gonze, and Ph. Ghosez. Nonlinear optical susceptibilities, Raman efficiencies, and electro-optic tensors from first-principles density functional perturbation theory. *Phys. Rev. B*, 71:125107, Mar 2005.
- [120] R. M. Martin. *Electronic structure: Basic theory and practical methods*. Cambridge Univ. Press, Cambridge, 2004.
- [121] R. O. Jones and O. Gunnarsson. The density functional formalism, its applications and prospects. *Rev. Mod. Phys.*, 61:689–746, Jul 1989.
- [122] Andrea Dal Corso, Stefano Baroni, Raffaele Resta, and Stefano de Gironcoli. *Ab initio* calculation of phonon dispersions in II-VI semiconductors. *Phys. Rev. B*, 47:3588–3592, Feb 1993.
- [123] Alexander Khein, D. J. Singh, and C. J. Umrigar. All-electron study of gradient corrections to the local-density functional in metallic systems. *Phys. Rev. B*, 51:4105–4109, Feb 1995.
- [124] John P. Perdew, Kieron Burke, and Yue Wang. Generalized gradient approximation for the exchange-correlation hole of a many-electron system. *Phys. Rev. B*, 54:16533–16539, Dec 1996.
- [125] Zhigang Wu and R. E. Cohen. More accurate generalized gradient approximation for solids. *Phys. Rev. B*, 73:235116, Jun 2006.
- [126] Andrea Dal Corso, Stefano Baroni, and Raffaele Resta. Density-functional theory of the dielectric constant: Gradient-corrected calculation for silicon. *Phys. Rev. B*, 49:5323–5328, Feb 1994.
- [127] X. Gonze, Ph. Ghosez, and R. W. Godby. Density-Polarization Functional Theory of the Response of a Periodic Insulating Solid to an Electric Field. *Phys. Rev. Lett.*, 74:4035–4038, May 1995.
- [128] Ph. Ghosez, X. Gonze, and R. W. Godby. Long-wavelength behavior of the exchange-correlation kernel in the Kohn-Sham theory of periodic systems. *Phys. Rev. B*, 56:12811–12817, Nov 1997.

- [129] O. Gunnarsson, M. Jonson, and B. I. Lundqvist. Descriptions of exchange and correlation effects in inhomogeneous electron systems. *Phys. Rev. B*, 20:3136–3164, Oct 1979.
- [130] Hendrik J. Monkhorst and James D. Pack. Special points for Brillouin-zone integrations. *Phys. Rev. B*, 13:5188–5192, Jun 1976.
- [131] D. R. Hamann, M. Schlüter, and C. Chiang. Norm-Conserving Pseudopotentials. *Phys. Rev. Lett.*, 43:1494–1497, Nov 1979.
- [132] Warren E. Pickett. Pseudopotential methods in condensed matter applications. *Computer Physics Reports*, 9(3):115–197, 1989. ISSN 0167-7977.
- [133] Michael Teter. Additional condition for transferability in pseudopotentials. *Phys. Rev. B*, 48:5031–5041, Aug 1993.
- [134] M. Dawber, K. M. Rabe, and J. F. Scott. Physics of thin-film ferroelectric oxides. *Rev. Mod. Phys.*, 77:1083–1130, Oct 2005.
- [135] Ph. Ghosez and J. Junquera. *Handbook of Theoretical and Computational Nanotechnology*, volume 9. (American Scientific Publishers, Stevenson Ranch, CA), 2006.
- [136] Pavlo Zubko, Stefano Gariglio, Marc Gabay, Philippe Ghosez, and Jean-Marc Triscone. Interface Physics in Complex Oxide Heterostructures. *Annual Review of Condensed Matter Physics*, 2(1):141–165, 2011.
- [137] Matthew Dawber, Nicolas Stucki, Celine Lichtensteiger, Stefano Gariglio, Philippe Ghosez, and Jean\*-Marc Triscone. Tailoring the properties of artificially layered ferroelectric superlattices. *Advanced Materials*, 49(23):4153–4159, 2007.
- [138] Philippe Ghosez and Jean-Marc Triscone. Coupling of three lattice instabilities. *Nat Mater*, 2011.
- [139] James M. Rondinelli and Craig J. Fennie. Ferroelectricity: Octahedral Rotation-Induced Ferroelectricity in Cation Ordered Perovskites (Adv. Mater. 15/2012). *Advanced Materials*, 24(15):1961, 2012.
- [140] K. H. Hellwege and O. Madelung, editors. *Landolt-Börnstein: Numerical Data and Functional Relationships in Science and Technology*, volume III/16. (Springer-Verlag), 1981.

- [141] Pablo Aguado-Puente, Pablo Garcia-Fernandez, and Javier Junquera. Interplay of Couplings between Antiferrodistortive, Ferroelectric, and Strain Degrees of Freedom in Monodomain  $PbTiO_3/SrTiO_3$  Superlattices. *Phys. Rev. Lett.*, 107: 217601, Nov 2011.
- [142] Craig J. Fennie and Karin M. Rabe. Structural and dielectric properties of  $Sr_2TiO_4$  from first principles. *Phys. Rev. B*, 68:184111, Nov 2003.
- [143] J. Padilla and David Vanderbilt. Ab initio study of  $BaTiO_3$  surfaces. *Phys. Rev. B*, 56:1625–1631, Jul 1997.
- [144] Philippe GHOSEZ. *First-principles study of the dielectric and dynamical properties of barium titanate*. PhD thesis, UCL, 1997.
- [145] Gregory Geneste, Eric Bousquet, Javier Junquera, and Philippe Ghosez. Finite-size effects in  $BaTiO_3$  nanowires. *Applied Physics Letters*, 88(11):112906, 2006.
- [146] Gregory Geneste, Eric Bousquet, and Philippe Ghosez. New Insight into the Concept of Ferroelectric Correlation Volume. *Journal of Computational and Theoretical Nanoscience*, 5(4):517–520, 2008.
- [147] Born M. and M. Goppert-Mayer. *Handbuch Physik*, 24(623), 1933.
- [148] Ph. Ghosez, J.-P. Michenaud, and X. Gonze. Dynamical atomic charges: The case of  $ABO_3$  compounds. *Phys. Rev. B*, 58:6224–6240, Sep 1998.
- [149] Alice Ruini, Raffaele Resta, and Stefano Baroni. Dynamical-charge neutrality at a crystal surface. *Phys. Rev. B*, 57:5742–5745, Mar 1998.
- [150] A. Ruini, R. Resta, and S. Baroni. Effects of interface morphology on Schottky-barrier heights: A case study on  $Al/GaAs(001)$ . *Phys. Rev. B*, 56:14921–14924, Dec 1997.
- [151] W. Zhong, R. D. King-Smith, and David Vanderbilt. Giant LO-TO splittings in perovskite ferroelectrics. *Phys. Rev. Lett.*, 72:3618–3621, May 1994.
- [152] P. Zubko, N. Stucki, C. Lichtensteiger, and J.-M. Triscone. X-Ray Diffraction Studies of  $180^\circ$  Ferroelectric Domains in  $PbTiO_3/SrTiO_3$  Superlattices under an Applied Electric Field. *Phys. Rev. Lett.*, 104:187601, May 2010.
- [153] Almudena Torres-Pardo, Alexandre Gloter, Pavlo Zubko, Noémie Jecklin, Céline Lichtensteiger, Christian Colliex, Jean-Marc Triscone, and Odile

- Stéphan. Spectroscopic mapping of local structural distortions in ferroelectric  $PbTiO_3/SrTiO_3$  superlattices at the unit-cell scale. *Phys. Rev. B*, 84:220102, Dec 2011.
- [154] Pablo Aguado-Puente and Javier Junquera. Structural and energetic properties of domains in  $PbTiO_3/SrTiO_3$  superlattices from first principles. *Phys. Rev. B*, 85:184105, May 2012.
- [155] P. Zubko, N. Jecklin, A. Torres-Pardo, P. Aguado-Puente, A. Gloter, C. Lichtensteiger, J. Junquera, O. Stéphan, and J.-M. Triscone. Electrostatic Coupling and Local Structural Distortions at Interfaces in Ferroelectric/Paraelectric Superlattices. *Nano Letters*, 12(6):2846–2851, 2012.